Phase Retrieval Methods for Polychromatic Propagation-Based Phase-Contrast X-ray Imaging

by

Rhiannon Lee Lohr

A thesis
presented to the University of Waterloo
in fulfillment of the
thesis requirement for the degree of
Master of Applied Science
in
Electrical and Computer Engineering

Waterloo, Ontario, Canada, 2019

I hereby declare that I am the sole author of this thesis. This is a true copy of the thesis, including any required final revisions, as accepted by my examiners.

I understand that my thesis may be made electronically available to the public.

Abstract

X-ray imaging, based on conventional attenuation methods, is employed in various industrial, medical and scientific imaging application. Phase-contrast X-ray imaging is an emerging modality that has shown promise to image and characterize weakly absorbing objects, such as three-dimensional printed plastics and breast tissue. Propagation-based phase-contrast X-ray imaging is the simplest of the existing phase-contrast methods as it does not require any additional optics and can easily be integrated into current X-ray systems that utilize polychromatic X-ray sources. This novel imaging technique requires post-image processing using an algorithm called phase retrieval to extract phase information from the measured intensity.

Although propagation-based phase-contrast X-ray imaging offers the simplest setup, it possesses the most mathematically intensive methods to retrieve the phase. Phase retrieval is a nonlinear inverse technique used to estimate the phase shift, thickness or electron density throughout an image. Many of these phase retrieval methods have been developed assuming a monochromatic source, although can be extended to a polychromatic source.

This work compares seven phase retrieval methods under various conditions in the presence of a polychromatic source in simulation of different objects and materials. Six of these phase retrieval methods are single-shot algorithms that require only one phase-contrast image; whereas one method is iterative and requires an absorption and phase-contrast image. Each method is derived under different assumptions, but all should produce the same result of retrieved phase shift, thickness or electron density. Overall, Paganin's method performed the best under all test cases and was further applied to experimental data. Polytetrafluoroethylene, varying in thickness and shape, was imaged using a polychromatic source under numerous conditions and Paganin's method was applied to determine its limitations. In general, Paganin's method resulted in a high relative error in experiment, which is not what was seen in simulation. From these results and analysis, sources of error were determined to arise from the detector, the object and/or the X-ray source spectrum.

Isolating the source of error is difficult to accomplish in experiment because it is hard to eliminate certain variables completely. For this reason, further analysis on the sources of error were accomplished in simulation. The effect of material parameters was investigated using different X-ray source spectrums, source-to-object distances and object-to-detector distances. This research suggests that Paganin's method is highly material dependent and what is considered sufficiently thin for one material may not apply to another material. Generally, a filtered spectrum using 2 mm of aluminum gives the lowest relative error for all materials. Also, the trend between the retrieved thickness and the measured thickness of the object is observed to be polynomial when the object thickness exceeds 100 μm.

Further analysis shows that the polychromatic spectrum needs to be well calibrated to give accurate phase or thickness results and using different X-ray sources can affect the error produced by Paganin's method. Paganin's method uses Fourier filtering that allows it to increase the signal-to-noise ratio in an image and, thus, makes the algorithm resilient to noise.

This research suggests that although Paganin's method is one of the best phase retrieval methods derived to date, it has its limitations that include imaging thick materials; therefore it may not be the best-suited for industrial imaging where thick plastic objects are imaged for defects. Another limitation of this method is that it is unable to retrieve the thickness of high-density, high-atomic number materials. Finally, it appears that the spectrum utilized in imaging needs to be well characterized and calibrated for Paganin's method to work.

Acknowledgements

I would like to thank my supervisor, Dr. Karim Karim for his support and advising throughout my degree. I would like to thank Dr. Chris Scott and Abdollah Pil-Ali for mentoring me through my Master's degree and looking over my final code. I would like to thank Yunzhe Li and Dr. Celal Con for providing me with detectors for X-ray imaging. I would like to thank family and friends for their endless support throughout my graduate studies. Also, I would like to thank my former dog, Cassie, my present dog, Sofie, and my guinea pig, Maple for getting me through all of university with their endless hugs. Further, I would like to thank rock climbing and everyone within the community for their endless support.

Collaboration with KA Imaging Inc. assisted in making this work a success. Lastly, I would like to thank NSERC and the government of Ontario for providing me funding throughout my degree. This work would not have been possible without their contributions.

Dedication

This is dedicated to my parents, Ron and Michelle, and my brother, Cameron.

Table of Contents

List of Tables

List of Figures

Abbreviations

2D two-dimensional 11, 49

3D three-dimensional 1, 11, 67

a-Se amorphous selenium 19, 47, 67, 92, 100

APBA attenuation-partition based algorithm xiv, 35, 39, 52, 54–58, 60, 62, 63, 66, 99

APS Active Pixel Sensors 19

$CaWO_4$ calcium tungstate 21

CCD charged-coupled device 19, 21

CdTe cadmium telluride 46

CdZnTe cadmium zinc telluride 20

CMOS complementary metal-oxide-semiconductor 19, 42, 44, 67, 92, 100

CsI cesium iodide 21

CT computed tomography 3, 11, 28, 30

CTF contrast transfer function 23, 25, 26, 32, 33, 39, 52, 57–60, 62, 63, 99

FFT fast Fourier transform 24, 33

Ga_2O_2S gadolinium oxysulfide 21

HgI_2 mercury iodide 20

LHS left-hand side 24, 26, 30

MTF modulation transfer function 42, 49

NIST National Institute of Standards and Technology 13, 41, 46

NPS noise power spectrum 43

ODD object-to-detector distance 9, 10, 26, 35, 41, 54, 63, 68, 71–73, 75, 80

PAD Phase attenuation duality 33, 35, 36, 39, 52, 56–60, 62, 63, 66

PCI phase-contrast X-ray imaging 1–3, 6, 9–11, 22, 23, 30, 44, 67, 80, 87, 90, 98, 99

PPA passive pixel arrays 19

PSF point spread function 42, 100

PTFE polytetrafluoroethylene 3, 46, 51, 52, 61–63, 65, 67, 70–72, 74, 80, 82–84, 86, 92, 99, 100

RHS right-hand side 24, 30

Se selenium 20

SNR signal-to-noise ratio 71, 72, 95, 97

SOD source-to-object distance 9, 10, 54, 68, 71–74, 80

STAR Silicon Thin-filmed Applied Research 20, 67

TFT thin-film transistor 21

TIE transport of intensity equation 23–27, 29–31, 34, 36, 38, 39, 52, 54, 55, 57, 58, 60, 62, 63, 65, 99

Chapter 1

Introduction

In 1895, Röntgen produced and detected X-rays for the first time. This has been the sole method of radiographic commercial imaging up to this date. The first X-ray examining room was built in Glasgow in 1896, although the technology did not really become standard practice until after World War I [1]. This method of imaging relies on variation of materials' absorption coefficient, which offers poor contrast when imaging light-element materials. Regardless of these drawbacks, X-ray radiography is used successfully in many applications such as: X-ray imaging for medical diagnoses, mammography for tumour or cancer detection, non-destructive failure detection of cracks and porosities in materials, and for screening baggage at the airport.

Every object has a complex refractive index, where the imaginary part describes the absorption of X-rays and is retrieved in conventional X-ray imaging. Over the years it was found that the object's electron density causes phase variations that are also present in the X-ray wavefront that exits the object and can be visualized using phase-contrast techniques [2, 3]. Using this method of imaging, objects that offer low contrast in conventional imaging, such as light-element or low density materials and soft tissue, can be imaged with a higher sensitivity using phase-contrast X-ray imaging (PCI) [4]. There is a high demand for improving contrast of low density materials (e.g. three-dimensional (3D) printed polymer composites or in mammography) in a fast, non-destructive manner. PCI has shown promise in detecting voids or defects in quality control analysis, along with detecting cancer with high sensitivity and specificity in mammography.

PCI can be performed using many different setups, where some require complex optical elements such as interferomtery-based [5, 6], analyzer-based, and coded-apertures [7, 8]. The simplest implementation of PCI is free-space propagation since it does not require any

optical elements [4]. In this method, the object is placed at a sufficient distance away from the detector to allow the X-ray wavefront to propagate, which gives rise to Fresnel diffraction fringes. The refractive index changes abruptly at the material boundaries, leading to edge-enhancement that is caused by the dependency of the fringes on the Laplacian of the phase. The only requirement for edge-enhancement to occur is there has to be sufficient transverse coherence length, $L_\perp = \lambda R_1/s$, where λ is the X-ray wavelength, R_1 is the source-to-object distance and s is the X-ray source focal spot size [9].

Propagation-based PCI has been commonly used with a monochromatic synchrotron source [10, 11], but due to the size and cost of the synchrotron facilities, it makes it difficult to use in any non-destructive testing or medical imaging. Currently, there are other imaging methods that can perform similar tasks for lower cost than using a synchrotron source. More recently polychromatic microfocus sources are being integrated into the propagation-based PCI systems [4, 12, 13, 14], making the system much more cost efficient and reducing the amount of space required to capture an image.

Although propagation-based PCI has the simplest setup out of all PCI methods, it possesses the most mathematically intensive post-processing [15]. The images captured on the detector of the object contains only qualitative intensity values. Due to the edge enhancement that is occurring at the boundaries of the object, it makes it difficult to understand where the boundaries of the object actually are. For this reason, a post-image processing method called phase retrieval is essential to recover quantitative information on the object. Once phase retrieval is implemented on the object, it recovers either the phase, electron density or thickness of the object depending on the equation applied to the intensity values. For propagation-based phase-contrast X-ray imaging, phase retrieval is a nonlinear inverse problem that many researchers have tried to linearize to make the math simpler, the processing time shorter ,and reduce the number of images required to create the final image, in turn reducing the dose the object receives [16, 17]. Many phase retrieval methods have been derived in the case of a monochromatic source [18, 19, 15, 20, 21], thus using a polychromatic source makes phase retrieval an even more complex problem [12, 13, 22]. Phase retrieval in the case of using a polychromatic source is essential for this PCI method to be used in mammography or non-destructive imaging of plastics. The motivation is that polychromatic sources are significantly cheaper than monochromatic sources and are currently used in many conventional X-ray imaging settings; therefore making it easier to integrate this phase-contrast method into current settings that already use X-ray imaging.

In this work, seven different phase retrieval methods are investigated and their limitations are discussed in the case of using a polychromatic source. In the past, many of these methods have been heavily applied in the case of a monochromatic source and

have not been investigated for the polychromatic case. The seven methods investigated are: Paganin's method [18], Bronnikov method [19], Modified Bronnikov method [23], Arhatari TIE method [12], Arhatari CTF method [13], phase-attenuation duality [20] and attenuation-partition based algorithm [21]. The first six of these methods mentioned only require one image; whereas attenuation-partition based algorithm is an iterative approach that requires a phase-contrast and attenuation image. Paganin's method, Bronnikov method, Modified Bronnikov method and phase-attenuation duality are phase retrieval methods that are derived for monochromatic sources and have not been applied in many polychromatic cases. Arhatari's methods have been derived for polychromatic cases, but have not been rarely used in literature. After investigating the seven methods, the best method will be chosen and applied to images containing polytetrafluoroethylene (PTFE) sample, which is a commonly used plastic in industry. Finally, an investigation on the parameters that effect phase retrieval of experimental results will be made that includes: the material's effect, the spectrum's effect and a small investigation on the effect of noise. Based on these investigations, the limitations of the phase retrieval methods when using a polychromatic source becomes apparent and will aid in understanding when the phase retrieval method can be applied and possible ways of applying corrections when imaging specific materials. It also aids in understanding how well the spectrum and other parameters need to be known in order to produce accurate results. When phase retrieval is applied properly to an image, it will aid significantly in the analysis and understanding of the X-ray image. Also, phase retrieval is a requirement in post-processing of micro computed tomography (CT) images, which could revolutionize diagnosis for certain medical applications.

1.1 Thesis Organization

The focus of this thesis is to investigate seven different phase retrieval methods in the case of polychromatic propagation-based phase-contrast X-ray imaging, then apply the best method to experimental data and discuss the effect of certain parameters on the method. The thesis chapters are organized as follows:

- Chapter 2 provides background on the X-ray imaging, expanding on some of the current existing phase-contrast X-ray imaging methods. It describes the fundamentals of X-ray interactions with matter and X-ray mechanisms. Also, X-ray sources and X-ray detectors that are used in current PCI are examined.

- Chapter 3 describes the derivation of each phase retrieval method and the assumptions made in detail. At the end of this chapter, a table outlines the all assumptions made to assist in choosing the most appropriate phase retrieval method.

- Chapter 4 outlines the numerical model, assumptions made in the model and summarizes the MATLAB numerical implementation of the simulations used throughout this thesis.

- Chapter 5 compares the seven phase retrieval methods using three different materials that vary in density. The methods are validated under five different test cases that include: varying the thickness, varying the source potential, varying the pixel size, varying the source-to-object distance, and varying the object-to-detector distance.

- Chapter 6 experimentally implements Paganin's method, which is found to be the most accurate and reliable method out of the seven investigated methods. It shows experimental results under different conditions and explains some sources of error.

- Chapter 7 describes parameters that effect the results of Paganin's method and that can cause sources of error to arise in experimental imaging.

- Chapter 8 provides the main conclusions and contributions of this work to phase retrieval. Suggestions for future work are also discussed.

Chapter 2

X-Ray Imaging

In this chapter, X-ray interactions, mechanisms of X-ray radiation, X-ray sources, X-ray detectors, absorption X-ray radiography, phase-contrast X-ray radiography and computed tomography will be described in detail.

2.1 Absorption X-ray Radiography

The most common form of X-ray imaging performed in medicine and industry is called absorption X-ray radiography and it relies on the attenuation of X-rays in materials before the X-rays reach the detector. Different densities and elemental components of materials attenuate X-rays by different amounts. In this method, the source is placed at some distance R_1 from the object and the object is placed immediately before the detector. The number of X-rays that travel through the object are determined by the object's thickness $T(\mathbf{r}_\perp)$ and the attenuation coefficient μ. The intensity of X-rays at the detector in the presence of an object can be determined using the Beer-Lambert Law:

$$I = I_{in} \exp\left[-\mu T(\mathbf{r}_\perp)\right] \tag{2.1}$$

where I_{in} is the incident intensity that is measured with no object present in the X-ray wavefront. Thus, it is difficult to resolve objects that are thin or have small attenuation constants. This method cannot easily resolve objects that have atomic number Z less than 20. Bone, which is mostly composed of calcium (Z = 20), can be resolved in an absorption X-ray image because it has a density that is two times that of tissue. Soft materials, such as soft tissue, leads to poor contrast in absorption images.

2.2 Phase-Contrast X-ray Radiology

Optical light phase-contrast imaging has been used for many years. By mathematically applying wave optics instead of ray optics in X-ray problems, phase information becomes apparent [24]. PCI is a technique that has been recently developed that detects X-ray phase changes in the form of intensity measurements that are caused by X-ray-material interactions. All materials have a complex refractive index $n = 1 - \delta + i\beta$, where δ is the phase coefficient and β is the absorption coefficient, as will be described in section 2.5.4. Absorption X-ray radiology, as mentioned in section 2.1, retrieves the absorption component of the object; whereas PCI measures the changes in phase coefficient along with the absorption coefficient [25]. PCI offers higher sensitivity in early detection of breast cancer because breast carcinoma's phase shift and the surrounding tissue's phase shift are around 3 magnitudes greater than the linear attenuation coefficients [26]. There are many different types of PCI techniques, which include interferometry-based [5, 6], analyzer-based [27, 28] and propagation-based [4] PCI. Most of the PCI techniques, such as interferometry-based and analyzer-based, are composed of complex optics that can lead to misalignment and reduced flux [15]. Propagation-based PCI is the only method that does not require any complex optical components. For this reason, the work done in this thesis was completed using propagation-based PCI.

Phase-contrast can be considered an aberration to the imaging system as it no longer truly represents the object that is being imaged, even though it can aid in visualizing objects that weakly absorb X-rays. It is important to quantitatively recover information from the image by performing algorithms called phase retrieval. Currently there is no direct method of recovering quantitative information from the detector. The detector is only capable of measuring an intensity image and not the phase shift [29]. Phase retrieval will be further described in Chapter 3.

The phase shift is a fundamental piece of information that is being retrieved from a phase-contrast image. The phase shift is related to the phase coefficient δ, the electron density $\rho_e(\mathbf{r}_\perp)$ and the projected electron density $\rho_{e,p}(\mathbf{r}_\perp)$ as follows [4]:

$$\phi(\mathbf{r}_\perp) = -\frac{2\pi}{\lambda}\int \delta(\mathbf{r}_\perp, z)dz == -\frac{2\pi r_e}{k}\int \rho_e(\mathbf{r}_\perp)dz = -\lambda r_e \rho_{e,p}(\mathbf{r}_\perp), \tag{2.2}$$

where the wavevector $k = 2\pi/\lambda$, r_e is the classical electron radius and the integral is integrated over the propagation direction.

For homogeneous objects, this expression can be simplified and expressed in terms of

projected object thickness $T(\mathbf{r}_\perp)$ [18]:

$$\phi(\mathbf{r}_\perp) = -T(\mathbf{r}_\perp)\delta\frac{2\pi}{\lambda}. \tag{2.3}$$

These equations are fundamental for retrieving the phase or thickness in an image.

2.2.1 Interferometry-Based Phase-Contrast X-ray Imaging

In 1965, U. Bonse and M. Hart designed the Laue-Case X-ray interferometers [6]. The same year, they suggested that this device can be used for the purpose of X-ray phase-contrast micrography to image biological materials. This method requires three crystals, where each crystal serves a different purpose: a beam splitter, a transmission mirror and an analyzer crystal, as seen in Figure 2.1 [5]. The beam splitter splits the beam by way of

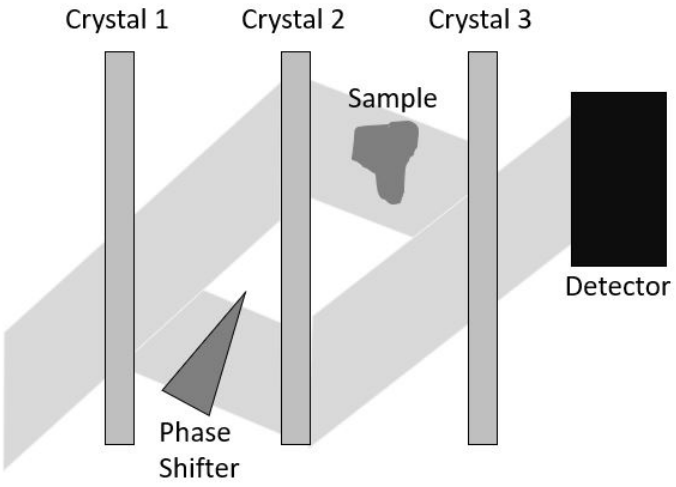

Figure 2.1: Interferometry-Based Phased Contrast X-ray Imaging

a symmetrical Laue reflection, the transmission mirrors reflect the two beams back toward each other and the analyzer crystal combines the beams. The detector is placed close to the analyzer crystal, and the sample is placed between the transmission mirror crystal and the analyzer crystal. In order to retrieve the phase in this method, it is a modulo 2π, therefore unwrapping the phase from the image. This method of phase retrieval is simple and does not require intensive physics and math. The drawback to this method is that it

requires complex optics in order to acquire an image, which is impractical in the clinical setting and could cause for misalignment [30].

2.2.2 Analyzer-Based Phase-Contrast X-ray Imaging

Analyzer-based phase-contrast X-ray imaging, also known as diffraction-enhanced imaging, takes advantage of small angle X-ray scattering using a single-reflection crystals. It applies similar concepts to interferometry-based method (see section 2.2.1) that U. Bonse and M. Harts developed, but their method requires a multiple-crystal arrangement. In the analyzer-based method, a perfect crystal analyzer is placed after the sample that is being illuminated by either a laboratory or synchrotron source and the X-rays that are reflected in the crystal are recorded on a detector. In order to create lateral coherence of the beam, a monochromator is used that is set at the Bragg angle that corresponds to the desired energy. The general setup for the analyzer-based phase-contrast X-ray imaging method is presented in Figure 2.2. Generally, this method is performed using a synchrotron source

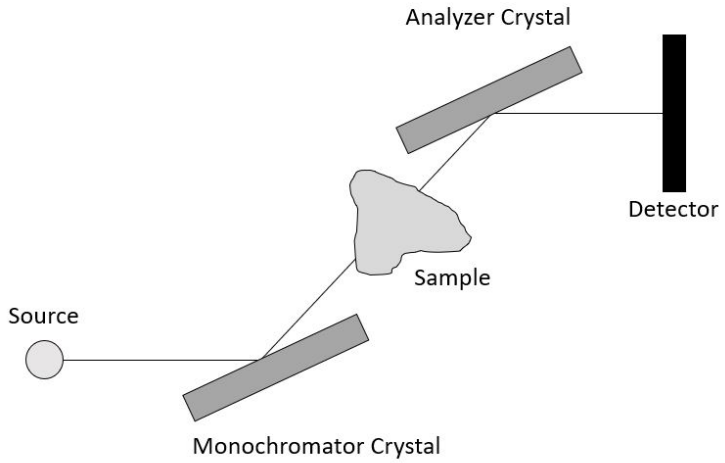

Figure 2.2: Analyzer-Based Phased Contrast X-ray Imaging

because its spectra that is extremely intense, highly collimated and tuneable over a wide energy range [27]. In 2014, Zhou et al. proposed a system using a micro-focus X-ray source. There are a number of obstacles that make it difficult to integrate the analyzer-based method with a conventional X-ray tube source, such as system alignment stability due to the rotating anode vibration and thermal variations. For this reason, Zhou et

al. have to include three enclosures in order to eliminate mechanical vibrations and to maintain constant temperature. Another drawback to this system is that it requires long acquisition time, which also results in a higher dose [28].

2.2.3 Propagation-Based Phase-Contrast X-ray Imaging

Propagation-based phase-contrast X-ray imaging, also known as inline phase-contrast X-ray imaging, is the simplest form of PCI as it only requires a source and a detector, as seen in Figure 2.3. The source is placed at a distance R_1 from the object, also known as the source-to-object distance (SOD). The detector is a placed at a distance R_2 from the object, also known as the object-to-detector distance (ODD). When the X-rays hit the object, the object's interfaces introduce a phase shift and the detector records the intensities of the X-rays. The intensity values contain both the phase and attenuation coefficient of the object. In order to quantitatively assess the image, the phase and attenuation coefficient must be separated by mathematically filtering the intensity image using analytically intensive phase retrieval algorithms.

The only criterion that is required for propagation-based PCI is that its chosen param-

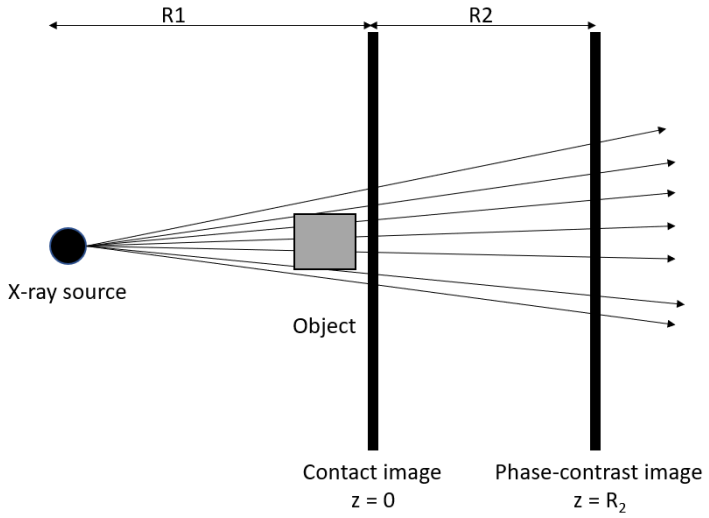

Figure 2.3: Propagation-based Phased Contrast X-ray Imaging

eters for acquisition must satisfy the following relation [9]:

$$\frac{L_{shear}}{L_{\perp}} = \frac{R_2 s|\mathbf{u}_{\perp}|}{MR_1} = \frac{(M-1)s|\mathbf{u}_{\perp}|}{M} << 1 \tag{2.4}$$

where $L_{shear} = \lambda R_2|\mathbf{u}_{\perp}|/M$ is the phase space shearing length, $L_{\perp} = \lambda R_1/s$ is the transverse coherence length, s is the source size, $M = (R_1 + R_2)/R_1$ is the magnification factor, $\mathbf{u}_{\perp}$ is the spatial frequency. If this equation is satisfied, edge enhancement will be easily visible. Since the microfocus source has a small spot size (5 µm - 10 µm), this relation is easily satisfied for small SOD and ODD [9].

Due to the simplicity of the setup for propagation-based PCI compared to all the other PCI methods, this method is investigated in this thesis.

2.3 Mammography

Breast cancer is the leading cause of death in women and accounts for one-quarter of all existing cancers. Currently, absorption X-ray imaging is the method used in mammography to detect cancer in breast tissue, but it is known to have low specificity and sensitivity. Breast density is directly correlated to the risk of developing breast cancer. The higher the breast density, the higher the chance of developing breast cancer [29]. Approximately 40-50 percent of women between the ages of 40 to 74 in the United States have dense breasts, therefore making it difficult to diagnose cancer with conventional absorption X-ray imaging [31]. The one issue is that it is difficult to image carcinoma in dense breasts with current imaging methods because the linear attenuation coefficient of cancerous tissue is similar to that of glandular tissue since they are similar composition; whereas adipose (fat) and glandular tissue is easy to differentiate. At lower energies (10-15 keV), carcinoma and glandular tissue have the highest contrast and it becomes much poorer at higher energies ($>$ 35 keV). Low energies require higher dose due to higher tissue absorption and longer exposure times. Calcium hydroxyapatite or calcium phosphate deposits can form within the breast, but these calcifications are usually benign. There are two categories of breast calcifications, which are macrocalcifications and microcalcification. Macrocalcifications are not cancerous and appear as large white dots. Microcalcifications are small calcium deposits that can indicate precancerous cells or early breast cancer if clustered, but are generally also non-cancerous. Current technology is able to image microcalcifications as small as 0.1 mm or less [29]. Calcifications are easier to visualize than cancerous tissue in glandular tissue as their linear attenuation coefficients are much different.

PCI offers opportunity for diagnosing cancer in dense breasts with higher sensitivity and specificity as it can characterize weakly absorbing objects, such as enhancing soft-tissue contrast and improving visualization of cancerous structures. This method overcomes the obstacles found in absorption X-ray mammography and has received considerable attention and can increase the early detection of breast cancer diagnoses, enabling earlier treatment and increasing survivability of women.

2.4 Computed Tomography

X-ray computed tomography (CT) is a commonly used three-dimensional X-ray imaging technique, where either the detector and source rotate around the object or the object is rotated and the detector and source remain stationary. Initially developed in the 1970s, CT has advanced greatly in terms of speed of acquisition and technology. Currently, CT imaging is only commercially used with absorption X-ray imaging, therefore soft tissue differentiation is not that high and some other image modalities perform better, such as positron emission tomography (PET) or magnetic resonance imaging (MRI). Ultrasound offers a better spatial resolution to CT when only a shallow region of interest is required to be imaged. Regardless of these drawbacks, it is one of the most robust imaging modality methods for the vast majority of clinical applications. CT systems use polychromatic sources and an X-ray detector based on energy integration or photon counting. CT system can take up to 360 two-dimensional (2D) slices. The slices have to be further processed using an algorithm method called reconstruction in order to produce the final 3D image. The most common reconstruction method that is used is called the Feldkamp-Davis-Kress (FDK) reconstruction algorithm [29].

PCI can improve contrast of different types of soft tissues and allow for soft tissue differentiation. This imaging modality could revolutionize the current CT systems, improve diagnosis and possibly replace PET and MRI for certain medical applications. PCI CT requires an addition post-processing step that occurs before reconstruction called phase retrieval, which creates a quantitative image.

2.5 X-ray Interaction

X-rays interact in many different ways. Their interactions can result in a local deposition of energy. The X-ray sometimes will exit after the interaction as a scattered X-ray or a characteristic X-ray. Some types of X-ray interactions are Compton scattering, the

photoelectric effect and Rayleigh scattering. All of these X-ray interactions are combined to form the complex refractive index. In this section, different types of X-ray interactions will be explained, along with the complex refractive index.

2.5.1 Compton Scattering

Compton scattering, also known as incoherent scattering, increases as the X-ray energy increases. Compton scattering causes the photon to change momentum and transfer an amount of energy to a scattering electron. The amount of energy that is transferred to the electron depends on the angle at which the photon interacts with it. It becomes the dominate scattering event for X-ray energies that are greater than 60 keV. At these energies, attenuation by the object is negligible and the phase parameter becomes the dominating factor of the refractive index. The Klein-Nishina formula is used to calculate the total cross-section for an X-ray photon Compton scattering from a single free electron, σ_{KN} [32]:

$$\sigma_{KN} = 2\pi r_e^2 \left\{ \frac{1+\eta}{\eta^2} \left[\frac{2(1+\eta)}{1+2\eta} - \frac{1}{\eta} \ln(1+2\eta) \right] + \frac{1}{2\eta} \ln(1+2\eta) - \frac{1+3\eta}{(1+2\eta)^2} \right\} \qquad (2.5)$$

where $\eta = E_{photon}/m_e c^2$, r_e is the classic radius of an electron ($2.82\text{x}10^{-15}$), m_e is the mass of an electron ($9.11\text{x}10^{-3}1$ kg) and c is the speed of light, as mentioned before. $m_e c^2$ is the resting energy of an electron and is equal to 511 keV.

2.5.2 Photoelectric Effect

The photoelectric effect dominates at lower X-ray energies. The photon transfers its energy to an electron, and, due to the conservation of momentum and energy, the electron is ejected from the atom. Thus, the atom is ionized. The attenuation due to the photoelectric effect is energy dependent as $\mu \ \alpha \ E^{-3}$.

2.5.3 Rayleigh Scattering

Rayleigh scattering is a coherent type of scattering. It increases as the X-ray energy decreases and with increasing atomic number of the sample. This occurs when there is no energy transferred to the electron and the photon energy is less than the electron binding energies. Coherent scattering is defined by the forward scattering factors, f_1^0 and f_2^0, that

are used to define the complex refractive index. The values for the forward scattering factors are tabulated for a wide range of photon energies and chemical elements on the National Institute of Standards and Technology (NIST) website [33, 34]. f_1^0 can be approximated as the atomic number of the element, Z.

2.5.4 Complex Refractive Index

The complex refractive index is describe as:

$$n = 1 - \delta + i\beta \tag{2.6}$$

where δ is the phase coefficient and β is the absorption coefficient.

The phase coefficient is on the order of 10^{-6} for most materials and therefore also has small refraction angles that allows X-ray trajectories to be approximated as straight lines. The absorption coefficient is on the order of 10^{-9} for most low density materials. The phase shifts of biological materials are around three magnitudes greater than the linear attenuation coefficients [26].

For objects of known material, the refractive index decrements can be calculated using the following formulas [35]:

$$\delta = \frac{r_e h^2 c^2}{2\pi E^2} \sum_Z n_Z f_{1Z}^0(E) \tag{2.7}$$

$$\beta = \frac{r_e h^2 c^2}{2\pi E^2} \sum_Z n_Z f_{2Z}^0(E) \tag{2.8}$$

where r_e is the classical electron radius, h is Planck's constant, c is the speed of light, E is the photon energy of the X-ray beam, Z is the atomic numbers of all elements present in the material, and f_{1Z}^0 and f_{2Z}^0 are forward scattering factors. The attenuation coefficient is proportional to energy as $\frac{1}{E^3}$ and the phase coefficient is proportional to energy as $\frac{1}{E^2}$. In clinical imaging, attenuation arises from the three scattering mechanisms mentioned in sections 2.5.2, 2.5.3 and 2.5.1, which are the photoelectric effect, Comptom scattering and Rayleigh scattering [32].

The absorption coefficient β is related to the linear attenuation coefficient μ with the following expression, where λ is the X-ray wavelength:

$$\beta = \frac{\lambda}{4\pi}\mu = \frac{hc}{4\pi E}\mu. \tag{2.9}$$

The projected linear attenuation coefficient over a sample can be defined by the following equation:

$$\mu(x, y) = \frac{4\pi}{\lambda} \int \beta(x, y, z) dz \tag{2.10}$$

These fundamental equations will be used in this thesis to define material properties.

2.6 Mechanisms of X-ray Radiation

A form of ionizing electromagnetic radiation that can liberate electrons from atoms because of their high energy are X-rays. Two X-ray generation mechanisms, Bremsstrahlung radiation and characteristic X-rays, will be discussed in this section.

2.6.1 Bremsstrahlung Radiation

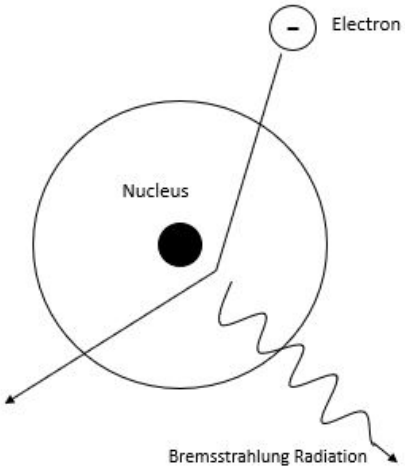

Figure 2.4: Bremsstrahlung Radiation

Bremsstrahlung radiation, also known as braking radiation, is produced by electrons interacting with the Coulomb field of the target atoms' nucleus, which causes them to undergo

deceleration. Bremsstrahlung radiation is dependent on the atomic number of the material being bombarded Z, the charge incident on the target nuclei ze and the mass of the charged particle bombarding the target m. Thus, intensity of Bremsstrahlung is proportional to the following expression:

$$I_{Bremsstrahlung} \propto \frac{Z^2 z^4 e^6}{m^2} \tag{2.11}$$

As the atomic number of the target material increases, the intensity of Bremsstrahlung increases, therefore high atomic number targets are preferred for X-ray generation. Also, as the mass of the charged particle bombarding the target increases, the intensity of Bremsstrahlung radiation decreases. For this reason electrons are preferred since their mass is around four magnitudes less than alpha particles and protons. An electron that has a glancing angle of incidence atomic coulomb field will only emit a small amount of X-ray energy; whereas an electron that interacts with the atom will transfer all of its kinetic energy and produce an X-ray of equivalent energy, as seen in Figure 2.4 [36].

2.6.2 Characteristic X-rays

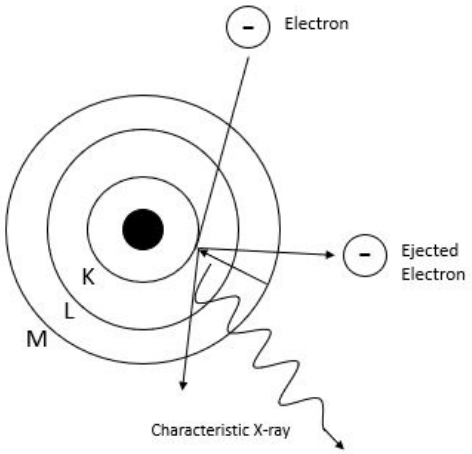

Figure 2.5: Characteristic X-rays

Characteristic X-rays are produced when electrons interact with other atomic electrons in the target, compared to Bremsstrahlung X-rays that are produced when the electron interacts with the nucleus of the atom.

Electrons are bound to the nucleus of the atom through charge-charge interactions, and occupy orbitals of specific quantized energy as represented in the Bohr model of an atom. The innermost shell is called the K-shell and is occupied by two electrons that have approximately the same binding energy. The next shell is called the L-shell and is occupied by eight electrons that are bound to the nucleus with approximately the same binding energy.

An electron will bombard an atomic electron with binding energy less than or equal to its kinetic energy. This will cause the K-shell electron to eject from its shell, leaving a vacant spot in the innermost shell. An atomic electron from a different shell will fill this vacancy and leave a vacancy in a different shell, which will be filled by another atomic electron that will also leave a vacancy in another shell. This leads to a cascade effect of electrons filling vacancies in lower shells, leaving vacancies in more distant outer shells. Once all shells are filled except for the outer shell, free electrons from the environment will fill the outermost shell. The general process is shown in Figure 2.5. The transition of an electron from an upper shell to a lower shell causes energies to be emitted in the form a X-ray energy. An electron moving from the L-shell to the K-Shell is called a K_α emission because the electron is moving into the K-shell and is making an α transition (coming from the next shell up).

Thus, X-rays that are emitted from this sequence of atomic electrons moving due to the bombardment of a free electron that ejects an atomic electron are called characteristic X-rays. Every element has its own characteristic binding energies, making the energies of the X-rays emitted characteristic to each atom [36].

2.7 X-ray Source

The typical energy range for diagnostic X-rays is 10 keV to 150 keV. The wavelengths these energies correspond to is between 0.0083 to 0.124 nm. The relationship between energy and wavelength λ is given by:

$$E = \frac{hc}{\lambda} \tag{2.12}$$

where h is Planck's constant (4.135 x 10^{-15} eV·s) and c is the the speed of light (2.997925 x 10^8 m/s). The most common source of X-ray generation is the standard X-ray tube that

emits Bremsstrahlung and characteristic X-rays. One of the most common sources used in phase-contrast imaging is the synchrotron source. Both will be described below [29].

2.7.1 Synchrotron Source

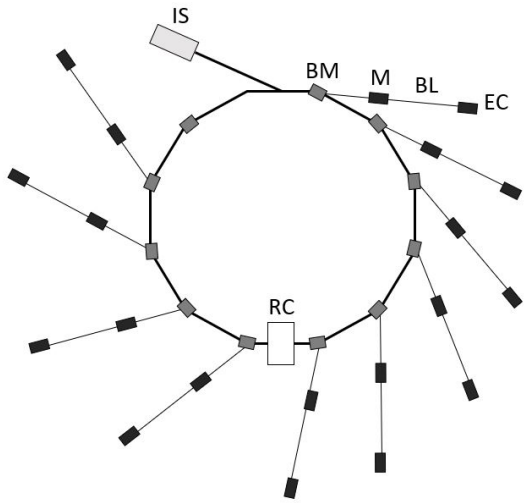

Figure 2.6: Generic scheme of a synchrotron source. IS = injector system; M = monochromator; BL = beamline; EC = experimental chamber; BM = bending and focusing magnet; RC = radiofrequency cavity.

Synchrotron sources produce a monochromatic X-ray spectrum, meaning that it emits one specified X-ray energy. A generic synchrotron facility is shown in Figure 2.6. The synchrotron source works on the basis of electron acceleration. There is an injector system that produces and pre-accelerates the electrons to a speed that is close to the speed of light. The electrons are sent into a closed path ultra-high-vacuum chamber by focusing and bending magnets. As the electron is circulating, it emits X-rays that are collected by beamlines and sent through a monochromator to filter out all undesirable X-ray energies. The monochromatic X-ray spectrum is emitted to the experimental chamber. The X-rays are emitted due to the way the magnets act on the electrons. The bending magnets cause a centripetal acceleration to the electrons so they remain in the closed path. The change in acceleration gives off energy in the form of X-rays due to the conservation of energy and momentum.

2.7.2 X-ray Tube

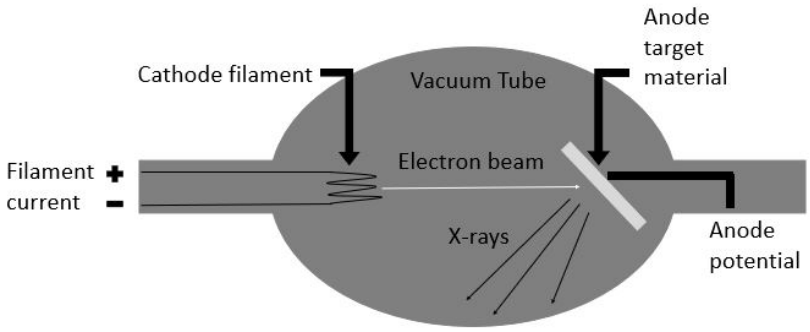

Figure 2.7: General schematic of an X-ray tube

Generally, X-ray tubes contain a vacuum environment to ensure that the energetic electrons will bombard with the target instead of air molecules, since air molecules would decrease the X-ray efficiency. The target is the anode and is positively-charged where the electrons bombard to produce X-rays. The typical material used for the anode found in diagnostic X-ray imaging applications is tungsten. The cathode is negatively-charged and is the source of the electrons that are bombarding the anode target. Inside the cathode is a filament, which heats up during X-ray exposures and electrons are emitted through a process called thermionic emission. Thermionic emission is the emission of electrons from a heated source. The high voltage between the anode and cathode causes the electrons to accelerate towards the target and bombard to produce X-ray energy. A general schematic for an X-ray tube is shown in Figure 2.7.

In X-ray diagnostics, electron volt is commonly used to define the amount of energy the X-ray has. One electron volt is equivalent to $1.602\text{x}10^{-19}$ Joules. One electron volt can be defined as the kinetic energy of an electron accelerated by an applied potential of one volt. This is different than the tube potential, which is expressed in volts. The tube potential controls the X-ray energy and the current in the filament controls the number of electrons being emitted from the cathode.

A small number of the X-rays produced are via Bremsstrahlung and characteristic radiation mechanisms (see sections 2.6.1 and 2.6.2). The majority of the X-rays produced are due to an electron transferring a fraction of its kinetic energy to the atomic electron and as the target atom relaxes, it emits infrared radiation, therefore generating heat. The

heat produced by this mechanism places a limit on the power density of the focal spot size, which can impacts the spatial resolution in phase-contrast X-ray imaging [36].

Polychromatic X-ray source is more accessible than a monochromatic X-ray source because of its lower cost and is used in conventional absorption-based X-ray radiography. Wilkins et al. describe that a conventional polychromatic microfocus X-ray tube source is well suited for propagation-based phase-contrast X-ray imaging [4]. For this reason, the polychromatic source is used in this thesis.

2.8 X-ray Detector

X-ray detection was first performed on a photosentive X-ray film, where the process of image storage was based on chemical reaction of silver salt when the film interacts with X-rays. The film, itself, would act as the display. Within the past couple of decades, films are being replaced with digital technology. Using digital detectors permits characteristics of the final image to be tuned on a standalone computer. Digital X-ray detectors absorb the X-ray in the form of an electrical signal, which is collected and digitized [29]. The digital X-ray detectors are classified as either direct or indirect conversion, described in sections 2.8.1 and 2.8.2. There are two common digital detectors: charged-coupled device (CCD) and complementary metal-oxide-semiconductor (CMOS).

CCDs were invented in 1970 by Boyle and Smith [37]. CMOS technology, although first presented in the 1960s, could not compete in the past with CCD technology. It was not until the early 1990s when CMOS technology re-emerged as a substitute for CCD technology. The first generation of CMOS had passive pixel arrays (PPA). In the late 1990s, CMOS Active Pixel Sensors (APS) emerged and offered lower noise readout, higher readout speed and improved scalability to large arrays compared to PPA. For the longest time, CCD technology had many qualities that the CMOS technology could not compete with, such as higher fill factor, smaller pixel size and larger format. The CCD technology has its limitations as well. It requires several watts for its basic functioning. Its analog readout and digital control electonics cannot be on the same integrated circuit, unlike CMOS technology. Also, they cannot function over the whole temperature range or lighting conditions required for specific applications. CMOS technology is able to be integrated into very-large-scale integrate electronics on a chip, which can reduce the cost of packaging and components. To this date, CMOS technology has demonstrated quantum efficiency, dynamic range and noise comparable to CCDs. Both technologies have their advantages and disadvantages depending on the application [38]. In this thesis, a 7.8 µm pixel pitch amorphous selenium (a-Se) direct conversion CMOS X-ray imager will be used that was

designed within the Silicon Thin-filmed Applied Research (STAR) group at the University of Waterloo.

An important parameter of detectors is their quantum detection efficiency. The quantum detection efficiency η is defined as the efficiency of a detector to convert incident X-ray energy into a signal to form an image. It depends on the attenuation of the detector μ_{det} and the thickness of the detector's active region d:

$$\eta = 1 - \exp\big[-\mu_{det}(E)d\big] \tag{2.13}$$

The quantum efficiency increases as the active region thickness, the detector material density and/or atomic number increases.

2.8.1 Direct Detector

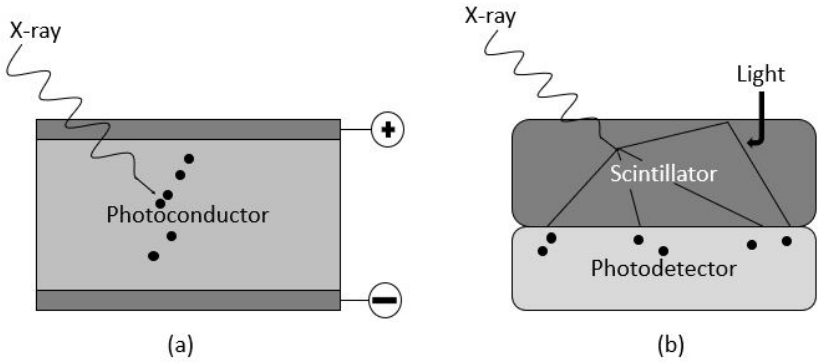

Figure 2.8: Schematic of (a) direct conversion detector and (b) indirect conversion detector.

Direct detectors work on the principle of atom ionization and change in current or voltage as depicted in Figure 2.8 (a). There is a photoconductor placed between two electrodes, where one of the electrodes is pixelated. In the absence of X-rays, the photoconductor acts as an insulator and no charge is transferred to the electrodes. When an X-ray hits the photoconductor, an electron is promoted to the conduction band and becomes conductive. The conductive electrons then move to the upper and lower electrode. The accumulated charge on the electrodes is measured electronically. Examples of direct detectors are: selenium (Se), cadmium zinc telluride (CdZnTe) or mercury iodide (HgI_2) detectors, xenon detectors and film detectors with no intensifying screen [36].

2.8.2 Indirect Detector

Indirect detectors are scintillator-based, which means the material fluoresces when a high-energy photon hits it as illustrated in Figure 2.8 (b). When an X-ray hits a phosphor, this causes the phosphor to emit photons in or near the visible light range. These visible light photons propagate to a photodetector by a phenomenon called optical diffusion, and from this the photodetector arrays, CCD or thin-film transistor (TFT) records the pattern from the visible light photons. Examples of detector compositions are: cesium iodide (CsI), gadolinium oxysulfide (Ga_2O_2S) and calcium tungstate ($CaWO_4$).

Chapter 3

Phase Retrieval

All PCI techniques require a post-image processing method referred to as phase retrieval because the intensity image produced by the detector is only qualitative since it contains both the phase and absorption information. In order to retrieve quantitative data about the sample, the phase must be unwrapped from the intensity data. For most PCI methods, the post-processing method is relatively simple and only requires an unwrapping of the 2π phase shifts. On the other hand, propagation-based PCI has a more mathematically intensive method of retrieving the phase [15].

A retrieved phase map is useful for tissue characterizations in medical imaging. A phase map of a breast can compute the volumetric breast density for use in mammography and cancer diagnosis (volume of fraction of fibroglandular tissue in the breast) [22].

Phase retrieval was first used in the 1940s in X-ray crystallography, although these techniques only apply to small molecules. In the late 1970s and early 1980s, methods were developed that were used in general imaging and since then these methods have been used in electron microscopy, wavefront sensing, astronomy and X-ray imaging. Phase retrieval is a nonlinear inverse problem that separates the phase and attenuation component from an intensity image [39]. Most inverse problems, such as phase retrieval, are mathematically ill-posed. The best known inverse problem is deconvolution, which, in imaging, can be stated as an image deblurring problem [17].

There exists two categories of phase retrieval in propagation-based phase-contrast X-ray imaging: indirect and direct methods. Indirect methods are iterative approaches that are used when a correlation between the measurement and wavefield is difficult to compute mathematically; whereas direct methods are non-iterative approaches that express the solution as a explicit function of the input data or use a deterministic algorithm. Direct

methods can be further broken down into two categories: multi-image methods or single-distance methods. Multi-image methods require two or more images to be acquired either at two or more distances or by using two or more different spectrums for each image. Quantitative phase retrieval using transport of intensity equation (TIE)-based algorithms and multiple defocused images suffers when using an X-ray source due to variation in the incident illumination; whereas using visible light or electrons as the source, quantitative phase retrieval has been successful. Flat-field correction can be applied to compensate for the incident intensity, but it cannot correct for changes in the phase distribution that are present in the incident illumination [40].

Single distance methods require *a priori* information and assumptions to be made that include assumptions based on the material and/or wave propagation. Many of the existing methods begin with the paraxial or parabolic wave equation, using the Fresnel diffraction integral as a solution to the paraxial wave equation. Using the assumption that the wave will propagate over a short distance, this equation turns into the TIE. This is a common starting point to derive many phase retrieval methods in PCI, and it is used as the starting point for Paganin's method, one of the most well-known phase retrieval methods for propagation-based PCI [41, 42]. Another common starting point is using the contrast transfer function (CTF), which is derived by assuming a slowly varying phase shift. CTF is based on first-order Taylor expansion of the intensity with respect to the wave and the forward model of CTF is a linearization of the transmittance function [15, 16].

3.1 Transport of Intensity Equation

As mentioned previously, the TIE is a solution to the paraxial wave equation. It is derived under the assumption of a paraxial beam propagating along the z-axis over a short distance. The complex amplitude of an object can be represented by $\sqrt{I(\mathbf{r})}\exp\left[ik\phi(\mathbf{r})\right]$, where k is the wavenumber, $I(\mathbf{r})$ is the intensity, $\mathbf{r}$ is the spatial coordinates (x, y) and ϕ is the phase. The TIE can be described as the derivative of intensity propagating along the z-axis that contains the phase information as described in the following equation, where ∇ is the Laplacian that applies only to the lateral coordinates (x, y) [41]:

$$\nabla \cdot (I(\mathbf{r}_\perp, z)\nabla\phi(\mathbf{r}_\perp, z)) = -\frac{2\pi}{\lambda}\frac{\partial}{\partial z}I(\mathbf{r}_\perp, z). \tag{3.1}$$

TIE can be derived in many different ways. One derivation is by using the Fresnel wave propagation formula assuming small propagation distance, as mentioned above. It can also

be derived from the Helmholtz equation under the paraxial approximation or through the Poynting theory as in the following equation:

$$-k\frac{\partial I(\mathbf{r}_\perp)}{\partial z} = \nabla I(\mathbf{r}_\perp)\cdot\nabla\phi(\mathbf{r}_\perp) + I(\mathbf{r}_\perp)\nabla^2\phi(\mathbf{r}_\perp). \tag{3.2}$$

The first term on the right-hand side (RHS) of the equation is called the prism term and corresponds to the longitude intensity due to the local wavefront slope; whereas the second term on the RHS is called the lens term and corresponds to intensity variations caused by the local wavefront curvature.

Using first order approximations on the left-hand side (LHS) of Eq. 3.2 and breaking down the RHS, the following approximation can be derived [43]:

$$-k\frac{I_{\delta z}(x,y) - I(x,y)}{\delta z} = \nabla I(x,y)\nabla\phi(x,y) + I(x,y)\nabla^2\phi(x,y) \tag{3.3}$$

Eq. 3.3 is the final TIE, which is an elliptical partial differential equation of the phase ϕ.

If two images are acquired at different propagation distances, each resulting in different $I(x,y)$, this allows for $\partial I(x,y)/\partial z$ to be estimated. Thus, the phase can be determined uniquely if the boundary conditions are specified.

Boundary conditions are not easy to determine, which make rigorous implementation of the TIE phase retrieval difficult. The boundary conditions are generally based on *a priori* information. The easiest boundary conditions that can be implemented is if the sample is in the center of the field of view and not touching the edges of the image. In this case, homogeneous Dirichlet or Neumann boundary conditions can be applied, or periodic boundary conditions can be considered and, thus, the fast Fourier transform (FFT)-based TIE solvers can be used. These methods can only be used in a limited number of cases. If the object is located at the image border, these methods can no longer be implemented and defining boundary conditions becomes difficult [43].

The most well-known fast TIE solver is Paganin's method, which is described in 3.3. This method uses FFT to solve the inverse Laplacian operator, which implies periodic boundary conditions and forces the phase outside the domain to be periodically extended. The periodic assumption can cause serious boundary error across the reconstructed phase if the opposite boundaries of the true phase distribution match poorly. In most cases, Paganin's method works without any problems, but it has its restrictions, which will be described in 3.3 [43].

3.2 Contrast Transfer Function

The CTF is derived using a Born-type approximation. It gives a solution that is identical to that was used in electron microscopy derived by Guigay. Since the Born-type approximation is used, it makes this equation more restrictive to use than TIE. Like the TIE, it depends on wavelength, feature size and propagation distance, but it also has the restrictive requirement that the object is purely phase with little to no absorption [44]. To derive the CTF, first the transmission equation is used:

$$U(\mathbf{r}_\perp) = U_0 \exp(-\mu(\mathbf{r}_\perp) + i\phi(\mathbf{r}_\perp)) \tag{3.4}$$

where $U(\mathbf{r}_\perp)$ is the transmission function and $I_0 = |U_0|^2$ is the intensity of a plane wavefield incident on the object. Using the Born-type approximation of $\mu << 1$ and $|\phi| << 1$ and using first order Taylor expansion, the transmission function can be simplified to the following:

$$U(\mathbf{r}_\perp) = U_0(1 - \mu(\mathbf{r}_\perp) + i\phi(\mathbf{r}_\perp)). \tag{3.5}$$

Next, the propagated wavefield ψ is calculated:

$$\psi(\mathbf{r}_\perp, z) = \mathcal{F}^{-1}\left[\exp\left(-i\frac{z\mathbf{u}_\perp^2}{2k}\right)\mathcal{F}\left(1 - \mu(\mathbf{r}_\perp) + i\phi(\mathbf{r}_\perp)\right)\right] \tag{3.6}$$

where $\mathcal{F}^{-1}$ is the inverse Fourier transform, $\mathbf{u}_\perp$ is the spatial frequency, z is the propagation distance and k is the wavenumber. Using the identity $\exp(-ix) = \cos(x) - i\sin(x)$, the propagated wavefield can be expressed as:

$$\psi(\mathbf{r}_\perp, z) = 1 + \mathcal{F}^{-1}\left[\left(\cos\left(\frac{z\mathbf{u}_\perp^2}{2k}\right) - i\sin\left(\frac{z\mathbf{u}_\perp^2}{2k}\right)\right)\left(i\tilde{\phi} - \tilde{\mu}\right)\right]. \tag{3.7}$$

where $\tilde{\phi}$ is the Fourier transform of the phase coefficient and $\tilde{\mu}$ is the Fourier transform of the attenuation coefficient.

Using Fourier transform convolution theorem, the intensity $|\psi|^2$ can be calculated:

$$|\psi|^2 = 1 + 2\phi * \mathcal{F}^{-1}\left(\sin\left(\frac{zu_\perp^2}{2k}\right)\right) - 2\mu * \mathcal{F}^{-1}\left(\cos\left(\frac{zu_\perp^2}{2k}\right)\right) \tag{3.8}$$

where $*$ denotes the convolution. The intensity in Fourier space $\tilde{I}$ can be approximated as:

$$\tilde{I}(u_\perp, z) \approx 2\pi\delta_D(u_\perp) + 2\tilde{\phi}(k_\perp)\sin\left(\frac{zu_\perp^2}{2k}\right) - 2\tilde{\mu}(k_\perp)\cos\left(\frac{zu_\perp^2}{2k}\right) \tag{3.9}$$

where $\delta_D(u_\perp)$ is the Dirac delta function. Eq. 3.9 is the final CTF equation in Fourier space.

This approximation is valid for the weak object approximation that was defined by the Born-type approximation. Also, it is valid for a pure phase object, where $\mu(\mathbf{r}_\perp) \approx 0$ and the slowly varying phase approximation $|\phi(\mathbf{r}_\perp) - \phi(\mathbf{r}_\perp + \lambda z \mathbf{u}_\perp/2\pi)| << 1$ are satisfied, or for a homogeneous object where $\delta \propto \beta$ and $\mu(\mathbf{r}_\perp) << 1$ [45].

3.3 Paganin's Method

Paganin et al. developed a non-iterative phase retrieval algorithm that is based on TIE and requires a single image [18]. This method is valid for homogeneous objects of known composition in the near Fresnel region, which is defined as $\lambda z u^2 << 1$ where λ is the wavelength, z is the propagation distance and u is the spatial frequency of the detector plane. Paganin developed an algorithm that is able to retrieve the projected thickness of the object using a single defocused image.

The derivation begins with the TIE, which is described by Eq. 3.1. Using Eq. 2.1 and Eq. 2.3 to describe the intensity and phase of the radiation over the plane at the exit surface, these equations are substituted into Eq. 3.1 to obtain:

$$\frac{\partial}{\partial z} I(\mathbf{r}_\perp, z = 0) = -\frac{\delta}{\mu} \nabla^2 \exp\big(-\mu T(\mathbf{r}_\perp)\big). \tag{3.10}$$

Next, the LHS of the equation is estimated using two intensities that are separated by a distance R_2, which is also known as the ODD:

$$\frac{\partial}{\partial z} I(\mathbf{r}_\perp, z = 0) \approx \frac{I(\mathbf{r}_\perp, z = R_2) - \exp\big(-\mu T(\mathbf{r}_\perp)\big) I^{in}}{R_2}. \tag{3.11}$$

Substituting Eq. 3.11 into 3.10 and using the Fourier transform identity of the Laplacian $\mathcal{F}[\nabla^2 \exp(-\mu T(\mathbf{r}_\perp))] = -\mathbf{u}_\perp^2 \mathcal{F}[\exp(-\mu T(\mathbf{r}_\perp))]$, the following expression can be achieved with re-arrangement:

$$\mathcal{F}\left\{\exp\big(-\mu T(\mathbf{r}_\perp)\big)\right\} = \mu \frac{\mathcal{F}\left\{I(\mathbf{r}_\perp, z = R_2)\right\}/I^{in}}{4\pi^2 R_2 \delta |\mathbf{u}_\perp|^2 + \mu} \tag{3.12}$$

where $T(\mathbf{r}_\perp)$ is the projected thickness of the sample at a given position, μ is the attenuation coefficient, δ is the phase coefficient, $\mathbf{u}_\perp$ is the spatial frequency, I_{in} is the incident intensity

acquired at the object plane, $I(\mathbf{r}_\perp, z = R_2)$ is the intensity image of the object acquired at the detector plane.

Rearranging Eq. 3.12 and taking into account magnification $M = (R_1 + R_2)/R_1$ from point-source illumination, Paganin et al. came up with this final thickness retrieval expression for a homogeneous object:

$$T(\mathbf{r}_\perp) = -\frac{1}{\mu} \ln \left(\mathcal{F}^{-1} \left\{ \mu \frac{\mathcal{F}\left\{M^2 I(\mathbf{r}_\perp, z = R_2)\right\}/I_{in}}{4\pi^2 \frac{R_2}{M} \delta |\mathbf{u}_\perp|^2 + \mu} \right\} \right) \tag{3.13}$$

Paganin's method can be related to the phase shift caused by the object by substituting Eq. 2.3 into Eq. 3.13:

$$\phi(\mathbf{r}_\perp) = \frac{\delta}{2\beta} \ln \left(\mathcal{F}^{-1} \left\{ \frac{\mathcal{F}\left\{M^2 I(\mathbf{r}_\perp, z = R_2)\right\}/I_{in}}{\frac{\lambda \frac{R_2}{M} \delta}{4\pi\beta} |\mathbf{u}_\perp|^2 + 1} \right\} \right) \tag{3.14}$$

Beltran et al. altered Paganin's method to retrieve the thickness of multi-material samples using a monochromatic source where one material encapsulates the other [15] with the following expression [46]:

$$T_j(r_\perp) = -\frac{1}{\mu_j - \mu_1} \ln \left(\mathcal{F}^{-1} \left\{ \frac{\mathcal{F}\frac{\left\{M^2 I(\mathbf{r}_\perp, z = R_2)\right\}}{I_{in} \exp[-\mu_1 A(r_\perp)]}}{4\pi^2 \frac{R_2}{M} (\delta_j - \delta_1) |\mathbf{u}_\perp|^2 + (\mu_j - \mu_1)} \right\} \right), \tag{3.15}$$

where j index represents the encapsulated material's parameters and 1 index represents the outer material's parameters, and $A(r_\perp)$ is the total projected thickness of the object.

Paganin's method has been derived in the presence of a monochromatic source, but can be further extended to a polychromatic source. In the presence of a polychromatic source, there is the effect of temporally imperfect coherence in the beam that can cause blurring in the image. There are some polychromatic phase retrieval methods that exist that only use the effective wavelength from the spectrum distribution to calculate the energy dependent parameters. The problem with this is that some of these parameters, such as δ and β, have different dependencies on energy, as described in section 2.5.4. Taking this into account, effective values for each parameter are calculated using the spectrum distribution [12].

To extend Paganin's method from a monochromatic source to a polychromatic source, this can be accomplished by integrating the monochromatic TIE as follows [12]:

$$I_{poly}(\mathbf{r}_\perp, z = R_2) = \int_\lambda I_\lambda^{in} D(\lambda) e^{-\mu_\lambda T(\mathbf{r}_\perp)} \left(\frac{R_2 \delta_\lambda}{\mu_\lambda} \nabla_\perp^2 + 1 \right) d\lambda \tag{3.16}$$

where $D(\lambda)$ is the X-ray and detector response and includes the detector's quantum efficiency and the X-ray spectrum. The polychromatic incident intensity can be calculated using:

$$I^{in}_{poly}(\mathbf{r}_\perp) = \int_\lambda I^{in}_\lambda(\mathbf{r}_\perp) D(\lambda) d\lambda. \tag{3.17}$$

The effective absorption coefficient and effective phase coefficient are calculated as follows [12]:

$$\mu_{poly} = \frac{\int_\lambda \mu_\lambda I^{in}_\lambda(\mathbf{r}_\perp) D(\lambda) d\lambda}{\int_\lambda I^{in}_\lambda(\mathbf{r}_\perp) D(\lambda) d\lambda} \tag{3.18}$$

$$\delta_{poly} = \frac{\int_\lambda \delta_\lambda I^{in}_\lambda(\mathbf{r}_\perp) D(\lambda) d\lambda}{\int_\lambda I^{in}_\lambda(\mathbf{r}_\perp) D(\lambda) d\lambda}. \tag{3.19}$$

Using Eq. 3.18 and Eq. 3.19, the intensity integral turns into the following expression:

$$I_{poly}(\mathbf{r}_\perp, z = R_2) = I^{in}_{poly} \exp\left[-\mu_{poly} T(\mathbf{r}_\perp)\right] \left(\frac{R_2 \delta_{poly}}{\mu_{poly}} \nabla^2_\perp + 1 \right) \tag{3.20}$$

From this, Paganin's method becomes the following for the polychromatic case:

$$T(\mathbf{r}_\perp) = -\frac{1}{\mu_{poly}} \ln \left(\mathcal{F}^{-1} \left\{ \mu_{poly} \frac{\mathcal{F}\left\{ M^2 I_{poly}(\mathbf{r}_\perp, z = R_2) \right\} / I^{in}_{poly}}{4\pi^2 \frac{R_2}{M} \delta_{poly} |\mathbf{u}_\perp|^2 + \mu_{poly}} \right\} \right) \tag{3.21}$$

There are only a few differences between Paganin's monochromatic method and Paganin's polychromatic method. The major differences are that it requires a polychromatic intensity and incident intensity, where every pixel is the sum of all energies from the spectrum, and the effective absorption and phase coefficients must be used. Overall, this method is a weighted average of all the X-ray spectrum energies and is valid for thin homogeneous materials.

To this date, there are very few papers that have used Paganin's method that gave quantitative results in the presence of a polychromatic spectrum. There are some groups that claim that it can be further extended to thin homogeneous objects in the presence of a polychromatic source, but no proof of the results. A paper published in 2015 by J Wenz et al. performed a quantitative phase-contrast CT image of a fly and was able to retrieve the thickness of the fly fairly accurately by using the effective phase and linear attenuation coefficient [47]. To the best of my knowledge, there are very few papers that have demonstrated this. In this thesis, Paganin's method will be used to demonstrate that

it can retrieve accurate thicknesses using different types of materials and thicknesses in the presence of a polychromatic source. Specifics on where error can arise in the quantitative results will be introduced for this method and the need for a well-characterized experimental system will be outlined.

3.4 Arhatari TIE Method

In 2008, Arhatari et al. derived a phase retrieval method from the TIE that gave a different result than that derived by Paganin [12]. Under the assumption that the homogeneous object has uniform absorption, the TIE for a monochromatic wave with a wavelength of λ can be expressed as:

$$I_\lambda = I_\lambda^{in}(\mathbf{r}_\perp)\exp\big(-\mu_\lambda T(\mathbf{r}_\perp)\big)\big[1+z\delta_\lambda\nabla^2 T(\mathbf{r}_\perp)\big] \tag{3.22}$$

where $T(\mathbf{r}_\perp)$ is the projected thickness and z is the effective propagation distance, defined by R_2/M. First order Taylor series expansion can be applied to Eq. 3.22 in the weak absorption object limit to obtain:

$$I_\lambda(\mathbf{r}_\perp) = I_\lambda^{in}(\mathbf{r}_\perp)[1-\mu_\lambda T(\mathbf{r}_\perp)+z\delta_\lambda\nabla^2 T(\mathbf{r}_\perp)]. \tag{3.23}$$

Replacing the monochromatic X-ray source with the polychromatic X-ray source, the detector response function and X-ray interactions outside of the sample must be taken into account for each wavelength, which is accomplished through integration:

$$I_{poly}(\mathbf{r}_\perp) = \int_\lambda I_\lambda^{in}(\mathbf{r}_\perp)D(\lambda)[1-\mu_\lambda T(\mathbf{r}_\perp)+z\delta_\lambda\nabla^2 T(\mathbf{r}_\perp)]d\lambda \tag{3.24}$$

Eq. 3.17 is used to simplify Eq. 3.24 further, and using the identity of a Laplacian in the Fourier domain $\mathcal{F}[\nabla^2 T(\mathbf{r}_\perp)] = -\mathbf{u}_\perp^2\mathcal{F}[T(\mathbf{r}_\perp)]$, Arhatari TIE method can be derived:

$$T(\mathbf{r}_\perp) = -\mathcal{F}^{-1}\left(\frac{1}{\mu_{poly}+4\pi^2 z\delta_{poly}u_\perp^2}\mathcal{F}\left[\frac{I_{poly}(\mathbf{r}_\perp)}{I_{poly}^{in}}-1\right]\right). \tag{3.25}$$

One major difference between Arhatari's derivation compared to Paganin's derivation is that Arhatari uses first order expansion to define the exponential, whereas Paganin keeps the exponential in his final expression.

3.5 Bronnikov Method

Bronnikov was the first to derive a single-distance phase retrieval algorithm for propagation-based PCI in 1999. He derived the method to be used in CT reconstruction [19]. In his derivation, he uses the weak defocusing formula that is similar to the TIE and has been previously applied in electron microscopy. This method is derived assuming large Fresnel number, which is defined by:

$$N_F = \frac{a^2}{\lambda z} >> 1, \tag{3.26}$$

where a is the smallest feature size and z is the propagation distance. This weak defocusing formula is derived from the Fresnel diffraction integral, and under the assumption of large Fresnel number and the absorption being zero, it resembles the TIE [15]:

$$I_\lambda(\mathbf{r}_\perp) = I_\lambda^{in}\left(1 - \frac{\lambda z}{2\pi}\nabla^2\phi(\mathbf{r}_\perp)\right). \tag{3.27}$$

Applying Fourier methods to Eq. 3.27, the following phase retrieval formula is achieved:

$$\phi(\mathbf{r}_\perp) = \mathcal{F}^{-1}\left(\frac{\mathcal{F}\left\{\frac{I_\lambda}{I_\lambda^{in}} - 1\right\}}{2\pi\lambda z|\mathbf{u}_\perp|^2}\right) \tag{3.28}$$

Setting the LHS of Eq. 3.28 to the RHS of Eq. 2.3, the following equation can be derived for the projected thickness:

$$T(\mathbf{r}_\perp) = -\frac{\lambda}{2\pi\delta}\mathcal{F}^{-1}\left(\frac{\mathcal{F}\left\{\frac{I_\lambda}{I_\lambda^{in}} - 1\right\}}{2\pi\lambda z|\mathbf{u}_\perp|^2}\right) \tag{3.29}$$

In order to make Eq. 3.29 valid for a polychromatic X-ray source, Eq. 3.19 is used to calculate the effective phase coefficient and the effective wavelength is calculated as follows:

$$\lambda_{poly} = \frac{\int_\lambda \lambda D(\lambda) d\lambda}{\int_\lambda D(\lambda) d\lambda}. \tag{3.30}$$

The projected thickness can be calculated using Bronnikov's method when illuminated with a polychromatic X-ray source using the resulting equation:

$$T(\mathbf{r}_\perp) = -\frac{\lambda_{poly}}{2\pi\delta_{poly}}\mathcal{F}^{-1}\left(\frac{\mathcal{F}\left\{\frac{I_{poly}}{I_{poly}^{in}} - 1\right\}}{2\pi\lambda_{poly} z|\mathbf{u}_\perp|^2}\right). \tag{3.31}$$

3.6 Modified Bronnikov Method

The Modified Bronnikov method was developed by A. Groso et al. in 2006 and is similar to the algorithm that A. Bronnikov developed [23], but includes a filter factor to reduce residual absorption artifacts from the object. To develop this algorithm, it starts with the TIE with the assumption of weak absorption:

$$I_\lambda(\mathbf{r}_\perp) = I_\lambda^{in}\left(1 - \frac{\lambda z}{2\pi}\nabla^2\phi(\mathbf{r}_\perp)\right), \tag{3.32}$$

which is the same result as the starting point for Bronnikov's derivation. Therefore, the phase and projected thickness formula resulting from this equation are the same as Eq. 3.28 and 3.29, respectively. This equation, as metioned in section 3.5, is derived under the assumption of no absorption and large Fresnel number (refer to Eq. 3.26). A. Groso et al. improved Bronnikov's method to allow the absorption requirement to be relaxed by taking into consideration a Fourier low-pass filter:

$$q(\xi,\eta) = \frac{|\xi|}{\xi^2+\eta^2} \tag{3.33}$$

and adding an absorption-dependent correction factor α in the denominator that is found using a semi-empirical approach:

$$q(\xi,\eta) = \frac{|\xi|}{\xi^2+\eta^2+\alpha}. \tag{3.34}$$

This can be extended to Bronnikov's method to create the Modified Bronnikov method:

$$T(\mathbf{r}_\perp) = -\frac{\lambda}{2\pi\delta}\mathcal{F}^{-1}\left(\frac{\mathcal{F}\left\{\frac{I_\lambda}{I_\lambda^{in}} - 1\right\}}{2\pi\lambda z|\mathbf{u}_\perp|^2 + \alpha}\right) \tag{3.35}$$

.

The Modified Bronnikov method can be extended to be used in the case of an object being illuminated with a polychromatic X-ray source like the Bronnikov method by utilizing Eq. 3.30 and a slightly modified version of Eq. 3.31:

$$T(\mathbf{r}_\perp) = -\frac{\lambda_{poly}}{2\pi\delta_{poly}}\mathcal{F}^{-1}\left(\frac{\mathcal{F}\left\{\frac{I_{poly}}{I_{poly}^{in}} - 1\right\}}{2\pi\lambda_{poly} z|\mathbf{u}_\perp|^2 + \alpha}\right). \tag{3.36}$$

.

The constant α is usually decided by trial and error through simulation, although Burvall et al. determined the following expression gives reasonable results [15]:

$$\alpha = \frac{\lambda\mu}{2\pi\delta} \tag{3.37}$$

Using Eq. 3.37 in Eq. 3.36 gives the same resulting filter function as that derived by [12] described in section 3.4.

3.7 Arhatari CTF Method

In 2011, Arhatari et al. developed another phase retrieval method that is an extension of previously proposed CTF-based methods [13]. Their method extends the validity of the CTF to the intermediate Fresnel region for homogeneous objects. As described in section 3.2, it requires a slowly varying phase and an object that is weak absorbing. Their final expression takes into account a polychromatic X-ray source and they claim that they are able to retrieve quantitative projected thickness values of a thin homogeneous sample.

This method is derived using the equations described in 3.2. It starts with the wavefield as described by Eq. 3.6 and propagates the wavefield using Eq. 3.7. The propagated wavefield is linearized assuming a Born-type approximation. After linearization, the intensity can be written in terms of the CTF for monochromatic x-rays and projected thickness $T(\mathbf{r}_\perp)$:

$$\mathcal{F}\big(I_\lambda(\mathbf{r}_\perp, z) - I_\lambda^{in}\big) = I_\lambda^{in} CTF_\lambda(\mathbf{u}_\perp, z)\mathcal{F}\big(T(\mathbf{r}_\perp)\big), \tag{3.38}$$

where $CTF_\lambda(\mathbf{u}_\perp, z)$ is defined defined as:

$$CTF_\lambda(\mathbf{u}_\perp, z) = 4\pi\frac{\sqrt{\delta^2+\beta^2}}{\lambda}\sin\left(\pi\lambda z\mathbf{u}_\perp^2 - \arctan\left(\frac{\beta}{\delta}\right)\right). \tag{3.39}$$

The polychromatic intensity after the sample is defined by:

$$I_{poly}(\mathbf{r}_\perp, z) = \int_\lambda I_\lambda(\mathbf{r}_\perp, z)D(\lambda)d\lambda \tag{3.40}$$

and the incident polychromatic intensity is defined by Eq. 3.17.

Using Eq. 3.17 and Eq. 3.40, Eq. 3.38 can be re-written to take into account the polychromatic source:

$$\mathcal{F}\bigg(\int I_\lambda(\mathbf{r}_\perp,z)D(\lambda)d\lambda-\int I_\lambda^{in}D(\lambda)d\lambda\bigg)=\bigg(\int I_\lambda^{in}D(\lambda)d\lambda\bigg)CTF_\lambda(u_\perp,z)\mathcal{F}\big(T(\mathbf{r}_\perp)\big). \tag{3.41}$$

The CTF in the polychromatic X-ray source case is defined by:

$$CTF_{poly}(\mathbf{u}_\perp,z)=\frac{\int_\lambda D(\lambda,z)CTF_\lambda(\mathbf{u}_\perp,z)d\lambda}{\int_\lambda D(\lambda,z)d\lambda}. \tag{3.42}$$

Eq. 3.41 can be re-written using Eqs. 3.17, 3.40 and 3.42 as follows:

$$\mathcal{F}\bigg(I_{poly}\big(\mathbf{r}_\perp,z\big)-I_{poly}^{in}\bigg)=\mathcal{F}\big(T(\mathbf{r}_\perp)\big)I_{poly}^{in}CTF_{poly}(\mathbf{u}_\perp,z). \tag{3.43}$$

.

Rearranging Eq. 3.43, the projected thickness $T(\mathbf{r}_\perp)$ can be calculated from a phase-contrast X-ray image:

$$T(\mathbf{r}_\perp)=\mathcal{F}^{-1}\left[\frac{1}{CTF_{poly}(\mathbf{u}_\perp,z)}\mathcal{F}\left\{\frac{I_{poly}(\mathbf{r}_\perp,z)}{I_{poly}^{in}}-1\right\}\right]. \tag{3.44}$$

Eq. 3.44 is the Arhatari CTF method used to retrieve the projected thickness of a thin homogeneous sample using the FFT.

3.8 Phase-Attenuation Duality Method

Phase attenuation duality (PAD) occurs when the X-ray energy is greater than 60 keV because Compton scattering is the dominant interaction to attenuation μ at these energies and for light materials ($Z < 10$, where Z is the atomic number); whereas wen the X-ray energy is less than 60 keV, the photoelectric effect is the dominant mechanism of X-ray scattering. Wu et al. used this concept to develop a single image phase retrieval method that is called the PAD method, which is only valid for energies greater than 60 keV. In this method, the amplitude of the attenuation image, $A(\mathbf{r}_\perp)$ can be related to the electron

density $\rho_e(\mathbf{r}, \mathbf{z})$ because the only major scattering mechanism to the attenuation coefficient is Compton scattering [48]:

$$A(\mathbf{r}_\perp) \approx \exp\left[-\frac{\sigma_{KN}}{2} \int \rho_e(\mathbf{r}_\perp, \mathbf{z}) dz \right] = \exp\left[-\frac{\sigma_{KN}}{2} \rho_{e,p}(\mathbf{r}_\perp) \right], \tag{3.45}$$

where the integral is defined over the ray path and results in the projected electron density $\rho_{e,p}(\mathbf{r}_\perp)$. The Klein-Nishina coefficient, σ_{KN}, is defined by Eq. 2.5. At energies above 60 keV, attenuation becomes very small and is almost negligible.

The phase shift can be calculated by relating it to the electron density using Eq. 2.2 found in Section 2.2. Both the attenuation image $A^2(\mathbf{r}_\perp)$ and the phase image $\phi(\mathbf{r}_\perp)$ are related to the projected electron density when energies greater than 60 keV are considered. This leads to the phase and attenuation being both proportional to the electron density, and, therefore, to each other. This relationship is called phase-attenuation duality, which is rooted in a quantum-mechanical relationship between the atomic form factor and the atomic incoherent scattering function. This method is derived from the Wigner distribution, which was originally developed for quantum mechanics, based on the parabolic wave equation [26, 48, 20]. Assumptions made in the derivation of this method is a slowly varying phase through the object and a large Fresnel number (refer to Eq. 3.26) [20]. Using these assumptions, the Wigner distribution becomes a generalized TIE:

$$I(\mathbf{r}_\perp) = I_\lambda^{in}\left(A_0^2\big(\frac{\mathbf{r}_\perp}{M}\big) - \frac{\lambda_2}{2\pi M} \nabla \cdot \left(A_0^2 \nabla \phi\big(\frac{\mathbf{r}_\perp}{M}\big) \right) \right), \tag{3.46}$$

where A_0 is the attenuation amplitude [26].

Using Eq. 3.46, Wu et al. derived a phase-retrieval formula to find the projected electron density $\rho_{e,p}$ of a material based on a single phase-contrast image that is acquired using a monochromatic point source with an energy greater than 60 keV [20, 48]:

$$\rho_{e,p}(\mathbf{r}_\perp) = -\frac{1}{\sigma_{KN}} \ln\left(\mathcal{F}^{-1}\left\{ \frac{\mathcal{F}(M^2 I_\lambda(\mathbf{r}_\perp))/I_\lambda^{in}}{1 + 2\pi\big(\frac{\lambda^2 r_e R_2}{M\sigma_{KN}}\big)\mathbf{u}_\perp^2} \right\} \right). \tag{3.47}$$

This can be further related to phase $\phi(\mathbf{r}_\perp)$:

$$\phi(\mathbf{r}_\perp) = \frac{\lambda r_e}{\sigma_{KN}} \ln\left(\mathcal{F}^{-1}\left\{ \frac{\mathcal{F}(M^2 I_\lambda(\mathbf{r}_\perp))/I_\lambda^{in}}{1 + 2\pi\big(\frac{\lambda^2 r_e R_2}{M\sigma_{KN}}\big)\mathbf{u}_\perp^2} \right\} \right), \tag{3.48}$$

and can be related to projected thickness if the object is homogeneous:

$$T(\mathbf{r}_\perp) = \frac{\lambda^2 r_e}{2\pi\delta\sigma_{KN}} \ln\left(\mathcal{F}^{-1}\left\{ \frac{\mathcal{F}(M^2 I_\lambda(\mathbf{r}_\perp))/I_\lambda^{in}}{1 + 2\pi\big(\frac{\lambda^2 r_e R_2}{M\sigma_{KN}}\big)\mathbf{u}_\perp^2} \right\} \right). \tag{3.49}$$

Eqs. 3.48 and 3.49 can be altered to be used in the presence of a polychromatic source using an effective wavelength that is calculated using Eq. 3.30, leading to the final PAD method equations:

$$\phi(\mathbf{r}_\perp) = \frac{\lambda_{poly} r_e}{\sigma_{KN}} \ln\left(\mathcal{F}^{-1}\left\{\frac{\mathcal{F}(M^2 I_{poly}(M\mathbf{r}_\perp))/I^{in}_{poly}}{1 + 2\pi\left(\frac{\lambda^2_{poly} r_e R_2}{M\sigma_{KN}}\right)\mathbf{u}^2_\perp}\right\}\right), \tag{3.50}$$

and

$$T(\mathbf{r}_\perp) = \frac{\lambda^2_{poly} r_e}{2\pi\delta\sigma_{KN}} \ln\left(\mathcal{F}^{-1}\left\{\frac{\mathcal{F}(M^2 I_{poly}(\mathbf{r}_\perp))/I^{in}_{poly}}{1 + 2\pi\left(\frac{\lambda^2_{poly} r_e R_2}{M\sigma_{KN}}\right)\mathbf{u}^2_\perp}\right\}\right). \tag{3.51}$$

3.9 Attenuation-Partition Based Algorithm

As mentioned in 3.8, PAD occurs when the X-ray energy is greater than 60 keV, making this method only valid for energies greater than 60 keV. In 2008, Yan et al. derived an attenuation-partition based algorithm (APBA) that is iterative. This method uses the same concepts and assumptions used to derive the PAD method, but can be used for energies less than 60 keV. This method requires two images to be acquired: an attenuation image and a phase-contrast image. The two images are acquired at the same X-ray energies and by varying the ODD, R_2. The attenuation image is acquired at $R_2 = 0$ and the phase-contrast is acquired at $R_2 > 0$. Like the single distance method (Eqs. 3.47, 3.48 and 3.49), this method first assumes that the Compton scattering is the main scattering mechanism for both the phase and attenuation image. With this assumption, a guess for the absorption that occurs in the image is calculated [21].

The total X-ray attenuation amplitude image A_0 can be broken down into the X-ray wave amplitude attenuated by incoherent scattering A_{incoh} (determined by the electron density), the X-ray amplitude attenuated by coherent scattering, and the photoelectric effect $A_{pe,coh}$ [21]:

$$A_0(\mathbf{r}_\perp) = A_{incoh}(\mathbf{r}_\perp) \cdot A_{pe,coh}(\mathbf{r}_\perp) \tag{3.52}$$

The X-ray wave amplitude attenuated by Compton scattering A_{KN} is related to an object's phase shift ϕ by [21]:

$$A^2_{KN}(\mathbf{r}_\perp) = \exp\left(-\int \mu_{KN}(\mathbf{r}_\perp, z)dz\right) = \exp\left[\frac{\sigma_{KN}}{\lambda r_e}\phi(\mathbf{r}_\perp)\right]. \tag{3.53}$$

Using the TIE, the following equation can be derived when PAD holds:

$$A_{KN}^2(\mathbf{r}_\perp) = \mathcal{F}^{-1}\left(\frac{\mathcal{F}\left(\frac{M^2}{I_{in}}I\right)}{1+4\pi^2\tilde{k}\mathbf{u}_\perp^2}\right) \tag{3.54}$$

where $\tilde{k}$ can be calculated using the following expression:

$$\tilde{k} = \frac{\lambda^2 R_2 r_e}{2\pi M \sigma_{KN}}. \tag{3.55}$$

The phase can be calculated as follows:

$$\phi(\mathbf{r}_\perp) = \left(\frac{\lambda r_e}{\sigma_{KN}}\right)\ln(A_{KN}^2(\mathbf{r}_\perp)). \tag{3.56}$$

Yan et al. came up with an iterative approach in order to take advantage of the relationship between the phase and attenuation. In order to approximate the phase, it is first assumed that the phase image contains only Compton scattering information. This means that $I_{KN} \approx I$, where I_{KN} is the phase-contrast image where Compton scattering is dominant and I is the original acquired phase-contrast image. The X-ray wave amplitude attenuated by Compton scattering is calculated replacing $\frac{M^2}{I_{in}}I$ with I_{KN}. After, an error term for attenuation $\delta A(\mathbf{r}_\perp)$ is calculated by using the following equations:

$$\delta A(\mathbf{r}_\perp) = \tilde{A}(\mathbf{r}_\perp) - A_0(\mathbf{r}_\perp) \tag{3.57}$$

where

$$\tilde{A}(\mathbf{r}_\perp) = A_{KN}(\mathbf{r}_\perp) = A_{incoh}(\mathbf{r}_\perp). \tag{3.58}$$

$$\delta A(\mathbf{r}_\perp) = A_{KN}(\mathbf{r}_\perp)\cdot(1 - A_{pe,coh}(\mathbf{r}_\perp)) \tag{3.59}$$

Once the error is calculated, the next step is to improve the previous estimate on $\tilde{A}(\mathbf{r}_\perp) = A_{KN}(\mathbf{r}_\perp)$ by incorporating δA. To do this, a hypothetical object is considered that can be modeled by $\delta T_0(\mathbf{r}_\perp)\cdot\exp i\phi(\mathbf{r}_\perp)$ and compute the transmitted X-ray wave field that arrives at the detector at the distance $R_1 + R_2$. This is computed using the paraxial Fresnel diffraction theory for a monochromatic source and can be modeled by the Fresnel-Kirchhoff integral[21]:

$$E(\mathbf{r}_\perp; R_1, R_2) = \frac{\sqrt{I_{in}}}{\lambda R_2} e^{-2\pi i\frac{R_1+R_2}{\lambda}} \int_{\mathbb{R}^2} e^{i\frac{\pi}{k}\left(\frac{\xi_\perp^2}{R_1}+\frac{(\xi_\perp-\mathbf{r}_\perp)^2}{R_2}\right)} A_0(\xi_\perp) e^{i\phi\xi_\perp} d\xi_\perp \tag{3.60}$$

Eq. 3.60 can be simplified to, where $*$ is the convolution operator and $|E_1| = \frac{M}{\sqrt{I_{in}}}\sqrt{I}$:

$$E_1(\mathbf{r}_\perp) = \frac{1}{2\pi\omega}\int_{\mathbb{R}^2} exp\left(i\frac{(\mathbf{r}_\perp - \xi_\perp)}{2\omega}\right)T_0(\xi_\perp)d\xi_\perp = \frac{1}{2\pi\omega}\cdot G(\mathbf{r}_\perp) * T_0(\mathbf{r}_\perp) \tag{3.61}$$

where

$$\omega = \frac{\lambda R_2}{2\pi M} \tag{3.62}$$

and

$$G(\mathbf{r}_\perp) = exp\left[i\frac{\mathbf{r}_\perp^2}{2\omega}\right]. \tag{3.63}$$

Using these equations, δI can be computed as $\delta I = |E_1|^2$. Using this approximation, a the phase-contrast intensity that depends only on Compton scattering is calculated:

$$I_{KN} = \left(\sqrt{I} + \sqrt{\delta I}\right)^2 \tag{3.64}$$

Once the new Compton scattering phase-contrast intensity is calculated, a new iteration step is started. Yan et al. claims that this algorithm can reach an accurate result within 10 iteration step. The algorithm has been summarized below:

Algorithm 1: Attenuation-Partition Based Algorithm

Result: Return $\phi(\mathbf{r}_\perp)$
while $n <= 10$ *or error* $< \epsilon$ **do**
1. Compute I_{KN} using Eq. 3.64
2. Calculate A_{KN}^2 using Eq. 3.54
3. Compute the phase using Eq. 3.56.
4. $A_{KN} = \sqrt{A_{KN}^2}$
5. Calculate δA using Eq. 3.57 and $\tilde{A} = A_{KN}$
6. Calculate the error: error $= |\delta A_{old} - \delta A|$
7. Calculate $T = \delta A \exp(i\phi)$
8. Calculate the analytic transform of Eq. 3.63: $g = \exp(-\frac{i}{2}\omega\mathbf{u}_\perp)/(-i/\omega)$
9. Compute the following: $E_1 = \mathcal{F}^{-1}(\frac{1}{2\pi\omega}g\mathcal{F}(T))$
10. Compute $\delta I = |E_1|^2$
11. Assign $\delta A_{old} = \delta A$
12. Assign $n = n + 1$

end

In 2010, Yan et al. published a paper on the performance of the attenuation-partition based iterative phase retrieval algorithm and suggested that this method can retrieve the

phase of a polychromatic image. To this date, no one has published a paper proving that this method works or does not work in the polychromatic case. They explain that there are two modifications that need to be made to the algorithm in order for it to work in the polychromatic case. In the polychromatic case, the wavelength must be replaced by the spectral average $\langle\lambda^2\rangle/\langle\lambda\rangle$ and used to calculate σ_{KN} and ω. The parameter $\tilde{k}$ is calculated as follows in the case of a polychromatic spectrum [49]:

$$\langle\tilde{k}\rangle = \frac{r_e R_2}{2\pi M} \cdot \left\langle \frac{\lambda^2}{\sigma_{KN}} \right\rangle \tag{3.65}$$

3.10 Summary of Phase Retrieval Methods

A summary of the assumptions made in the derivation of phase retrieval methods is presented in Table 3.1.

Table 3.1: Summary of assumptions made in the derivations of phase retrieval methods

Method (Eq. Number)	Assumptions
Bronnikov (Eq. 3.31)	- $\mu \approx 0$ - Fresnel approximation - $N_F >> 1$ - Weak defocusing formula - Inhomogeneous or homogeneous samples
Modified Bronnikov (Eq. 3.36)	- Weak absorption - Fresnel approximation - $N_F >> 1$ - TIE - Inhomogeneous or homogeneous samples
Paganin (Eq. 3.21)	- $\mu \propto \delta$ - Fresnel approximation - $N_F >> 1$ - TIE - Homogeneous object
Arhatari TIE (Eq. 3.25)	- Weak absorption - Fresnel approximation - $N_F >> 1$

	- TIE - Homogeneous object - $\frac{\partial \mu}{\partial \mathbf{r}_\perp} \approx 0$
Arhatari CTF (Eq. 3.44)	- Weak absorption - Slowly varying phase - Intermediate Fresnel region - CTF - Homogeneous object
PAD (Eq. 3.51)	- $\mu \propto \delta$ - Fresnel approximation - $N_F >> 1$ - Slowly varying phase - TIE - X-ray energy = 60 keV - 500 keV - Assumption: Compton scattering is the dominant scattering phenomena - Inhomogeneous or homogeneous samples
APBA (Algorithm 1)	- $\mu \propto \delta$ - Fresnel approximation - $N_F >> 1$ - Slowly varying phase - TIE - X-ray energy < 60 keV - Requires attenuation image and phase-contrast image - Iterative method (10 iterations)

Chapter 4

Numerical Modeling

Numerical modeling is an important step to understanding an imaging system and its capabilities. It is helpful in determining what parts of the system play the biggest roles and the most crucial parameters to characterize. It determines where errors can arise and what parts of the system need improving. The simulation tool defines which objects are possible to image using a desired technique and how it should be done. The limitation of simulations is simulating complex or unknown objects because these objects require accurate parametrization and results.

This chapter covers the simulation of the objects and free-space propagation of X-rays to create a propagation-based phase-contrast image. All parameters used in the simulation are a representation of an ideal case of the experimental system.

Initially, an ideal case using a monochromatic plane wave X-ray that contains a single energy is described. After, modifications are made to extend the simulation to a polychromatic source at finite distance.

Noise is taken into account at the end of the simulation.

4.1 Object Modeling

The object is modeled assuming that it is fully described by its complex refractive index $n(x, y, z) = 1 - \delta(x, y, z) + i\beta(x, y, z)$. The object is considered homogeneous in a small sampling region and all scattering that is caused by crystal lattice planes or any material inhomogenities, such as cracks, impurities and pores are neglected. The wave propagation

direction that is transverse to the z direction is neglected in the object by considering a thin object.

The incident plane wave is described by the multiplication of transmission function. The transmission function of the object at a specified energy is described by the thickness, t, the linear attenuation coefficient μ, the wavenumber $k = 2\pi/\lambda$, and the phase coefficient δ:

$$T(E) = exp\Big(- t\big(\frac{\mu}{2} + ik\delta\big)\Big). \tag{4.1}$$

The thickness of the object is defined by the geometrical shape that is simulated, such as the equation of a cylinder, sphere or box, and is calculated analytically for each point. The linear attenuation coefficient is defined by values defined by the NIST and the phase coefficient is calculated using the Eq. 2.7.

4.2 X-ray Propagation

The Fourier filter that corresponds to free space propagation is as follows:

$$H(E) = \exp\Big(- i\pi z\lambda\big(u^2 + v^2\big)\Big), \tag{4.2}$$

where u and v are the spatial frequencies in the x and y direction, respectively. $z = R_2/M$ is the effective propagation distance, where R_2 is the ODD and $M = \frac{R_1+R_2}{R_1}$ is the magnification.

Using this Fourier filter, the X-ray propagation can be calculated:

$$U = \Big|\mathcal{F}^{-1}\Big\{\mathcal{F}\big(T(E)\big) \cdot H(E)\Big\}\Big|^2. \tag{4.3}$$

4.3 Detector Response

The response of the detector is taken into consideration. One important component of the detector that needs to be taken into account is the quantum efficiency of the detector, as defined by Eq. 2.13. In order to calculate the quantum efficiency, the linear attenuation coefficient and the thickness of the detector must be known. The spectrum produced

by the X-ray source is multiplied by this factor to give the detector response for each corresponding energy.

One photon that hits the detector might cause the detector's output signal to be spread over several pixels, which causes blurring to the image and limits the resolution. The blurring caused by the detector is defined by the point spread function (PSF). The convolution of the PSF is known as the modulation transfer function (MTF), which is a more common factor used to describe the resolution of the detector. The MTF of each pixel can be described analytically using the following function, which is described in the Fourier domain as:

$$MTF_{pixel} = sinc(\pi dx_p u) \cdot sinc(\pi dy_p v), \tag{4.4}$$

where dx_p is the size of the pixel in the x-direction and dy_p is the size fo the pixel in the y-direction.

The intensity at the detector is calculated by taking into account the blurring effect of the pixels:

$$I = \mathcal{F}^{-1}\bigg(\mathcal{F}\big(|U(x,y)|^2\big) \cdot MTF_{pixel}\bigg). \tag{4.5}$$

4.4 Noise

In previous sections, the final image is produced assuming that the final image is created by averaging an infinite number images. In reality, this is not feasible, therefore this is not enough to predict what will occur experimentally. Noise, which is unwanted signal in an image, plays a large role in X-ray imaging. In the absence of noise, resolution in the sense of MTF can easily be deconvoluted, but in its presence, MTF becomes important factor. There are many sources of noise, but, in an X-ray image, many do not need to be taken into account. The main source of noise in an image is photon noise. Photon noise, also known as shot noise, can be modelled by a Poisson process and is due to the particle nature of light. Increasing the number of detected X-ray photons can reduce photon noise. Another source of noise is caused by the readout electronics and is called readout noise. Readout noise is small compared to photon noise if there is a large number of photons being detected. Dark noise caused by the flow of dark current in a pixel is nearly negligible for short exposure times because the dark current in the CMOS detector used is very small. Another common source of noise is gain noise that is due to variation in signal gain between the pixels, but this can be corrected for by dividing the image by the flat-field image since gain is constant in time. In X-ray imaging, structure noise that is due to overlapping structures of an object can also be an issue, but this is highly object dependent and not detector dependent. In

tomography, this is not a problem since the structure is viewed from many angles and all the structures can be viewed in the reconstructed image. Illumination noise is caused by variations in X-ray illumination and can be compensated for in the same way as gain noise.

Therefore, the two sources of noise that have the most impact on the image are photon noise and readout noise. Readout noise can be modelled as additive zero-mean white noise with a standard deviation. Photon noise depends on X-ray flux and spectrum. The number of photons reaching a detector pixel is hard to predict since it is inherently random, although the expectation value N can be calculated using the following formula:

$$N(x, y) = \Phi t w h \eta_{det} I_b \tag{4.6}$$

where Φ is the photon flux in the detector plane with no object present, t is the exposure time, w and h are the pixel width and height, η_{det} is the detector absorption efficiency and I_b is the blurred intensity image. The actual expectation value N' follows a Poisson probability distribution. Thus, the actual signal S' detected is random and can be calculated as follows:

$$S'(x, y) = g \int E N'(x, y, E) dE \tag{4.7}$$

where g is the gain and E is the energy. S' will be normally distributed since N' is. Variances add linearly for normal distributions, therefore:

$$\sigma(x, y)^2 = Var(S'(x, y)) = g^2 \int E^2 N(x, y, E) dE. \tag{4.8}$$

Scaling using a random number generator that gives values from a standard normal distribution X, an instance of noise can be added to the simulated image:

$$S'(x, y) = S(x, y) + \sigma(x, y) X. \tag{4.9}$$

Eq. 4.9 makes the assumption that the X-ray photon deposits all of its energy in a single pixel. The photon can deposit some of its energy in surrounding pixels, which creates a correlation of noise in surrounding pixels that is more easily taken into account in the Fourier domain. The noise power spectrum (NPS) describes this correlation assuming the noise is shift invariant. The NPS is measured by Fourier transforming and squaring the image acquired without a sample present and gives the quantity of noise that is at each spatial frequency. The normalized frequency-dependent part of NPS ($NPS_n(u, v) = NPS/\sigma^2$) is independent of exposure and the square root of NPS_n is used to filter the noise instance $\sigma(x, y)X$ in Eq. 4.9, which gives rise to the final noise equation:

$$S'(x, y) = S(x, y) + \mathcal{F}^{-1}\big\{\mathcal{F}\big\{\sigma(x, y)X\big\}\sqrt{NPS_n(u, v)}\big\}. \tag{4.10}$$

4.5 Polychromatic X-ray Propagation

The difference between monochromatic and polychromatic X-ray propagation is that the transmission function and the X-ray propagation must be calculated at each energy. The transmission function and the Fourier filter both rely on the X-ray energy, thus an integration can be performed over all wavelengths as follows:

$$U = \int_{\lambda} \left| \mathcal{F}^{-1} \left\{ \mathcal{F}\big(T(E)\big) \cdot H(E) \right\} \right|^2 \cdot D(E) dE. \tag{4.11}$$

$D(E)$ is the detector response to the X-ray energies where the quantum efficiency of the detector is taken into account.

4.6 MATLAB Numerical Implementation

In the previous sections, the functions to describe X-ray propagation are all analytical. The integrals need to be discretized and evaluated numerically. The model is simulated in MATLAB® 2018 using a script. Variations of this code are used to simulate the propagation-based PCI of the object and this image is used to perform phase retrieval throughout the entire thesis.

First, the imaging geometry is defined:

```
R1 = 8/100; % [m] source-to-object distance
R2 = 8/100; % [m] object-to-detector distance
Rtot = R1 + R2; % [m] source-to-detector distance
M = Rtot/R1; % magnification
z = R2/M; % [m] effective propagation distance
```

The imaging geometry is varied to see its effect on the error when phase retrieval is performed.

Next, the simulation resolution, field of view and spatial frequencies are defined. The pixel pitch is chosen to be7.8 µm pixel pitch to represent the high-resolution CMOS detector that is currently in use in the laboratory.

```
% Detector
p =7.8*1e-6; % [m] pixel pitch

% Simulation resolution and field of view
model_res = p/10;
dx = model_res; % [m] simulation pixel size in x direction in object plane
dy = model_res; % [m] simulation pixel size in y direction in object plane
xfov = 3*r;
yfov = 20e-6;
xmin = -xfov/2; xmax = xfov/2; % [m] x range of field of view in
% object plane
ymin = -yfov/2; ymax = yfov/2; % [m] y range of field of view in
% object plane
x = xmin:dx:xmax; y = ymin:dy:ymax; % [m] coordinate vectors
[X,Y] = meshgrid(x,y); % [m] coordinate matrices

% Spatial frequencies
nx = length(x); ny = length(y); % number of pixels in x and y direction
% [1/m] frequency in the x and y direction, respectively
u = ifftshift((-floor(nx/2):floor((nx-1)/2))/(nx*dx));
v = ifftshift((-floor(ny/2):floor((ny-1)/2))/(ny*dy));
[U,V] = meshgrid(u,v); % [1/m] frequency grid
w2 = U.^2 + V.^2; % frequency magnitude squared
```

Furthermore, physical constants that are required to calculate the various equations throughout the code are defined.

```
% Physical constants
c = 299792458; % [m/s] speed of light
h = 6.6260689633e-34; % [Js] Planck's constant
eV = 1.6022e-19; % [J/eV] unit conversion constant
re = 2.82e-15; % [m] classical electron radius
Na = 6.022e23; % [atoms/mol] Avogadro's number
me = 9.10938356e-31; %[kg] mass of an electron
```

The X-ray spectrums used for most of the simulations throughout this thesis are acquired using a MATLAB® toolset developed by Siewerdsen et al. in 2004 called Spektr [50]. This toolset contains many functions for computing beam-quality characteristics,

mass and mass-energy attenuation coefficients. The mass and mass-energy attenuation coefficient data is retrieved from NIST. The spectrum function computes the spectrum, given the tube potential (kVp), and the inherent or total filtration (mm). This function is an adaptation of the TASMIP model developed by Boone and Seibert [51] that computes an X-ray spectra based on the method of interpolating polynomials. The Beer's function filters the spectrum by specified materials and thicknesses according to Beer's law. This function uses attenuation coefficients acquired from NIST.

The X-ray spectrums used throughout this thesis for experimental images are ones that were obtained using cadmium telluride (CdTe) Spectrometer. The spectrum defined in the simulation is a polychromatic spectrum from a Thermo Scientific PXS5-927 MicroFocus X-ray Source with a maximum energy of 60 kV. Both filtered and unfiltered spectrums are attempted at 40 kV and 60 kV. The filtered spectrums are obtained by placing 2mm of aluminum in front of the X-ray source. The problem in obtaining the unfiltered spectrum is that the count rate of the CdTe spectrometer is not high enough and the X-ray source is too powerful to obtain an accurate spectrum. In order to obtain a more accurate spectrum, a 1mm to 2mm piece of tungsten with a pinhole should be placed in front of the CdTe detector of the spectrometer to act as a collimator, therefore only allowing a percentage of the photons through. This tungsten piece had not been obtained by the end of this thesis, but for further studies on the experimental system it is necessary.

The spectrum used in simulation was defined as follows:

```
E = [1:150]*1e3; % Energy [eV]
filter = -0.8; % Filter for half-value layer of 1.2
kVp = 60; % Source potential [kV]
spectrum = spektrSpectrum(kVp,filter); % defining spectrum using Spektr
```

The next step is to define the material parameters. This section is altered for different types of materials. PTFE, polystyrene, Kapton, aluminum, Kevlar and tungsten are the materials that are tested in this thesis. The code below describes the material information of PTFE. The phase coefficient values are calculated using Eq. 2.7. The values for the linear attenuation coefficient are obtained using 'Spektr' or values defined by NIST. The linear attenuation values obtained from Spektr and NIST are interpolated to calculate values corresponding to the energies of the spectrum using MATLAB®'s interpolation function.

```
% PTFE information for phase coefficient:
% Composition: C2F4
```

```
rho = 2.21439238; % density of PTFE [g/cm^3]
Num_of_C = 2; % number of carbon
Num_of_F = 4; % number of fluorine
Num_of_H = 0; % number of hydrogen

% Atomic numbers
ZH = 1; % hydrogen
ZC = 6; % carbon
ZF = 9; % fluorine
Z = ZC*Num_of_C + ZH*Num_of_H+ ZF*Num_of_F; % total atomic number

% Molar Mass
MMC = 12.011*Num_of_C; % [g/mol]
MMH = 1.008*Num_of_H; % [g/mol]
MMF = 18.998*Num_of_F; % [g/mol]
MM_total = MMC + MMH + MMF; % [g/mol] total molar mass

mu = spektrMuRhoCompound([6 2; 9 4])*rho*100; % [1/m] attenuation
% coefficient of PTFE
mu = interp1([1:150], mu, E/1000); % interpolate for all energies
```

Next, the quantum efficiency of a-Se detector is calculated using Eq. 2.13. The X-ray spectrum is multiplied by the quantum efficiency to obtain the energies at which selenium is more responsive.

```
% Quantum efficiency of selenium
rho_Se = 4.819; %[g/cm^3] density of selenium
mu_Se = spektrMuRhoElement(34)*rho_Se*100; % [1/m] attenuation
%coefficient of selenium (Z=34)
mu_Se = interp1([1:150], mu_Se, E/1000);  %interpolate for all energies
thickness_Selenium = 100e-6; % [m] thickness of selenium deposited on
% the detector
eta = 1-exp(-mu_Se.*thickness_Selenium); % quantum efficiency
spectrum_Se = spectrum.*eta; % spectrum seen by detector
```

The next section of the code is dedicated to the X-ray propagating through the object. No noise is taken into account in this section. All energy contributions to the image are summed up and the for-loop iterates through all energies of the spectrum.

```
thickness = 2*real(sqrt(r.^2-X.^2)); % [m] geometrical shape: cylinder
img = zeros(ny,nx); %[detector counts] phase image initialized
img_abs = zeros(ny,nx); %[detector counts] absorption image initialized

for n = 1:length(E)
    %the transmission function of the object at energy E(n)
    transmission = exp(-thickness*(mu(n)/2+1i*k(n)*delta(n)));

    %Absorption Image
    img0 = abs(transmission).^2;

    %Superimpose absorption image data
    img_abs = img_abs + spectrum_Se(n).*img0;

    %Fourier filter corresponding to free space propagation
    propagator = exp(-1i*pi*z*lambda(n)*w2);

    %propagator field for current photon energy
    img0 = abs(ifft2(fft2(transmission).*propagator)).^2;

    %add contribution of this energy to the image
    img = img+img0.*spectrum_Se(n);
end
```

When comparing the phase retrieval algorithms, noise is not taken into consideration and only the perfect case is studied. For later simulations that determine the error in the experimental data, noise is added to observe the effect of detector noise on the chosen phase retrieval algorithm. Noise is calculated using Eq. 4.8. The following line is added to the end of the for-loop that defines the image:

```
% Add contribution to the variance of the noise
noiseVariance = noiseVariance + img0*spectrum_Se(n);
```

Then noise is added to the image after the for-loop as follows:

```
% Specify the detector resolution
dPSFWidth = 25e-6;% [m] FWHM of Gaussian detector point spread function
```

```
%[m] detector PSF standard deviation in sample plane
dPSFSigma = dPSFWidth/(2*sqrt(2*log(2)))/M;

% Add photon noise
NPS = exp(-w2*pi^2*4*dPSFSigma^2) + .05; %normalized noise power spectrum

% Create an instance of white noise with the right noise variance
noiseInstance = randn(ny,nx).*sqrt(noiseVariance);

% Filter the noise to get the correct noise power spectrum
noiseInstance = ifft2(fft2(noiseInstance).*sqrt(NPS));

img = img + noiseInstance; % Add the noise to the image
```

In the next section of the algorithm, the image is blurred by applying the MTF of the pixels, as described in section 4.3 using Eq. 4.4 and Eq. 4.5, which takes into consideration the resolution of the pixels.

```
% Blur the image (filter with the MTF)
img_blur = ifft2(fft2(img).*pixelMTF);
```

All the previous simulation steps assume a smaller pixel pitch in the object plane. The next step is to interpolate the image from the simulated pixels to the detector pixels in the sample plane. The pixel size in the sample plane is calculated by taking into account magnification. Magnification also needs to be taking into account when interpolating the signal to the detector pixels. Interpolation is completed using the built-in MATLAB® 2D interpolation function.

```
% Interpolate from simulation pixels to detector pixels
% Define pixel coordinates
Dx = p/M; Dy = p/M; % [m] pixel size in sample plane
xp = min(x)-dx/2+Dx/2:Dx:max(x)+dx/2-Dx/2; % [m]
yp = min(y)-dy/2+Dy/2:Dy:max(y)+dy/2-Dy/2; % [m]
% [m] create pixel coordinates matrices
[Xp,Yp] = meshgrid(xp,yp);

% Interpolate and scale signal with pixel size
img = interp2(X,Y,img_blur,Xp,Yp)*p/M*p/M/(dx*dy);
```

The codes used for simulations are found in Appendices C and D. The code used for experimental results is described in E.

Chapter 5

Comparison of Phase Retrieval Methods

Every phase retrieval method is derived based on different assumptions, as discussed in Chapter 3, although each method serves the same purpose (i.e. to retrieve the phase, electron density or thickness of an object). Currently, no results have been published comparing all the methods mentioned in Chapter 3 in the polychromatic case to determine which method produces the best quantitative results overall. This chapter will explore the limitations of each method through the simulation of a homogeneous cylinder and sphere using different materials.

5.1 Methodology

The materials used in the analysis are: PTFE, polystyrene and Kapton. The material parameters are outlined in Table 5.1.

Table 5.1: Material properties

Material	Composition	Density [g/cm^3]
Polystyrene	$(C_8H_8)_n$	1.04
PTFE	$(C_4F_4)_n$	2.2
Kapton	$(C_{22}H_{10}N_2O_5)_n$	1.42

The best known PTFE-based formula is Teflon by Chemours, and it is chosen for simulations because this is the plastic that was imaged experimentally and this polymer has a much higher density compared to polystyrene and Kapton. Polystyrene is a versatile plastic that is used in a variety of consumer products such as food-service, automotive, electronics, insulation and medical industries. Kapton is a nearly pure phase object, which is a requirement for some of the phase retrieval methods, therefore it was chosen to see if these methods would perform better on this material.

The numerical model described in section 4.6 is used to simulate the object and X-ray image and the full script can be found in Appendix D for all methods except for APBA. The script for APBA can be found in Appendix C.

The spectrum used for these simulations was obtained using the external code called 'Spektr'. For all simulation cases, except varying source potential, the 90 kV filtered spectrum was used that is seen in Figure 5.1.

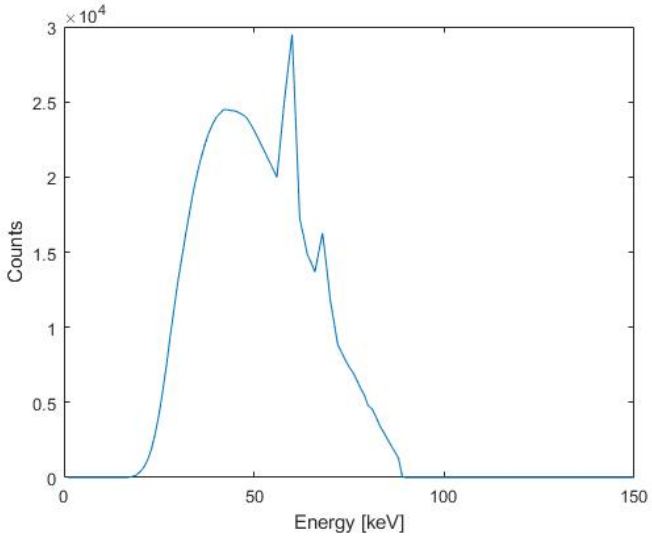

Figure 5.1: 90 kV filtered spectrum simulated using Spektr

In this chapter, seven different phase retrieval methods are compared, which are: Bronnikov method, Modified Bronnikov method, Paganin's method, Arhatari TIE method, Arhatari CTF method, PAD method and APBA. All of these algorithms and how they are derived are described in Chapter 3. These methods are compared by observing the behaviour of the relative error of the thicknesses under five different cases: varying the thickness of the object, varying the source potential, varying the pixel size, varying R_1 and

varying R_2. The relative error is calculated as follows:

$$\text{Relative Error} = \frac{|\text{Actual Thickness} - \text{Retrieved Thickness}|}{\text{Actual Thickness}} \tag{5.1}$$

where the retrieved thickness is the value retrieved with the phase retrieval algorithm and the actual thickness is known thickness of the simulated object.

The parameters for each test, unless they are the specified variables, are outlined below:

- Source potential = 90 kV
- Object thickness = 100 μm
- $R_1 = 8$ cm
- $R_2 = 16$ cm
- Pixel size = 7.8 µm

The first test is varying the thickness from 10 µm to 400 µm. The second test is varying R_1 from 1 cm to 100 cm. The third test is varying R_2 from 1 cm to 100 cm with R_1 set to 16 cm. The reason R_1 is set to 16 cm instead of 8 cm is because when R_1 is set to 8 cm, the retrieved thickness values past $R_2 = 72$ cm are imaginary; whereas setting $R_1 =$ 16 cm prevents the retrieved thicknesses from resulting in imaginary numbers. The results for varying R_2 from 1 cm to 100 cm with R_1 set to 8 cm can be seen in Figures A.5, A.12, A.14, A.21, A.27, A.34, A.36, A.43, A.49, A.56, A.58 and A.65 Appendix A, and show the same trend to what will be described for the case of $R_1 = 16$ cm. The fourth test involves varying the source potential from 20 kV to 140 kV. This test is performed since some methods state they perform better at energies greater than 60 keV when Compton scattering becomes the dominant X-ray interaction. The final test performed is to view how the phase retrieval methods behave with varying pixel size from 10 µm to 100 µm. The pixel size is also varied from 1 µm to 10 µm in Figures A.6, A.13, A.15, A.22, A.28, A.35, A.37, A.44, A.50, A.57, A.59 and A.66 seen in Appendix A, and show similar trends to the case of varying the pixel size from 10 µm to 100 µm. In all these test, the ideal situation is considered where an infinite number of images are average and therefore noise does not have an effect.

The tests are performed on spheres and cylinders. The results for the spheres can be found in sections A.1.1, A.1.2, A.2.1, A.2.2, A.3.1 and A.3.2 in Appendix A. Overall, the

relative errors of the spheres behave similarly to that of the cylinders. Based on these results, the shape of the object should not significantly effect the retrieved thickness.

For these tests, the α-term in the Modified Bronnikov method is set to Eq. 3.37, where λ, μ and δ are all calculated using the weighted averages found in Eqs. 3.18, 3.19 and 3.30. With the α-term equal to Eq. 3.37, the Modified Bronnikov method equation is equivalent to Arhatari TIE method.

5.2 Results

In this section, the simulation results of cylinders will be presented for each material and the best phase retrieval algorithm will be determined. This phase retrieval method will be used in the remainder of this thesis.

5.2.1 Polystyrene

Polystyrene is a low density polymer with properties described in Table 5.1. Polystyrene was chosen as a material due to the fact that it is a cheap plastic used a lot in industry. Figure 5.2 shows the results of all seven phase retrieval methods for relative error versus thickness. As can be seen in Figure 5.2, Bronnikov method has an exponential increase in relative error and, overall, its relative error is extremely high. For this reason, all results for the rest of the tests and the following materials will not include Bronnikov method as it presents high relative error in each case compared to all of the other phase retrieval algorithms. All results for each material that include Bronnikov method are found in sections A.1.1, A.2.1 and A.3.1 in Appendix A.

It can be seen in Figure 5.3 that Paganin's method, Modified Bronnikov method and Arhatari TIE method perform the best across all thickness values for polystyrene. Overall, all the methods seem to produce stable relative error when the thickness is greater than 150 µm.

Figure 5.4 displays the relative error versus SOD for polystyrene. All the methods oscillate while R_1 is increases and seem to increase significantly around 0.7 m. The four methods that appear to perform the best with varying R_1 value for polystyrene are: Modified Bronnikov method, APBA, Arhatari TIE method and Paganin's method. These methods have relative errors that are close to overlapping for all R_1 values.

Comparable to when varying R_1, varying R_2 also causes the relative error to oscillate as can be seen in Figure 5.5. For varying the ODD, the relative error decreases for increasing

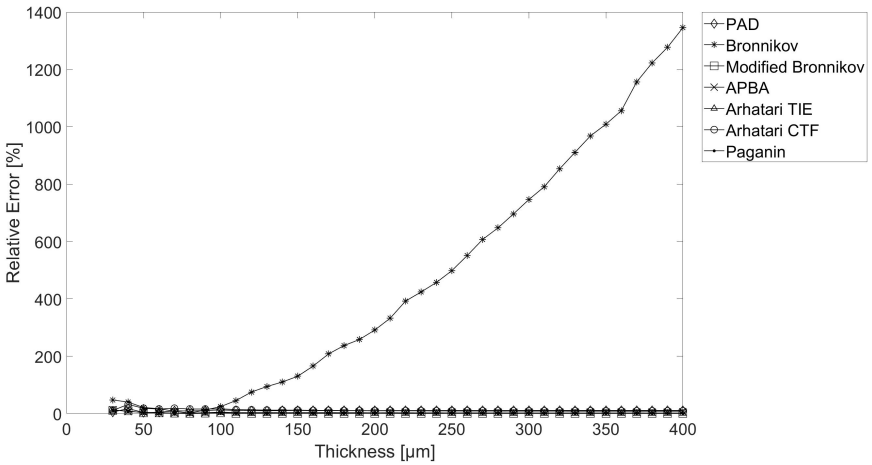

Figure 5.2: Relative error versus thickness for polystyrene retrieved with different phase retrieval methods (including Bronnikov Method)

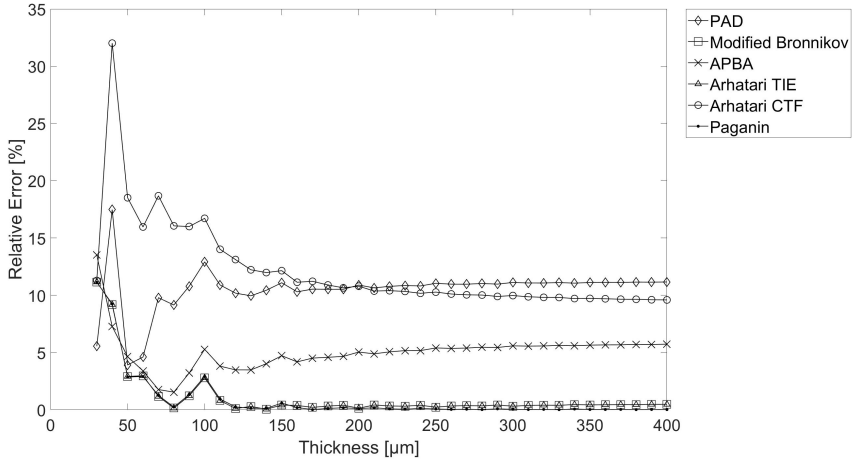

Figure 5.3: Relative error versus thickness for polystyrene retrieved with different phase retrieval methods

R_2 value. The same four phase retrieval methods perform the best in this case as for varying R_1 values, which are: Modified Bronnikov method, APBA, Arhatari TIE method and Paganin's method.

The next test performed was varying the source potential. These results are viewed

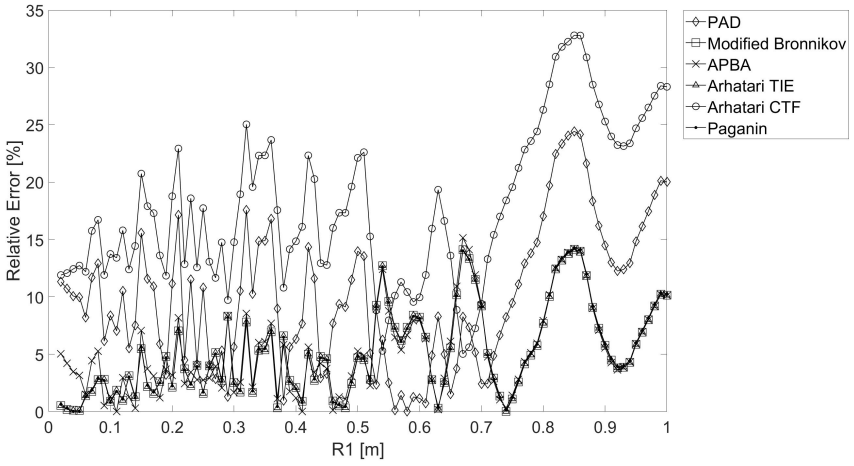

Figure 5.4: Relative error versus R_1 for polystyrene retrieved with different phase retrieval methods

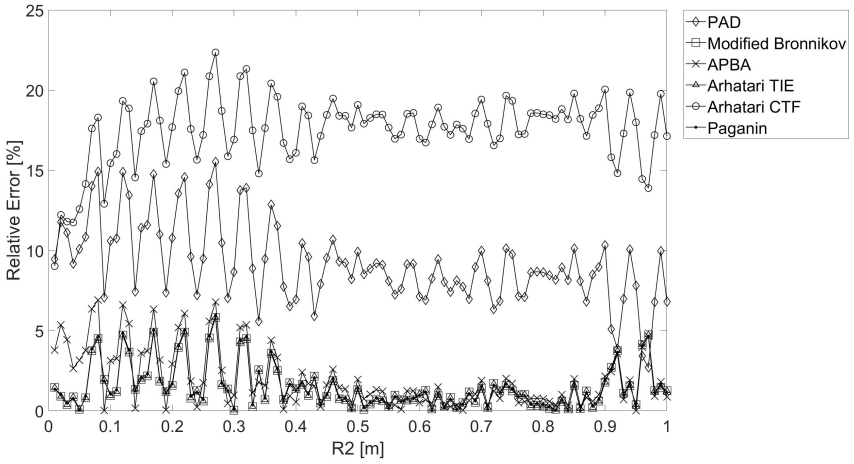

Figure 5.5: Relative error versus R_2 with $R_1 = 16$ cm for polystyrene retrieved with different phase retrieval methods

in Figure 5.6. The relative errors achieved by PAD and APBA decrease with increasing source potential. This is expected for PAD as it is derived assuming Compton scattering is the dominant X-ray interaction, which occurs at X-ray energies greater than 60 keV. When the source potential is set to 60 kV, most X-ray energies are much less than 60

keV. In this energy range, Compton scattering is not the main X-ray interaction and the photoelectric effect dominates. As the source potential is increased past 120 kV, the mean X-ray energies are around 60 keV and Compton scattering dominates. For this reason, PAD performs better at higher source potentials. On the other hand, APBA is derived to work for X-ray energies less than 60 keV, although, according to the results seen in Figure 5.6, this is not the case. APBA behaves similarly to PAD with source potential, therefore the claim that APBA works for lower X-ray energies appears to be incorrect. This will be further investigated in a later section. Arhatari CTF performs best with lower source potentials and the relative error slowly increases with increasing source potentials. Overall, Modified Bronnikov method, Arhatari TIE and Paganin's method perform the best out of all the investigated phase retrieval methods and the relative errors remain relatively stable for all source potentials. At source potentials greater than 100 kV, it appears that APBA performs as well as the other three methods for polystyrene.

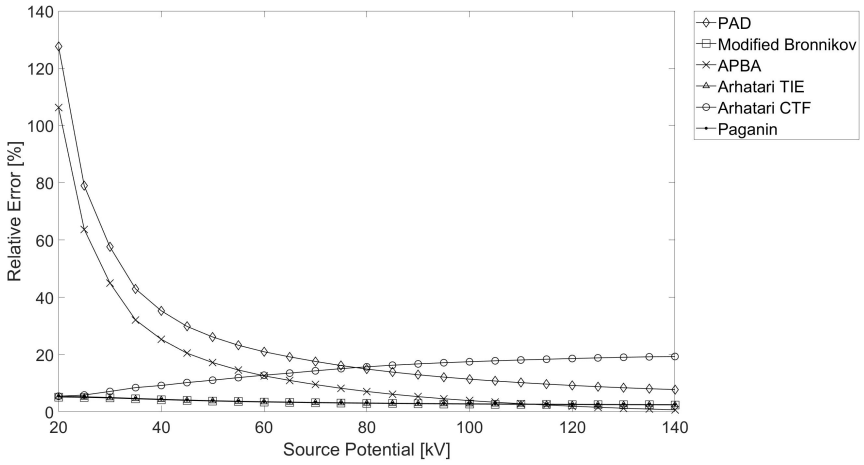

Figure 5.6: Relative error versus source potential for polystyrene retrieved with different phase retrieval methods

Figure 5.7 shows the relative error versus pixel size for polystyrene. For pixel sizes less than 30 µm, Modified Bronnikov method, Arhatari TIE method and Paganin's method perform the best. All the methods have the greatest relative error when the pixel size is between 40 µm and 50 µm. For pixel sizes greater than 60 µm, PAD and Arhatari CTF method perform the best out of the seven methods.

In general, it appears that Modified Bronnikov method, Arhatari TIE method and Paganin's method perform the best for polystyrene in all the test cases.

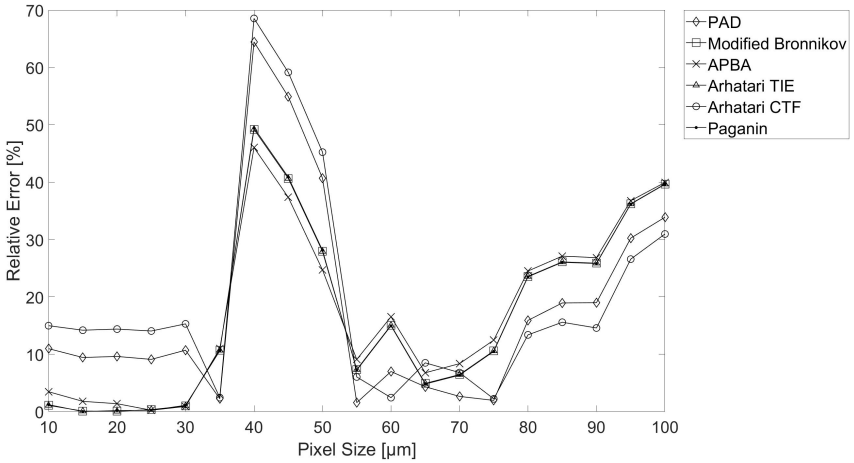

Figure 5.7: Relative error versus pixel size for polystyrene retrieved with different phase retrieval methods

5.2.2 Kapton

Kapton is considered a pure phase object with negligible absorption and was chosen for this reason. The material parameters for Kapton can be found in Table 5.1.

Like for polystyrene, it can be seen in Figure 5.8 that Modified Bronnikov method, Arhatari TIE and Paganin's method perform the best for varying thickness. APBA performs worse for Kapton compared to the results for polystyrene with almost an 10% increase in relative error. Also, PAD experiences a 10% increase in relative error compared to the polystyrene case. Arhatari CTF for Kapton remains roughly the same relative error over all thicknesses compared to polystyrene.

Figure 5.9 shows the relative error versus varying R_1 results for Kapton. The same oscillating behaviour can be seen for Kapton as was seen for polystyrene. Some differences that can be seen for Kapton is that Modified Bronnikov method, Arhatari TIE and Paganin's method perform the best for R_1 values less than 0.5 m, but for values greater than 0.5 m APBA performs the best. Another difference is that PAD and Arhatari CTF method have similar relative error results for Kapton, compared to their results using polystyrene where they have around a 10% difference in relative error. As in the case of polystyrene, Kapton also experiences an increase in relative error at greater R_1 values.

Modified Bronnikov method, Arhatari TIE method and Paganin's method have the lowest relative error for all R_2 values as seen in Figure 5.10. Although APBA performs

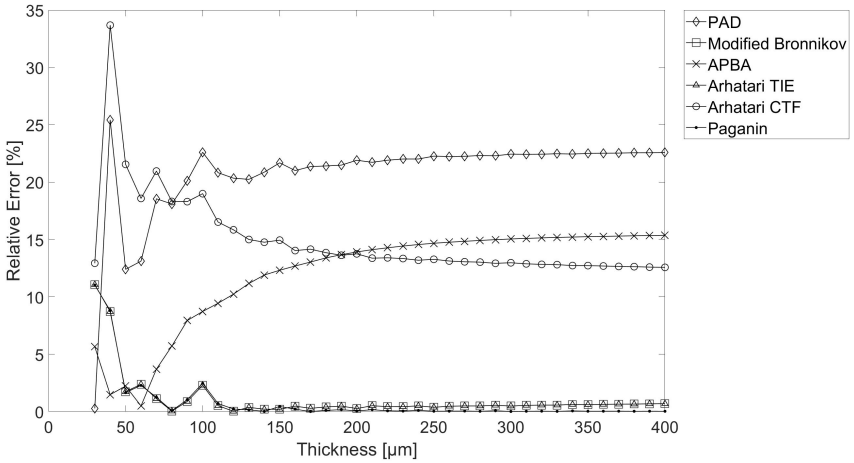

Figure 5.8: Relative error versus thickness for Kapton retrieved with different phase retrieval methods

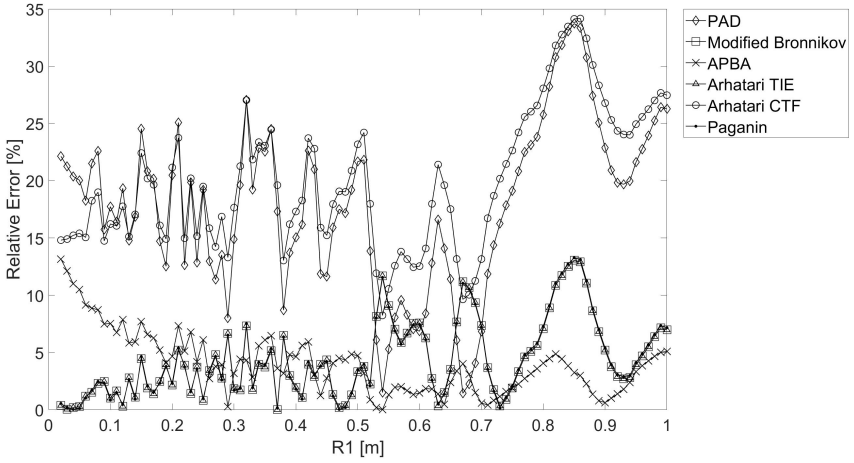

Figure 5.9: Relative error versus R_1 for Kapton retrieved with different phase retrieval methods

just as well as those three methods for polystyrene, that is not the case for Kapton. This shows that the methods can be very material dependent. Also, the relative errors for PAD and Arhatari CTF method's are similar in the case of Kapton, which is not the case for polystyrene. Overall, the oscillating trend observed in Figure 5.10 is similar to that seen

in Figure 5.5 for the results of all investigated phase retrieval algorithms.

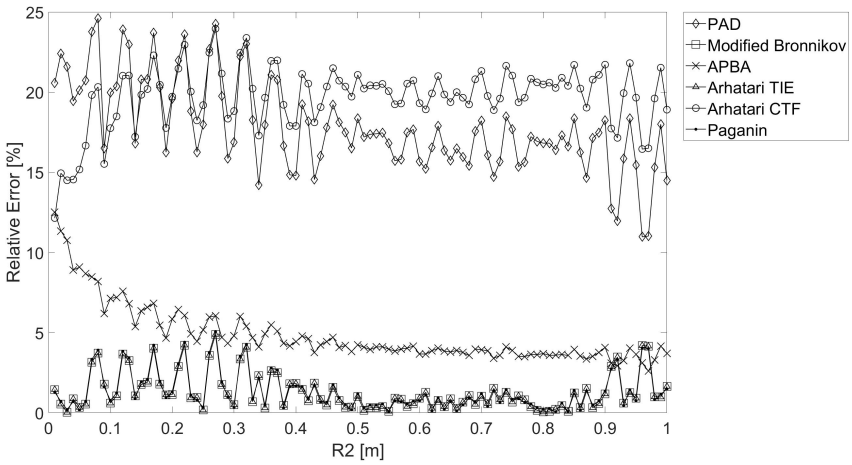

Figure 5.10: Relative error versus R_2 with $R_1 = 16$ cm for Kapton retrieved with different phase retrieval methods

Figure 5.11 shows similar results to Figure 5.6. Like in the polystyrene case, Modified Bronnikov method, Arhatari TIE method and Paganin's method have the lowest relative error for all source potentials in the case that Kapton is the material of choice. The relative errors of PAD and APBA decrease with increasing source potential, which is expected for PAD but not for APBA as explained in section 5.2.1. APBA does not perform as well as the other three methods when the source potential is greater than 100 kV for Kapton. Arhatari CTF method has increasing relative error when the source potential is increasing and surpasses the relative error of PAD around 100 kV.

Figure 5.12 shows that for pixel sizes less than 30 µm, Modified Bronnikov method, Arhatari TIE and Paganin's method perform the best for Kapton. All methods except for APBA relative errors increases significantly for pixel sizes between 40 µm to55 µm. In this range, APBA's relative error remains less than 10% and performs the best. For pixel sizes greater than 60 µm, PAD and Arhatari CTF method have the lowest relative errors out of all phase retrieval methods.

As in the case of polystyrene, Modified Bronnikov method, Arhatari TIE method and Paganin's method perform well under all tests cases for Kapton.

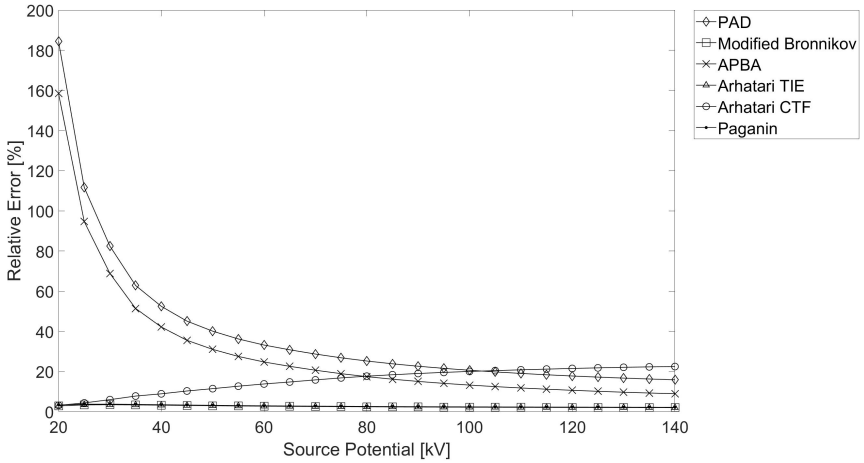

Figure 5.11: Relative error versus source potential for Kapton retrieved with different phase retrieval methods

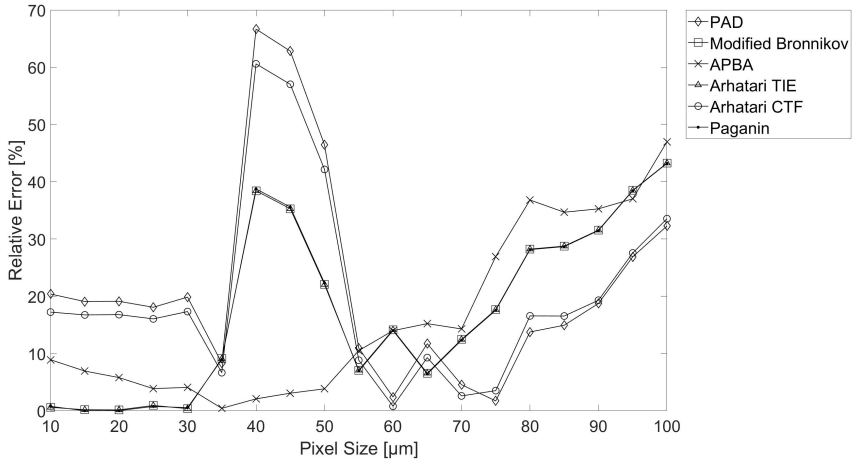

Figure 5.12: Relative error versus pixel size for Kapton retrieved with different phase retrieval methods

5.2.3 Polytetrafluoroethylene

PTFE is a higher density plastic used widely in industry. This plastic was chosen as it is the material used in experiment. PTFE parameters are described in Table 5.1.

Figure 5.13 shows the PTFE results for relative error versus thickness. For PTFE, it is obvious that Modified Bronnikov method, Arhatari TIE and Paganin's method perform the best with increasing object thickness as the relative errors remain stable below 5%. At thicknesses greater than 150 µm, Paganin's method performs better than Modified Bronnikov method and Arhatari TIE method. PAD stabilizes at a relative error of roughly 60%, APBA stabilizes around 40% and Arhatari CTF method stabilizes around 25%; thus making these methods undesirable to use for a material like PTFE. PAD performs the worst for PTFE and has relative errors that are roughly six times higher compared to polystyrene. The results from this plot compared to Figures 5.3 and 5.8 shows that all these methods are heavily material dependent. Each material gives different relative errors and express different behaviours.

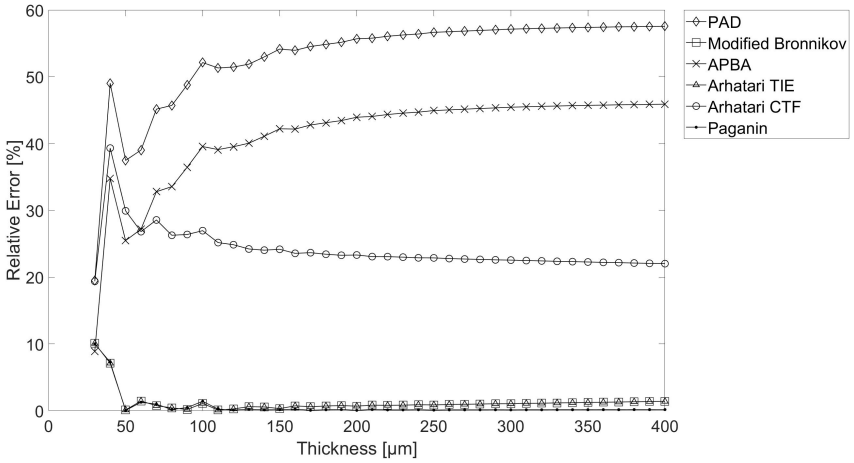

Figure 5.13: Relative error versus thickness for PTFE retrieved with different phase retrieval methods

Similar to the case of varying the thickness of PTFE, it is apparent in Figure 5.14 that Paganin's method, Modified Bronnikov method and Arhatari TIE method perform with the lowest relative error. Their relative error is under 5% until R_1 is greater than 0.5 m. At this point, the relative error reaches around 10%. Next, Arhatari CTF method performs with a relative error ranging from around 20% to 35%. Overall, APBA has a relative error similar to Arhatari CTF method. PAD has the highest relative error out of the seven methods, reaching values just over 50% for many R_1 values. The same oscillating behaviour is observed in Figure 5.14 as seen in Figures 5.4 and 5.9.

Figure 5.15 presents similar results in relative error to Figure 5.14, but in this case

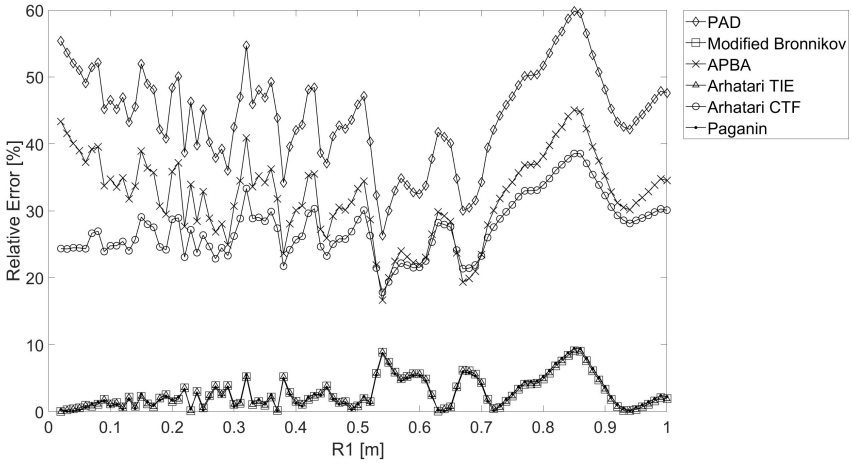

Figure 5.14: Relative error versus R_1 for PTFE retrieved with different phase retrieval methods

the ODD is being varied. Paganin's method, Modified Bronnikov method and Arhatari TIE method has a relative error consistently under 5% when R_2 is varied. Overall, the oscillations in relative error are more stable for varying R_2 than when R_1 is varied. PAD behaves the worst of the seven investigated methods with a relative error around 45% to 50%. APBA and Arhatari CTF method perform better than PAD, but still have relative errors around 30%.

Figure 5.16 shows the PTFE results for the relative error versus source potential. Similar to all other test cases, Paganin's method, Arhatari TIE method and Modified Bronnikov method perform the best. For low source potentials below 40 kV, Arhatari CTF method performs as well as the three previously mentioned methods. Past 40 kV, Arhatari CTF method's relative error increases, but generally has lower relative errror than APBA and PAD. The relative error of PAD and APBA decreases with increasing source potential, as it did with Kapton and polystyrene. This is expected for PAD, but not for APBA as described in section 5.2.1.

The trend of relative error versus pixel size seems to vary for each material, emphasizing that these phase retrieval algorithms tend to be highly material dependent. In the PTFE case seen in Figure 5.17, Modified Bronnikov method, Arhatari TIE method and Paganin's method have the smallest relative error for pixel sizes less than 65 µm. Past 65 µm, Arhatari CTF method performs with the lowest relative error up to a pixel size of 70 µm. When the pixel size is 75 µm, PAD has the lowest relative error. All the methods have a peak that

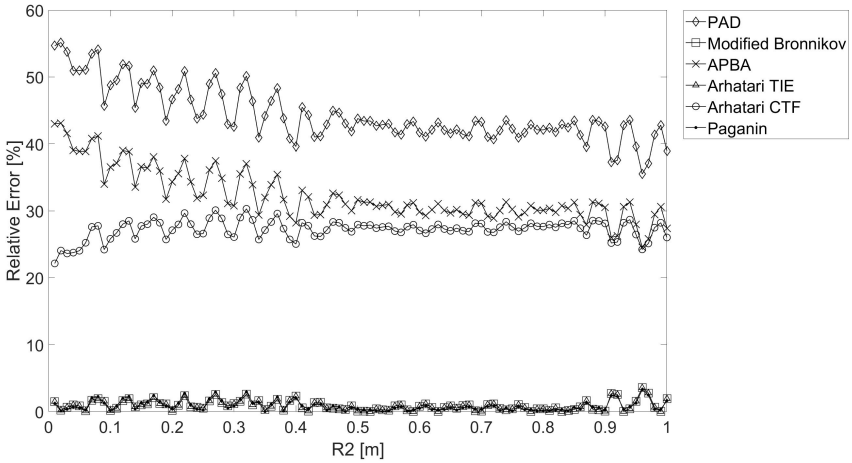

Figure 5.15: Relative error versus R_2 with $R_1 = 16$ cm for PTFE retrieved with different phase retrieval methods

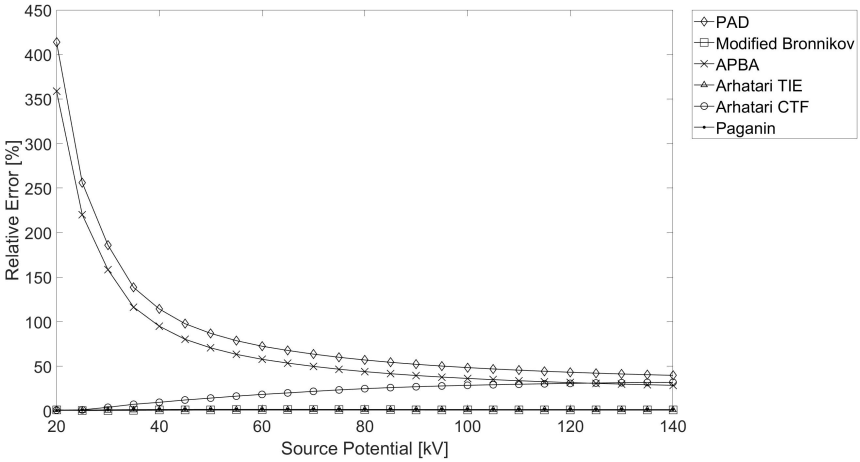

Figure 5.16: Relative error versus source potential for PTFE retrieved with different phase retrieval methods

forms in their relative errors that occurs around 45 µm.

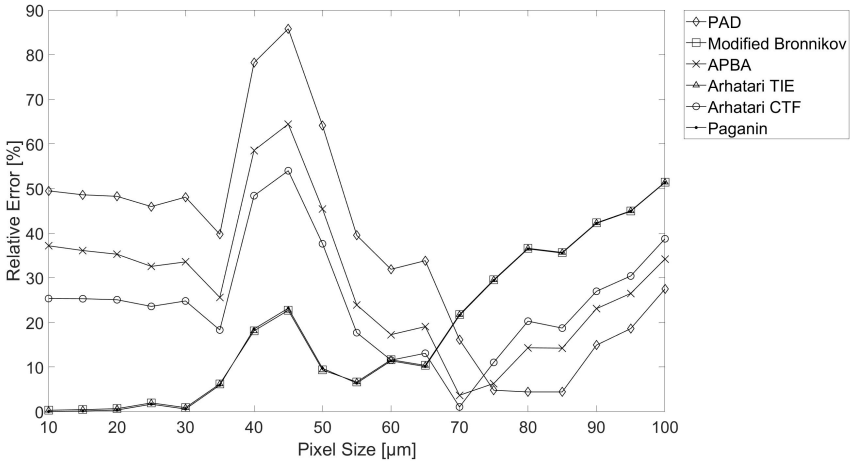

Figure 5.17: Relative error versus pixel size for PTFE retrieved with different phase retrieval methods

In conclusion, Paganin's method, Arhatari TIE method and Modified Bronnikov method perform the best under most cases for PTFE.

5.2.4 Conclusion

Observing the results in each section, it is difficult to tell if Paganin's method, Arhatari TIE method or Modified Bronnikov method performs with the lowest relative error. The results of Arhatati TIE method and Modified Bronnikov method overlap due to the fact that the α-value for the Modified Bronnikov method is set to Eq. 3.37 and, thus, results in the same equation as Arhatari TIE method. Observing the results more closely, it becomes apparent that Paganin's method generally has a lower relative error than Modified Bronnikov method and Arhatari TIE method. This is the most apparent in Figure 5.18. For this reason, Paganin's method is chosen as the best phase and/or thickness retrieval algorithm overall when imaging homogeneous materials with a polychromatic source.

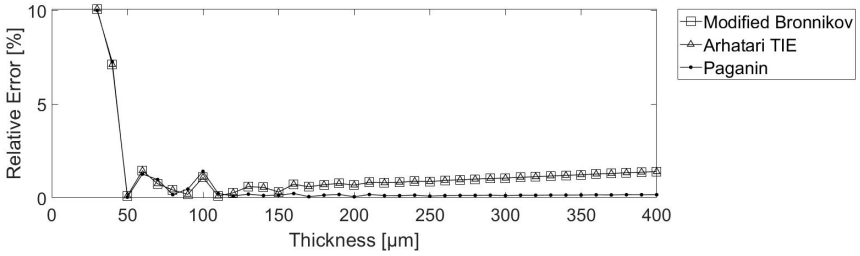

Figure 5.18: Relative error versus thickness for PTFE in comparing Modified Bronnikov, Arhatari TIE and Paganin's method

5.3 Validating APBA

APBA claims that it works for X-ray energies less than 60 keV, but, in simulation results, it can be seen that this method behaves similarly to the PAD method. It has a higher relative error for energies less than 60 keV and a reduced relative error for energies greater than 60 keV. This observation is tested in simulation using a monochromatic source to validate this conclusion, since this method was originally derived for a monochromatic source and has been extended to the polychromatic case. In the presence of a monochromatic source and all the same parameters used in the polychromatic simulation, it becomes apparent that this method is only valid for energies greater than or equal to 60 keV, unlike what the authors claimed in [21]. The results from this simulation can be seen in Figure 5.19. In the case of a polychromatic source, both PAD and APBA require most energies present in the spectrum to be greater than or equal to 60 keV in order for the error to decrease, therefore the source potential must be set to at least 120 kV or more. Even at these energies, it is apparent that the error is still relatively high.

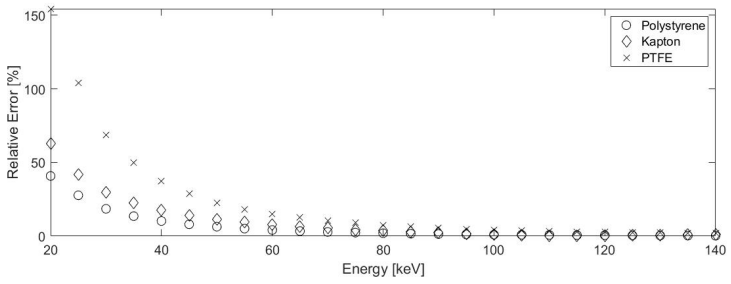

Figure 5.19: Relative error versus X-ray energy using APBA for different materials

Chapter 6

Experimental Results using Paganin's Method

Phase-contrast X-ray imaging has many advantages over conventional X-ray imaging when imaging low atomic number materials, such as 3D printed polymer composites or biological specimens. Propagation-based PCI has the easiest setup out of all the PCI methods, but has the hardest post-image processing. Its phase retrieval methods require many assumptions and, in many cases, that the material of the object to be known. As discussed in Chapter 5, Paganin's method shows the most promising results when the object is homogeneous and exposed by a polychromatic X-ray source. Biological specimens can generally be considered homogeneous materials. In this chapter, experimental results of PTFE will be discussed.

6.1 Methodology

A Thermo Scientific PXS5-927 MicroFocus X-ray Source was used to acquire images on a one-megapixel a-Se CMOS direct conversion detector with 7.8 µm pixel pitch made in-house in the STAR group at the University of Waterloo. The 40 kV and 60 kV spectrums are shown in Figure 6.1 and were acquired using the X-123 X-ray Spectrometer by Amptek. Pile-up may be an issue in these spectrums and a collimator is needed to reduce the number of photons hitting the photon counter. A collimator using lead was attempted, but some unknown peaks were appearing in the spectrum, thus these spectrums were not used for the investigation. Tungsten was used to try to fabricate a collimator, but it was too hard

of a material to produce a small hole with the current resources. In the end, a collimator kit was ordered for the spectrometer, but it did not arrive in time for the completion of this work. In Figure 6.2, the 40 kV and 60 kV spectrums with 2 mm of aluminum placed in front of the source to filter the tungsten Lα, Lβ and Lγ peaks were acquired using the spectrometer. Since a filter is placed in front of the source and acts as a collimator, not as many photons will be read on the spectrometer and thus more accurate X-ray spectrums are observed when filtered with 2 mm of aluminum.

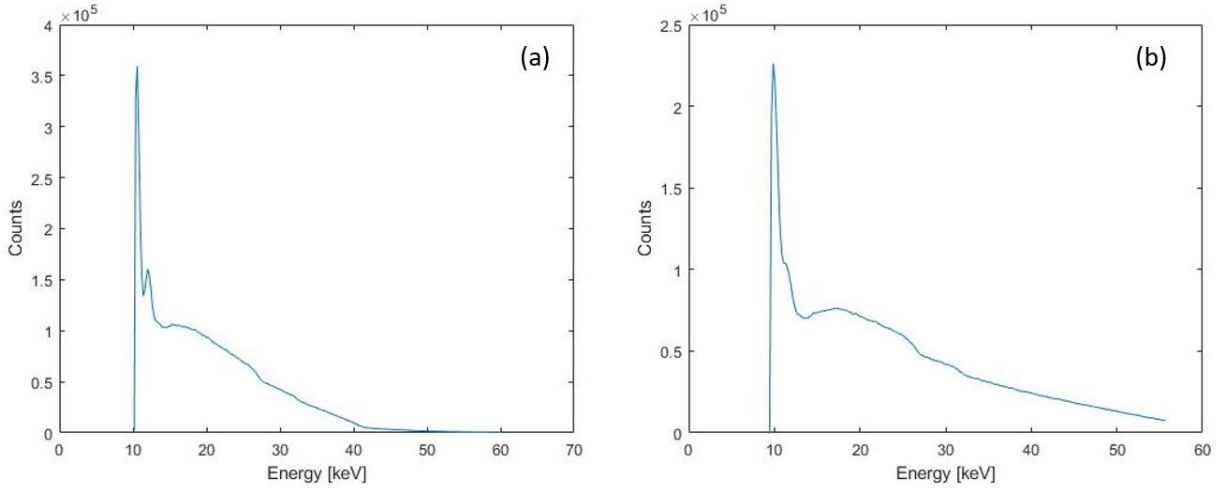

Figure 6.1: X-ray spectrums of the Thermo Scientific PXS5-927 Microfocus X-ray source acquired using the X-123 X-ray Spectrometer (a) 40 kV and (b) 60 kV.

The final X-ray imaging setup is depicted in Figure 6.3. The X-ray imaging setup consisted of the Thermo Scientific source being placed at a known SOD from the object. The object was placed on three Thorlabs motorized stages: a rotational stage, a x-direction stage and y-direction stage. These stages allowed for ease in positioning the object in the center of the detector. The detector is placed at a known ODD from the object. The SOD and ODD are measured using calipers. The positioning of the X-ray source and detector are controlled using manual x-direction and y-direction Thorlabs stage. A laser is used to ensure alignment of the entire system.

A software created by KA Imaging, Inc. is used to acquire images. The integration time used in experiment was 1 second and an average of 30 images was used. First, a dark image was acquired after letting the detector warm-up for 30 minutes and was acquired before each new image of the object was acquired. After 30 minutes, the detector's dark noise is stabilized. Also, an open image, where the detector is exposed to X-rays without

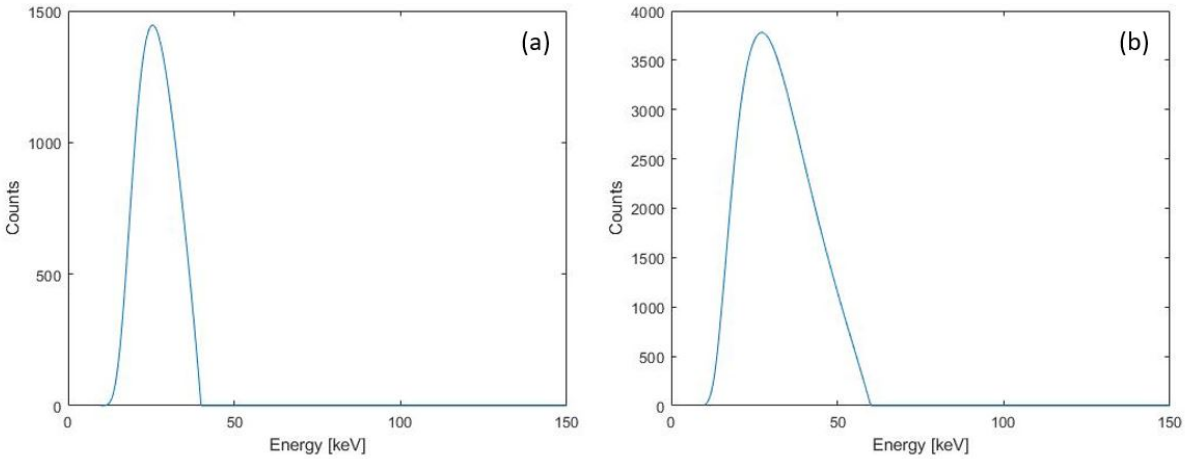

Figure 6.2: X-ray spectrums of the Thermo Scientific PXS5-927 Microfocus X-ray source acquired using the X-123 X-ray Spectrometer and 2 mm of aluminum placed in front of the source as a filter (a) 40 kV and (b) 60 kV.

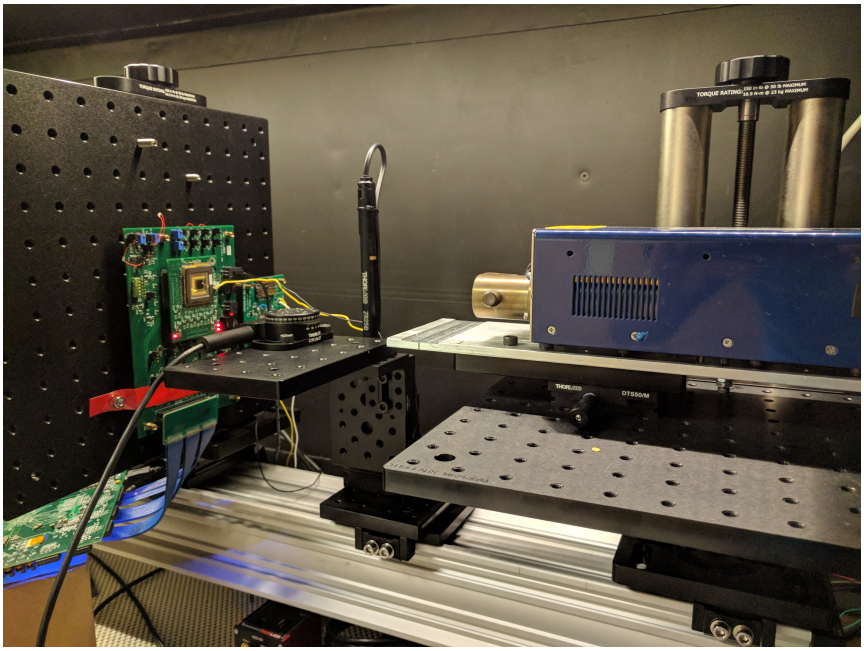

Figure 6.3: X-ray imaging setup

the presence of the object, was acquired before each new image of the object was acquired. The open and dark images are used in post-image processing to calculate the gain corrected image that is inputted into the phase retrieval algorithm. The gain corrected algorithm is outlined in Appendix E.1.

The material that was mainly investigated in experiment was PTFE, which was purchased from McMaster Carr in different diameters of spheres and cylinders. The PTFE samples have a known density of 2.13 g/cm^3 and a diameter tolerance of -0.002 inch to 0.002 inch. This density is slightly less than the density used in simulation for Teflon, which is 2.2 g/cm^3. The diameters of the PTFE objects used in experiment are outlines in Table 6.1. Next, the object was placed at a known distance from the source (R_1) and a known distance from the detector (R_2) that were measured using a caliper. The spheres were mounted on plasticine and the cylinders were mounted using a Thorlabs mount. Each image is gain corrected and Paganin's method is run on each gain corrected image. An average of the background profile is subtracted from the maximum thickness of the object to estimate the retrieved thickness. The phase retrieval experimental code is presented in Appendix E.2. Three of these estimates are calculated and averaged to estimate the total retrieved thickness of the object. The relative error is calculated using Eq. 5.1.

Table 6.1: PTFE Shapes

Size (inch)	Size (mm)	Tolerance (mm)	Shape
0.028	0.7112	-0.0508 to 0.0508	Cylinder
0.039	0.9906	-0.0508 to 0.0508	Cylinder
0.055	1.3970	-0.0508 to 0.0508	Cylinder
1/16	1.5875	-0.0508 to 0.0508	Sphere
3/32	2.38125	-0.0508 to 0.0508	Sphere
1/8	3.175	-0.0508 to 0.0508	Sphere

6.2 Experimental Results

In this section, experimental results that were acquired using the unfiltered spectrums (seen in Figure 6.1) and using the filtered spectrums (seen in Figure 6.2) are presented. Overall, the unfiltered images have lower noise than the filtered images. The increased noise in the filtered images could be do to scattering caused by the aluminum filter that is placed

between the source and object. Paganin's method is able to retrieve a smooth profile for the unfiltered images, although the results are not quantitative with high relative error. The filtered images resulted in higher relative error than the unfiltered images. Paganin's method is able to increase the signal-to-noise ratio (SNR) by Fourier filtering, but the thickness retrieved images obtained using a filtered spectrum still present high noise that could be caused by backscattering.

6.2.1 Using Unfiltered Spectrums

Figure 6.4 shows a phase-contrast (a) and thickness retrieval (b) image of the 0.028" PTFE cylinder acquired with the 60 kV Thermo Scientific spectrum (see Figure 6.1 (b)) at an SOD of 8 cm and ODD of 8 cm. The edge enhancement is clear in the phase-contrast image and appears as a bright white interface. In the thickness retrieved image, Paganin's method eliminated this interface to create a smooth profile. From this image, it appears that there are no voids within the cylinder. In appearance, the thickness retrieved image resembles what would be expected after Paganin's Fourier filter is applied.

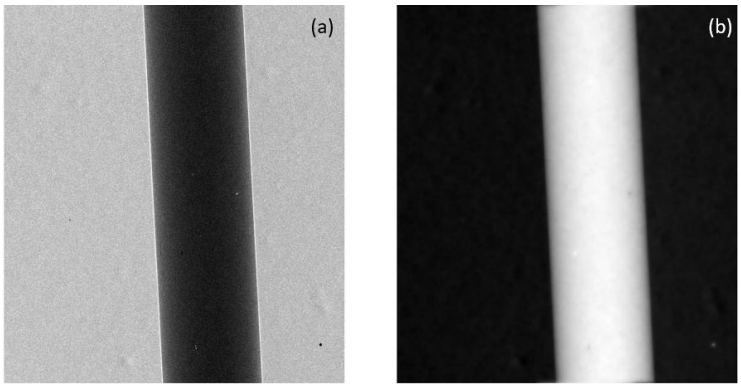

Figure 6.4: 0.028" PTFE cylinder imaged with a 60 kV spectrum at R1 = 8 cm and R2 = 8 cm, (a) phase contrast image and (b) thickness retrieval image using Paganin's method

The intensity profile shows the edge enhancement at the boundaries in the form of peaks is seen in Figure 6.5 (a), with one peak occurring around pixel number 100 and the other peak occurs around 290. The intensity profile is a bit noisy, which is most likely due to photon noise, and makes it harder to distinguish the peaks that represent the boundary of the object at pixel number 290. With Paganin's thickness retrieval, the thickness profile of the object was retrieved and presented in Figure 6.5 (b). Paganin's method reduces the noise in the image by Fourier filtering, in turn increasing the SNR.

The true thickness value of the cylinder is 0.7112 mm; whereas Paganin's method retrieved an average thickness value of 0.782554 mm for this image, which results in a relative error of 10%. This relative error is low and acceptable for this object. It is close to some of the predicted relative errors from simulation considering only 30 images were averaged to achieve this profile.

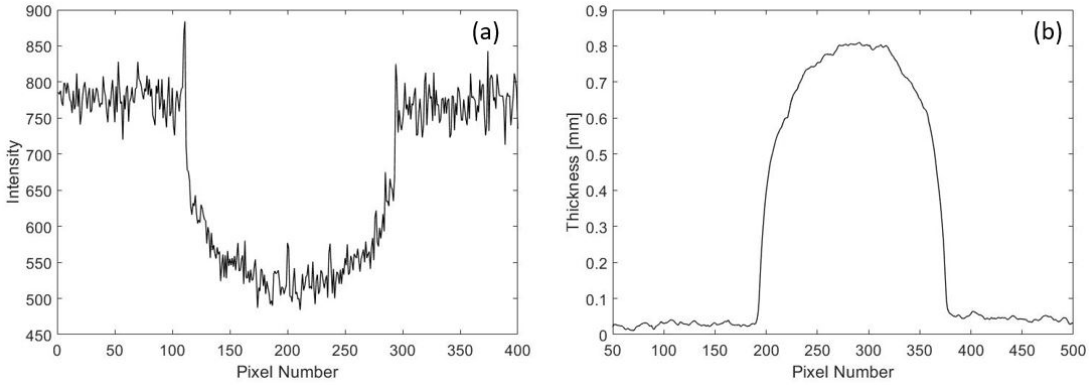

Figure 6.5: 0.028" PTFE cylinder imaged with a 60 kV spectrum at R1 = 8 cm and R2 = 8 cm, (a) phase contrast profile and (b) thickness profile retrieved using Paganin's method

Figure 6.6 shows a phase-contrast (a) and thickness retrieval (b) image of the 1/16" PTFE sphere acquired using a 60 kV spectrum at an SOD of 36 cm and ODD of 8 cm. As in the cylinder image, the edge is well defined and the thickness retrieval creates a smooth profile. The bright white edge enhancement is eliminated using Fourier filtering in Paganin's method and results in a clean, smooth image. There appears to be no voids present in this object. In both images, some defects from the detectors are visible that could not be corrected for with gain correction.

It is hard to observe the edge enhancement in the intensity profile of the sphere shown in Figure 6.7 (a) due to the surrounding noise in the image that is most likely caused by photon noise. The edge enhancement peaks for the sphere occur at pixel numbers 40 and 230. Paganin's method increased the SNR by Fourier filtering and the retrieved thickness profile, seen in Figure 6.7 (b), appears much smoother than the intensity profile. The retrieved thickness of the sphere is 1.237525 mm and the true thickness of this object is 1.5875 mm. This results in a relative error of 22%, which is higher than that measured for the 0.7112 mm cylinder. This relative error is much higher than the errors predicted in simulation. A lower relative error for this object is desirable.

A larger sample size was acquired using all the shapes described in Table 6.1 at different

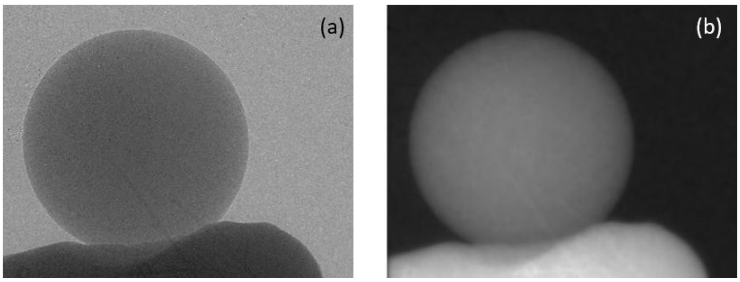

Figure 6.6: 1/16" PTFE sphere imaged with a 60 kV spectrum at R1 = 36 cm and R2 = 8 cm, (a) phase contrast image and (b) thickness retrieval image using Paganin's method

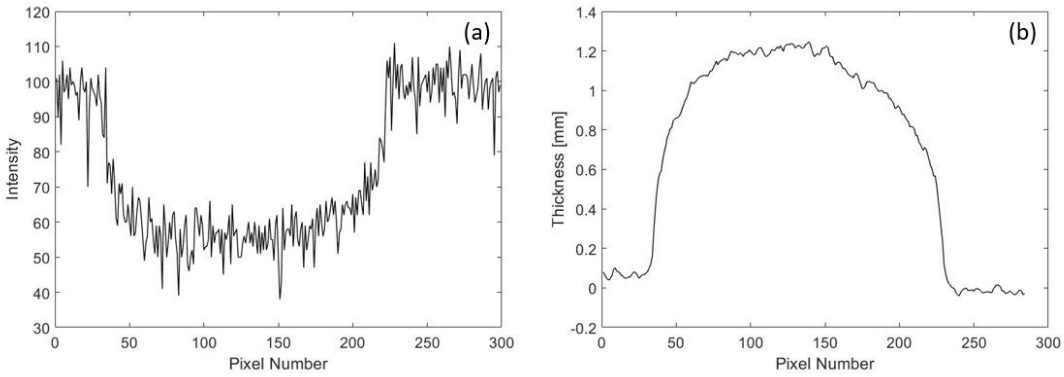

Figure 6.7: 1/16" PTFE sphere imaged with a 60 kV spectrum at R1 = 36 cm and R2 = 8 cm, (a) phase contrast profile and (b) thickness profile retrieved using Paganin's method

SOD and ODD. These results are shown in Figures 6.8 and 6.9. Generally, the SOD was set to either 8 cm, 18 cm or 36 cm and the ODD was varied. As a result, the magnification is varied from 1.22 to 3.67. In Figure 6.8, the relative error versus the object's thickness is shown and it can be seen that the cylinder with a diameter of 0.7112 mm and 0.9906 mm generally have the lowest relative error compared to the 1.3970 mm diameter cylinder, and the 1.5875 mm, 2.38125 mm and 3.175 mm diameter spheres. The 3.175 mm sphere has the highest relative error. Next, the retrieved thickness versus the measured thickness is plotted in Figure 6.9 to see if a trend can be observed. The retrieved thickness is the thickness obtained from Paganin's method and the measured thickness is the thickness of the object measured with the caliper. No clear trend is observed from these results, although a polynomial of third degree would be the best representation and gives an R-squared value of 0.9680; whereas a linear trend gives an R-squared value of 0.9342 and a

polynomial of second degree gives an R-squared of 0.9641. The R-squared value does not improve when increasing the polynomial order past third degree.

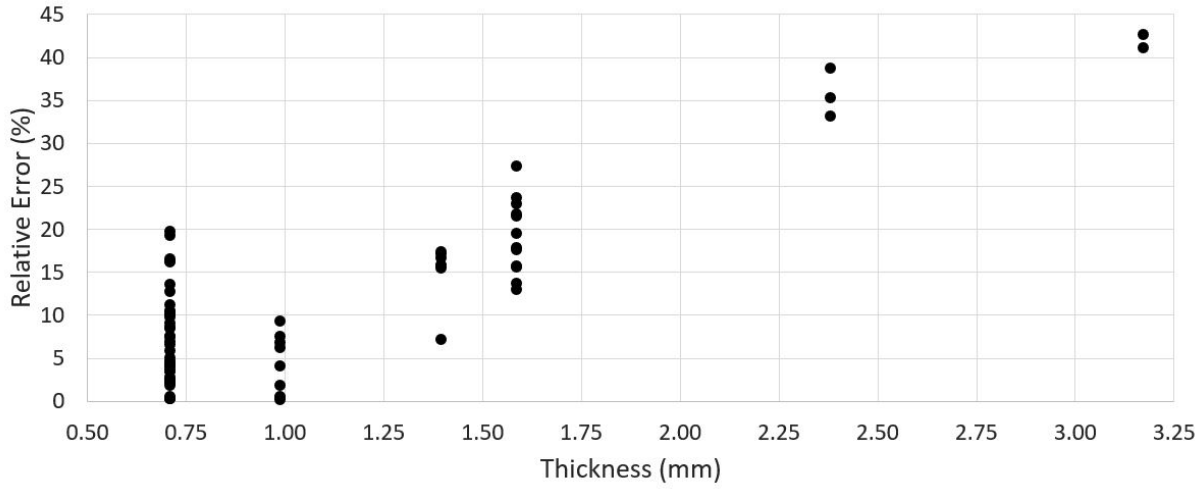

Figure 6.8: Relative error versus thickness for PTFE spheres and cylinders experimentally imaged using a 60 kV spectrum

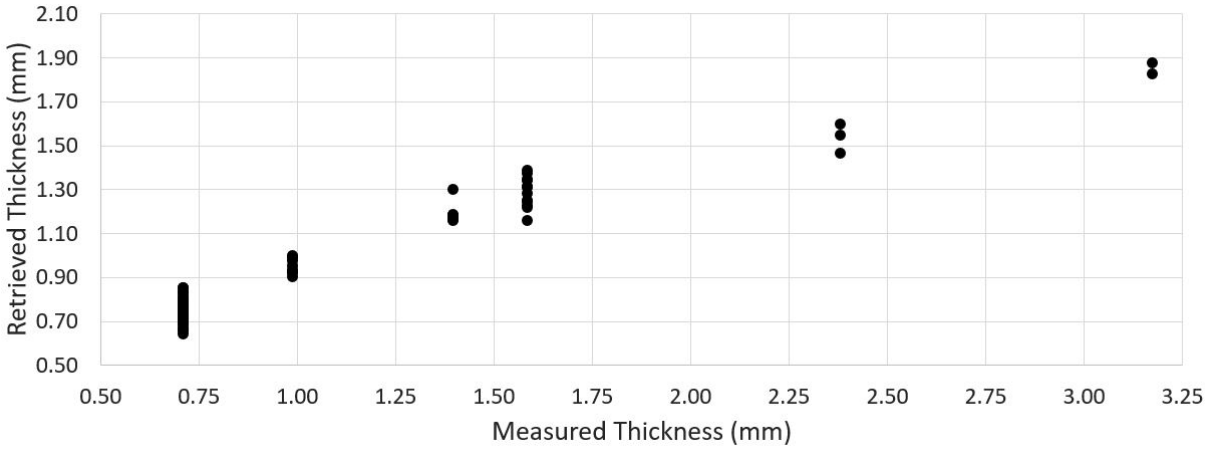

Figure 6.9: Retrieved thickness versus measured thickness for PTFE spheres and cylinders experimentally imaged using a 60 kV spectrum

Next, the objects were imaged using the 40 kV Thermo Scientific spectrum to see if there would be any improvement in the thickness retrieval of PTFE. The SOD was set

to either 8 cm, 15 cm or 36 cm and the ODD was varied, resulting in a magnification variation of 1.22 to 2. Overall, the phase-contrast and thickness retrieved images obtained using the 40 kV spectrum match the images seen in Figures 6.4 and 6.6 in appearance. The relative error versus object thickness is plotted in Figure 6.10. The results using the 40 kV spectrum are quite different from those obtained using the 60 kV spectrum because the smallest diameter cylinder has the largest error ranging from 33% to 41%; whereas the smallest error ranging from around 1% to 4% is achieved by the 0.9906 mm cylinder and 1.5875 mm sphere. The retrieved thickness versus measured thickness is plotted in Figure 6.11. The best representation of this curve is either a second degree polynomial, which results in an R-squared value of 0.9731. A linear trend gives an R-squared of 0.9556, therefore is not the best representation.

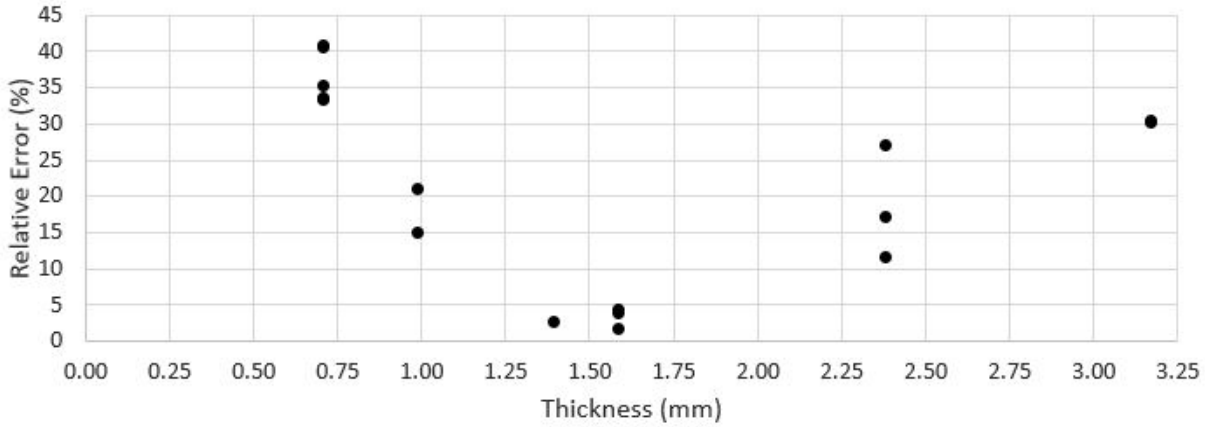

Figure 6.10: Relative error versus thickness for PTFE spheres and cylinders experimentally imaged using a 40 kV spectrum

The equations derived for the trends depicted in Figures 6.9 and 6.11 are presented in Table 6.2, where y is the retrieved thickness and x is the measured thickness.

Table 6.2: PTFE experimental result trends using unfiltered Thermo Scientific spectrums

Source Potential (kV)	Equation	R^2
40	$y = -0.0999x^2+0.8933x+0.3845$	0.9731
60	$y = -0.1109x^2+0.8594x+0.1924$	0.9641
60	$y = 0.0789x^3-0.5344x^2+1.5107x-0.0898$	0.968

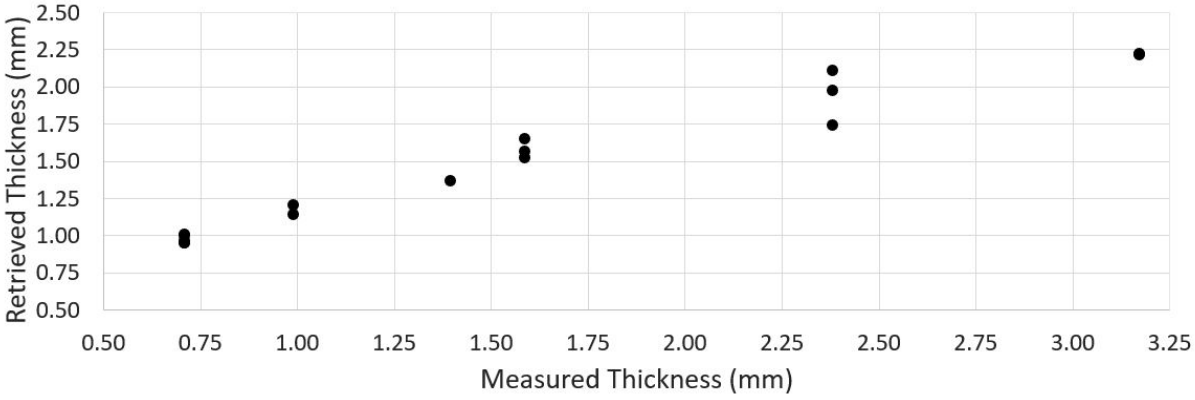

Figure 6.11: Retrieved thickness versus measured thickness for PTFE spheres and cylinders experimentally imaged using a 40 kV spectrum

Although the resulting phase-contrast and thickness retrieval images look clean and appear as one would expect a phase retrieved image, the results are not accurate.

6.2.2 Using Filtered Spectrums

An attempt to improve the results was made by filtering the spectrum with 2 mm of aluminum, as seen in Figure 6.2, to eliminate low energy photons, therefore reducing the tungsten Lα, Lβ and Lγ peaks.

As can be seen in Figures 6.12 and 6.13, filtering causes the images to be noisy and artefacts become present even when acquiring the images with a 3 second integration time and averaging 100 images. The cylinder in Figure 6.12 was acquired using the 40 kV Thermo Scientific spectrum filtered with 2 mm of aluminum (see Figure 6.2 (a)). The sphere in Figure 6.13 was acquired using the 60 kV Thermo Scientific spectrum filtered with 2 mm of aluminum (see Figure 6.2 (b)). Some of these artefacts are caused by possible crystallization of the detector. It is hard to distinguish the peaks from the noise in the phase-contrast profiles shown in Figures 6.14 (a) and 6.15 (a) of the cylinder and sphere, respectively. Considering how noisy these profiles are, Paganin's method is able to increase the SNR significantly and a thickness profile can easily be seen in Figures 6.14 (b) and 6.15 (b) of the cylinder and sphere, respectively. Although these profiles are smooth with little noise present, the retrieved thickness values for these objects is incorrect. In Figure 6.14, the actual thickness of the cylinder is 0.7112 mm and the average retrieved thickness is 0.4033 mm, which results in a relative error of 43.29%. The actual thickness of the sphere

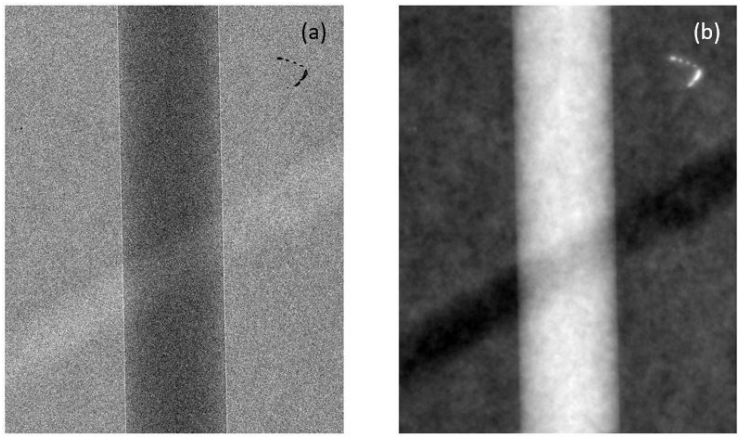

Figure 6.12: 0.028" PTFE cylinder imaged with a 40 kV spectrum filtered with 2 mm aluminum at R1 = 15 cm and R2 = 15 cm, (a) phase contrast image and (b) thickness retrieval image using Paganin's method

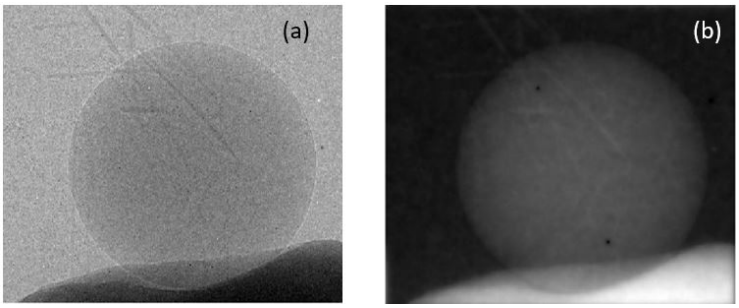

Figure 6.13: 1/16" PTFE sphere imaged with a 60 kV spectrum filtered with 2 mm aluminum at R1 = 36 cm and R2 = 8 cm, (a) phase contrast image and (b) thickness retrieval image using Paganin's method

in Figure 6.14 is 1.5875 mm and the average retrieved thickness is 0.66243 mm, resulting in a relative error of 58.27%. Due to the relative errors being high, the filtered spectrums were not used for many experimental results. The data acquired for these images was far too noisy to determine the thickness. It is possible that backscattering of X-rays caused by the aluminum filter placed in front of the X-ray source is a source of the increased noise in these images compared to the unfiltered images. Photon noise is also prominent in the images acquired using a filtered spectrum. The noise in the images makes it difficult to conclude a trend with the retrieved thickness, thus is not presented.

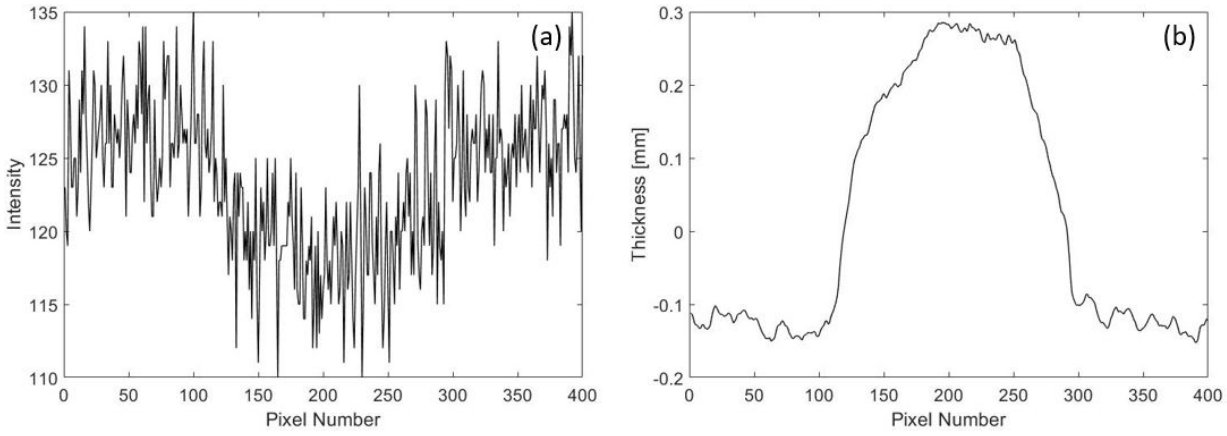

Figure 6.14: 0.028" PTFE cylinder imaged with a 40 kV spectrum filtered with 2 mm aluminum at R1 = 15 cm and R2 = 15 cm, (a) phase contrast profile and (b) thickness profile retrieved using Paganin's method

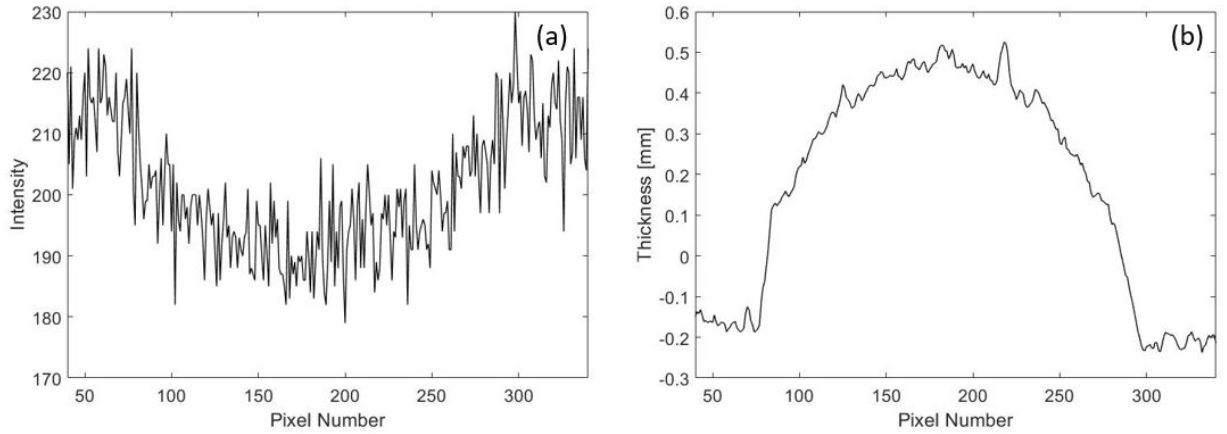

Figure 6.15: 1/16" PTFE sphere imaged with a 60 kV spectrum filtered with 2 mm aluminum at R1 = 36 cm and R2 = 8 cm, (a) phase contrast profile and (b) thickness profile retrieved using Paganin's method

6.3 Finding the Energy that Retrieves the Correct Thickness

To further view if there is a correlation in the experimental results, the phase coefficient $\delta(E)$ and linear attenuation coefficient $\mu(E)$ values where Paganin's method retrieves the correct thickness for a specified image was attempted. To find δ and μ, the code iterated through $\delta(E)$ and $\mu(E)$ sequentially according to a specified energy. The minimum relative error was calculated and the iteration number at which it occurs is returned. The one problem with this method is that the phase coefficient and the linear attenuation coefficient vary differently with respect to energy. The phase coefficient varies as $\frac{1}{E^2}$ and the linear attenuation coefficient varies as $\frac{1}{E^3}$. Overall, this method gives a good estimation of the correct phase and linear attenuation coefficients required to retrieve the correct thickness. The energy where the lowest relative error was achieved for all the PTFE objects that were imaged using the 60 kV spectrum is plotted in Figure 6.16. The average energy that retrieves the correct thickness is 14.7740 keV, although the phase and attenuation coefficients at this energy can cause large relative errors for the images in which a slightly higher or lower energy is required to define the phase and linear attenuation coefficients to retrieve the correct thickness. Overall, there is no trend found in the energy that returns the correct thickness with respect to the thickness of the object. These results show that further investigation is required in order to figure out the sources of error when using Paganin's method on different materials, thicknesses and shapes with different spectrums.

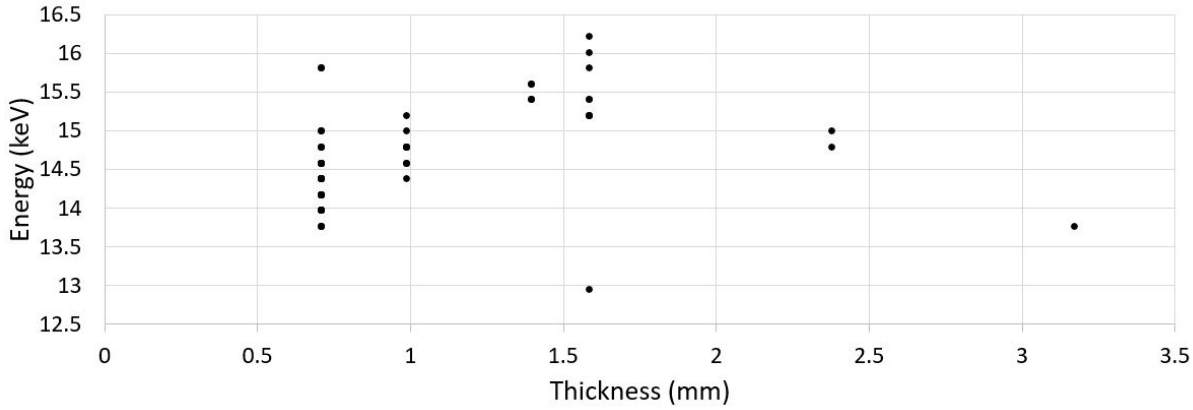

Figure 6.16: The energy at which the phase and attenuation coefficients retrieve the correct thickness for a selected image using the 60 kV Thermo Scientific spectrum

6.4 Sources of Error

After reviewing all the experimental data, it is clear that there are problems arising in the system that are causing error to arise in the retrieved thickness. In simulation, Paganin's method performs with relatively small relative error for the test cases presented to it in Chapter 5. There are three regions where the sources of error could arise, which are: the source, the object or the detector. It is possible if the spectrum of the source is not properly characterized, this could cause a source of error. With these objects, the density, material and actual thickness are well known; therefore a possible source of error is that these objects are no longer considered sufficiently thin for PTFE and, thus, causing Paganin's method to fail. To see if the thickness of the object is a source of error, a thin piece of kapton that was on the order of 10 µm was imaged. Kapton is a well-known purely phase object that is used in many journal articles to access their PCI system, although many of the systems require over 30 minute imaging time. The results of the kapton sample were too noisy using our detector to process with Paganin's method even with an unfiltered spectrum and over 100 images averaged. From the detector side, noise can introduce a source of error. The easiest way to access these sources of error separately is by running simulations on different types of material, using different spectrums and changing the SOD and ODD. In experiment, it is very difficult to identify where the error is coming from when there are three sources where the error can arise. The next chapter will investigate and discuss some of these possible causes of error in further detail by means of simulation.

Chapter 7

Effect of Parameters on Paganin's Method

As seen in Chapter 6, there are certain parameters that can introduce sources of error in the quantitative results, but it is challenging to define exactly where the source of error is coming from within the system. The three areas where the source of error can arise are the source, the object and/or the detector. It is difficult to distinguish in experiment where the source of error is arising within the system; thus, in this chapter, the sources of error will be investigated through simulations.

7.1 Effect of Material on Paganin's Method

Paganin mentions that a material is required to be sufficiently thin for this method to retrieve the correct phase or thickness, although it does not mention what is considered sufficiently thin. This statement is material dependent. In this section, different materials are investigated to see when Paganin's method fails to retrieve the correct thickness and the behaviour of the results when it does fail. Different spectrums were used for each material and the thickness was retrieved for materials that are greater than 100 µm since most plastic objects used in both experiment and industry tend to be thicker than 100 µm. In Chapter 5, thinner samples ranging up to 400 µm were already simulated and investigated. In experiment, the sample thickness exceeded the thicknesses simulated in Chapter 5, therefore further investigation is required. The material parameters used in the simulations are outlined in Table 7.1.

Table 7.1: Material Properties

Material	Composition	Density [g/cm^3]
PTFE	$(C_4F_4)_n$	2.2
Polystyrene	$(C_8H_8)_n$	1.04
Aluminum	Al	2.7
Tungsten	W	19.3
Kevlar	$(COC_6H_4CONHC_6H_4NH)_n$	1.44

A comparison between the thickness results from a PTFE sphere and cylinder simulated using a 60 kV Thermo Scientific spectrum is made in Figure 7.1 to ensure there was no variation between the results when using a different geometrical shape. The results for the retrieved thickness of a sphere and cylinder of the same theoretical thickness overlap, therefore a cylinder can be used for all the remaining simulations as it takes less computation time to simulate. The theoretical thickness is the thickness value of the simulated object and the retrieved thickness is the value retrieved from the phase-contrast X-ray image using Paganin's method. Further proof that a sphere and cylinder result in the same retrieved thickness for each theoretical thickness can be seen in Figure B.1.

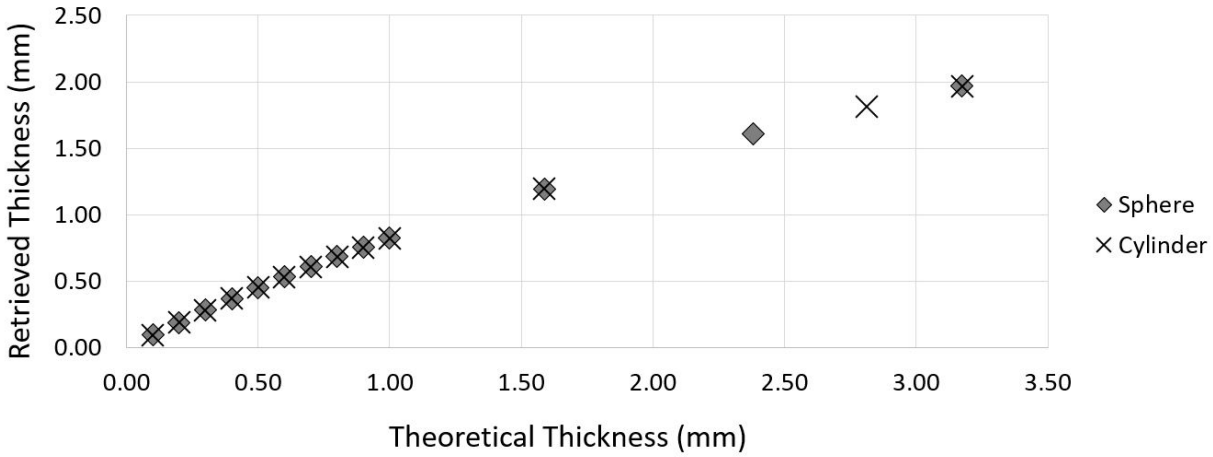

Figure 7.1: Retrieved thickness versus theoretical thickness comparing the results of a simulated PTFE sphere and cylinder using the 60 kV Thermo Scientific spectrum

Next, simulating PTFE cylinders with a 60 kV Thermo Scientific spectrum at different

R_1 and R_2 values are shown in Figure 7.2 to see if there is a trend of the retrieved thickness for thicker materials and replicate the experimental case without noise. It appears that changing the R_1 and R_2 values in the perfect noise-free case does not have an effect on the results. The relative error of the thickness of PTFE surpasses 10% when the theoretical thickness is set to 500 µm. Past this point, all three data series appear to behave as a second-degree polynomial when the retrieved thickness is plotted against the theoretical thickness. All three data series result in similar polynomial expressions tabulated in Table 7.2 with an R-squared value of 0.999. Henceforth, in the equations, 'y' is the retrieved thickness in millimeters and 'x' is the theoretical thickness in millimeters. It appears that if an equation is known for any R_1 and R_2 values, the actual thickness of the PTFE object imaged at 60 kV using the Thermo Scientific spectrum should be derivable by substituting the retrieved thickness in for 'y' and solving for 'x'.

Comparing the resulting equations from simulation in Table 7.2 to the equations observed for the 60 kV spectrum with the experimental data in Table 6.2, it is observed that both in simulation and experimentally the trend of the data points tends to be quadratic. The second coefficient of the experimentally found equation is close in value to the second coefficient of the equation found through simulation, being 0.8594 and 0.8123, respectively. Otherwise, the first and last coefficients of the equations found experimentally and in simulation are quite different, with the first coefficient of the experimental results being 1.77 times greater than the simulation results and the third coefficient of the experimental results being 3.57 times greater than the simulation result. Overall, the only similarity in the resulting equations when using the 60 kV Thermo Scientific spectrum is that both simulation and experimental results behave quadratically.

Table 7.2: Polynomial expressions of PTFE cylinders at different R_1 and R_2 values using the 60 kV Thermo Scientific spectrum

R_1 (cm)	R_2 (cm)	Equation	R^2
8	16	y = -0.0626x^2+0.8123x+0.0539	0.999
8	8	y = -0.0626x^2+0.8123x+0.0538	0.999
15	30	y = -0.0627x^2+0.8126x+0.0537	0.999

When the theoretical thickness is set to 4.35 mm, the retrieved thickness of this sample is 2.43 mm and results in a relative error of 44%. To try to improve the relative error, PTFE is simulated using 60 kV Thermo Scientific spectrum filtered with 2 mm of aluminum. The

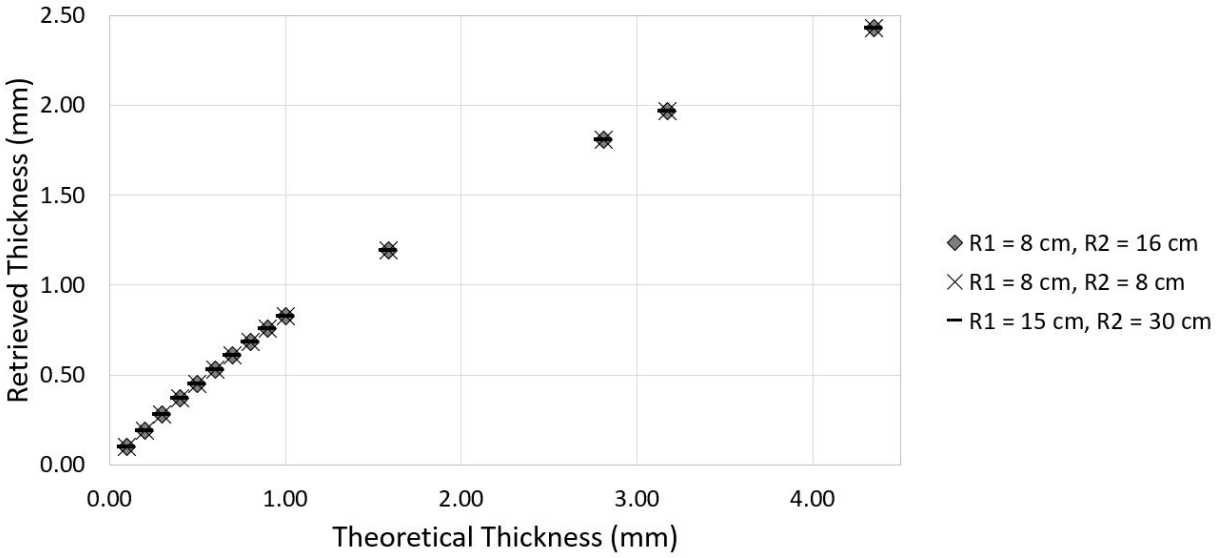

Figure 7.2: Retrieved thickness versus theoretical thickness of a PTFE cylinder varying R_1 and R_2 using the 60 kV Thermo Scientific spectrum

results are presented in Figure 7.3. The relative error for a theoretical thickness of 4.35 mm reduced to 14%, although a second-degree polynomial trend is still present between the retrieved thickness and theoretical thickness. The polynomial equations for the two different R_1 and R_2 values are almost the same with the only different being the last coefficient that has a difference of $1\text{x}10^{-4}$, as seen in Table 7.3. Both equations result in an R-squared value of 1, which represents a perfect fit. Overall, it appears as though a filtered spectrum should give results with lower relative error for thicker PTFE objects. Even a PTFE object with a theoretical thickness of 7 mm should result in a relative error of around 20%, which is a better result than what was seen using a spectrum that is not filtered.

These filtered spectrum results contradict what was seen in the experimental case. Experimentally, the unfiltered spectrum produces lower relative error results when using Paganin's method compared to the filtered spectrum results. This contradiction could be due to the fact that the filtered images appeared to be severely affected by noise in the experimental case; whereas there is no noise present in the simulation case. The noise in the experimental images might have been caused by X-ray backscattering of the aluminum filter. If this backscattering could be diminished or eliminated, it is possible the filtered spectrum could produce thickness retrieved results with lower relative error for thicker objects as seen in simulation.

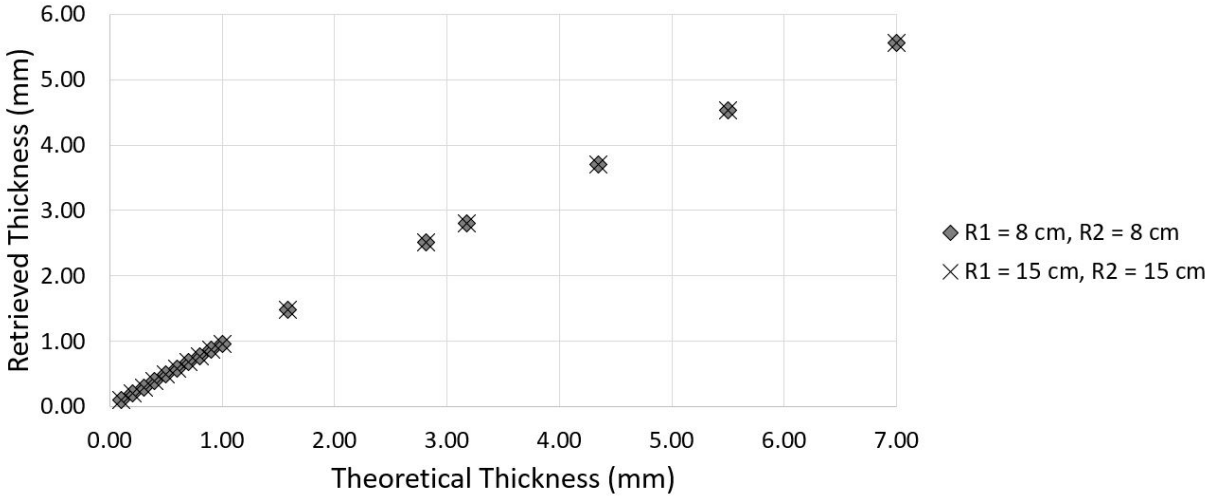

Figure 7.3: Retrieved thickness versus theoretical thickness of a PTFE cylinder varying R_1 and R_2 using the 60 kV 2 mm Al filtered Thermo Scientific spectrum

Table 7.3: Polynomial expressions of PTFE cylinders at different R_1 and R_2 values using the 60 kV 2 mm Al filtered Thermo Scientific spectrum

R_1 (cm)	R_2 (cm)	Equation	R^2
8	16	y = -0.0228x^2+0.9496x+0.0195	1
15	15	y = -0.0228x^2+0.9496x+0.0196	1

In Appendix B, Figure B.2 depicts similar results to Figure 7.2. Table 7.4 outlines the equations that describe the quadratic trends of the simulated data sets. The equations derived from the simulation results are similar for varying R_1 and R_2 values. Comparing these equations with the equation for the 40 kV Thermo Scientific spectrum experimental results found in Table 6.2, they are very different and the only similarity is that both the experimental and simulation data behave quadratically.

Next, polystyrene cylinders are simulated using the 60 kV Thermo Scientific spectrum and the results are presented in Figure 7.4. Due to the lower density of polystyrene, the

Table 7.4: Polynomial expressions of PTFE cylinders at different R_1 and R_2 values using the 40 kV Thermo Scientific spectrum

R_1 (cm)	R_2 (cm)	Equation	R^2
8	8	y = -0.0592x^2+0.8779x+0.0366	0.9909
15	15	y = -0.0593x^2+0.8783x+0.0361	0.9994
8	15	y = -0.0592x^2+0.8779x+0.0366	0.9996

trend of relative thickness versus theoretical thickness is linear compared to the quadratic trend of PTFE. The linear expressions are tabulated in Table 7.5 and are similar at different R_2 values. This means that one of two expressions may be used for either R_2 value with the introduction of a small error. In Appendix B, Figure B.3 also shows a linear trend for polystyrene simulated with a 40 kV Thermo Scientific spectrum, thus this trend is consistent with polystyrene and the unfiltered Thermo Scientific spectrums.

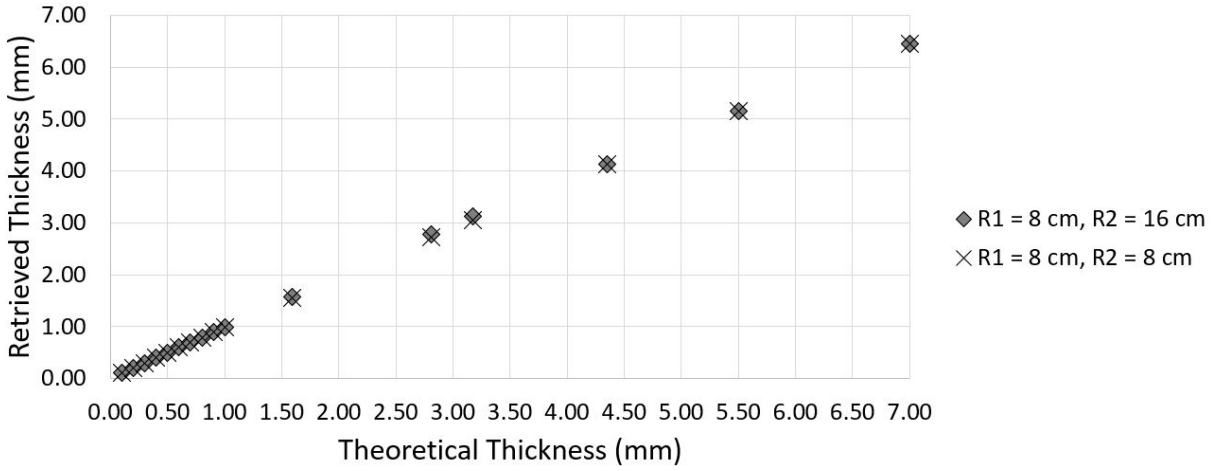

Figure 7.4: Retrieved thickness versus theoretical thickness of a polystyrene cylinder varying R_2 using the 60 kV Thermo Scientific spectrum

Further, a L12531 Hamamatsu source is used in the simulation of the polystyrene cylinders with a source potential of 60 kV. The L12531 Hamamatsu source is a source that is currently being purchased for the phase-contrast X-ray system, and, accordingly, it is also investigated in this analysis. The spectrums are provided by Hamamatsu for the simulation

Table 7.5: Linear expressions of polystyrene cylinders at different R_1 and R_2 values using the 60 kV Thermo Scientific spectrum

R_1 (cm)	R_2 (cm)	Equation	R^2
8	16	y = 0.9307x+0.0525	0.9991
8	8	y = 0.9285x+0.0467	0.9996

and are confidential. For this reason, the spectrums are not shown in this thesis. The source has a tungsten target and, thus, has the Lα, Lβ and Lγ peaks present. Another reason why the Hamamatsu spectrum is used in simulations is because the unfiltered spectrum from the Thermo Scientific source may not be correct since pileup may be present when measuring the spectrum with the spectrometer. To prevent pileup, a collimator is required and that is currently being purchased for the laboratory. Therefore, it is difficult to say if the Thermo Scientific spectrum is accurate; whereas the Hamamatsu spectrums are measured by Hamamatsu and are more likely to be an accurate representation of the spectrums.

In this case, R_1 and R_2 are varied. Using the Hamamatsu source results in a quadratic trend between retrieved thickness and theoretical thickness for polystyrene, as seen in Figure 7.5, compared to the linear trend that is seen using the Thermo Scientific source. The quadratic expressions are tabulated in Table 7.6 and all result in an R-squared value of 0.9988. The only difference between the quadratic equations is the last coefficient which results in a difference on the order of $1x10^{-4}$, therefore the same expression can be used for each R_1 and R_2 value with a small error introduced.

Table 7.6: Linear expressions of polystyrene cylinders at different R_1 and R_2 values using the 60 kV L12531 Hamamatsy spectrum

R_1 (cm)	R_2 (cm)	Equation	R^2
8	8	y = -0.0205x^2+0.4984x+0.1022	0.9988
8	16	y = -0.0205x^2+0.4984x+0.1023	0.9988
15	15	y = -0.0205x^2+0.4984x+0.1024	0.9988

For the final three tests, metal cylinders were simulated and the thickness was retrieved. Generally, metals are good absorbers and conventional X-ray imaging can be used to pick up defects. Since the atomic number of most metals is much greater than 20 and their densities tend to be much higher than plastics, PCI may not be the best imaging technique

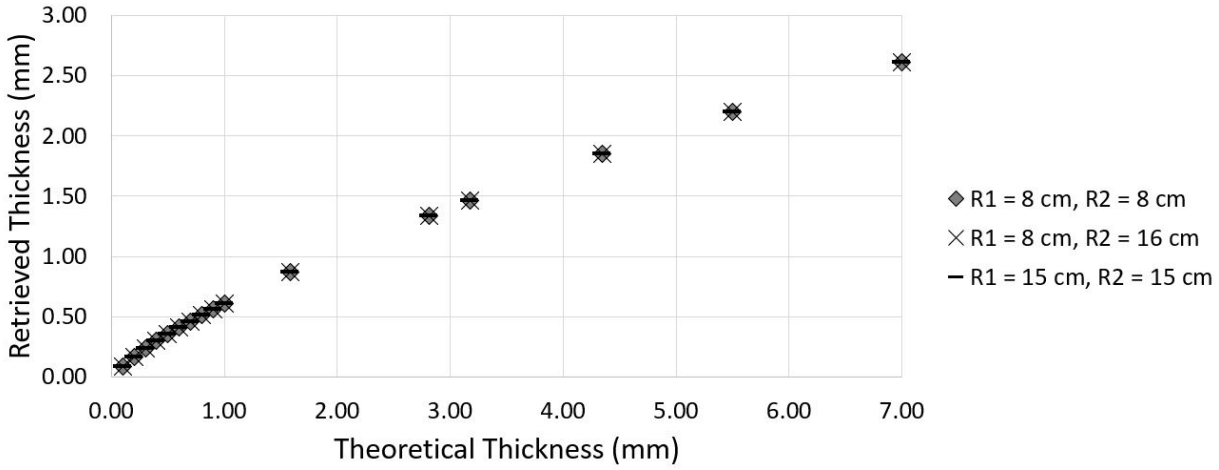

Figure 7.5: Retrieved thickness versus theoretical thickness of a polystyrene cylinder varying R_1 and R_2 using the 60 kV L12531 Hamamatsu spectrum

to find defects. Industries are interested in imaging metals to find small defects, therefore the final simulations are performed to see if thickness retrieval using Paganin's method is possible on higher atomic number samples. The first metal tested is aluminum. Aluminum is a soft, low-density, light-weight metal with a relatively low atomic number of 13. The first simulation performed on aluminum was using the 100 kV L12531 Hamamatsu spectrum at different R_2 values and the results are presented in Figure 7.6.

When the theoretical thickness of aluminum is set to 7 mm, the relative error is roughly 85%, therefore the properties of aluminum introduce a high relative error. The trend between the retrieved thickness and theoretical thickness is relatively quadratic with an R-squared value of 0.9869. The equations are expressed in Table 7.7. Again, the only difference between the two expressions at different R_2 values is the last coefficient, therefore either expression could be used to estimate the theoretical thickness given the retrieved thickness with relatively small error.

Table 7.7: Polynomial expressions of aluminum cylinders at different R_2 values using the 100 kV L12531 Hamamatsu spectrum

R_1 (cm)	R_2 (cm)	Equation	R^2
8	8	y = -0.0156x^2+0.2282x+0.1174	0.9869
8	16	y = -0.0156x^2+0.2281x+0.1175	0.9869

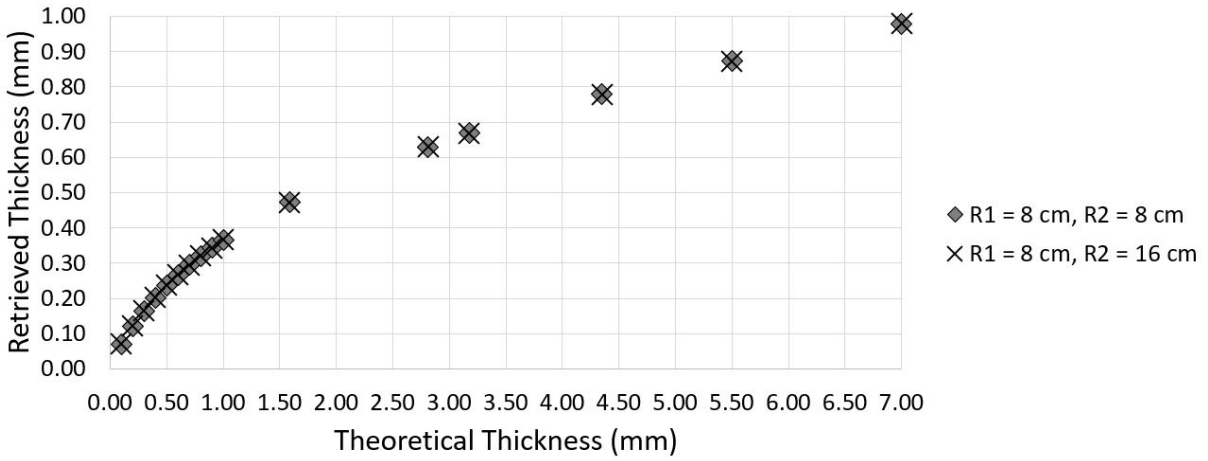

Figure 7.6: Retrieved thickness versus theoretical thickness of a aluminum cylinder varying R_1 and R_2 using the 100 kV L12531 Hamamatsu spectrum

Aluminum is simulated using the 60 kV 2 mm aluminum filtered Thermo Scientific spectrum to see if the results would improve compared to an unfiltered spectrum. Ideally, using a 100 kV 2 mm aluminum filtered Hamamatsu spectrum would give a better comparison to the unfiltered spectrum, but this spectrum is not currently available. For this reason, the 60 kV 2 mm aluminum filtered Thermo Scientific spectrum is used. Using this spectrum, the results improve. A 7 mm aluminum sample leads to a 29% relative error, which is far better than a relative error of 85% that was produced by the 100 kV unfiltered Hamamatsu spectrum. The trend between the retrieved thickness and theoretical thickness remains quadratic, as seen in Table 7.8. The R-squared value is 0.9999 for the two equations, therefore are good representations of the data. Like all the other cases, the two equations are similar with only the last coefficient varying.

Table 7.8: Polynomial expressions of aluminum cylinders at different R_2 values using the 60 kV 2 mm Al filtered Thermo Scientific spectrum

R_1 (cm)	R_2 (cm)	Equation	R^2
8	8	y = -0.0305x^2+0.9151x+0.0322	0.9999
8	16	y = -0.0305x^2+0.9151x+0.0322	0.9999

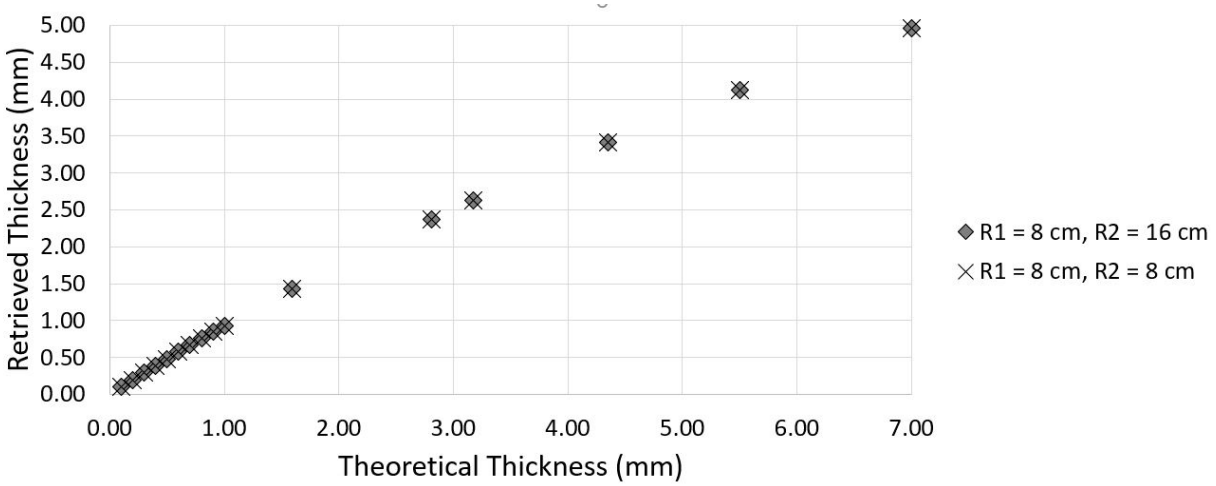

Figure 7.7: Retrieved thickness versus theoretical thickness of a aluminum cylinder varying R_1 and R_2 using the 60 kV 2 mm Al filtered Thermo Scientific spectrum

The final test performing thickness retrieval on a tungsten cylinder. Tungsten has a much higher density and atomic number than plastics. The atomic number of tungsten is 74 and the density is 19.3 g/cm^3, which makes it almost a magnitude more dense than most plastics. The results from the simulation using the 60 kV 2 mm aluminum filtered Thermo Scientific spectrum are presented in Figure 7.8. First, it can be observed that the results only go up to a theoretical thickness of 100 µm. This is because beyond this thickness, Paganin's method calculates complex numbers. This phase retrieval method, and many other phase retrieval methods for propagation-based PCI, are not suited for metals, high-density materials and atomic numbers greater than 20, which is why complex numbers are computed. The second observation is that the relative errors for the few thickness it could retrieve are high. For a theoretical thickness of 100 µm, the relative error is around 74%. From these results, it can be concluded that Paganin's method cannot retrieve the thickness of hard, dense metals like tungsten.

The results for Kevlar are found in Appendix B, Figures B.5 and B.6. The same quadratic trends can be observed in Table 7.9 for both the 60 kV and 100 kV L12531 Hamamatsu spectrum cases. The expressions vary between source potential, but remain similar for different R_2 values, as was seen with all the other materials described in this section. More analysis will be completed in section 7.2 on the effect of using different source potentials.

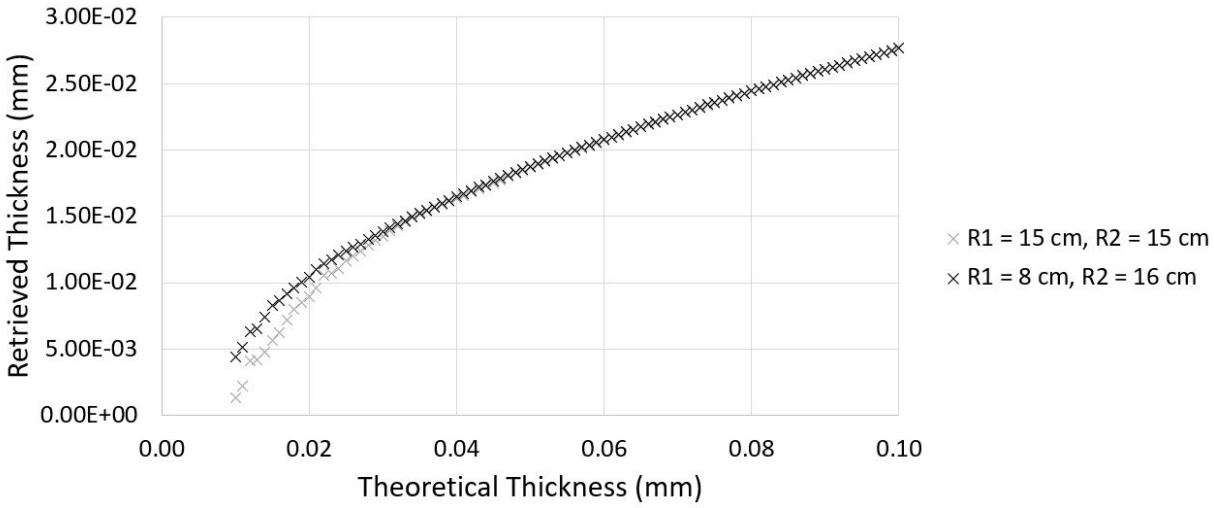

Figure 7.8: Retrieved thickness versus theoretical thickness of a tungsten cylinder varying R_1 and R_2 using the 60 kV 2 mm Al filtered Thermo Scientific spectrum

Table 7.9: Polynomial expressions of Kevlar cylinders using different source potentials with the Hamamatsu L12531 source and different R_2 values

Source Potential (kV)	R_1 (cm)	R_2 (cm)	Equation	R^2
60	8	8	$y = -0.0203x^2+0.4402x+0.0992$	0.9985
60	8	16	$y = -0.0203x^2+0.4402x+0.0993$	0.9985
100	8	8	$y = -0.0194x^2+0.4211x+0.1019$	0.9983
100	8	16	$y = -0.0194x^2+0.4212x+0.102$	0.9983

7.2 Effect of Spectrum on Paganin's Method

In this section, the effect of how accurately a spectrum needs to be calibrated will be discussed. Also, the effect of using a different source and using different source potentials will be examined.

The effect on how accurately the spectrum needs to be calibrated for Paganin's method to work is tested by simulating the PTFE object using the spectrum in Figure 6.1 (b) and shifting the spectrum to the higher energies by 0.204 keV to 1.84 keV to calculate the weighted averages for μ and δ used in Paganin's method. In effect, this means that the spectrum used to simulate the object is different from the one used to retrieve the thickness in the image. The results from these simulations are shown in Figure 7.9 for

different thicknesses of PTFE. From these results, it is observed that shifting the spectrum over by even a small amount can have an effect on the accuracy of Paganin's method in retrieving the correct thickness. As the spectrum used to calculate the weighted averages is shifted over, the relative error increases. This is expected since the spectrum used to simulate the image no longer matches the spectrum used to calculate the weighted averages for phase retrieval. Shifting the spectrum over by even 1 keV increases the relative error by just over 15 percent. The Amptek X-123 CdTe spectrometer is calibrated using an americium-241 gamma source where the spectrum is known, and the user outlines three characteristic peaks and defines the energies at which those peak occur. After the spectrometer is calibrated with the gamma source, it counts the number of photons from the X-ray source and uses the calibrated values from the gamma source to define the corresponding X-ray energies. Therefore, if this calibration is incorrect, the X-ray spectrum could be shifted by some value and not match up with the spectrum of X-ray energies that hit the a-Se CMOS detector when imaging. In effect, this can cause for an increase in relative error.

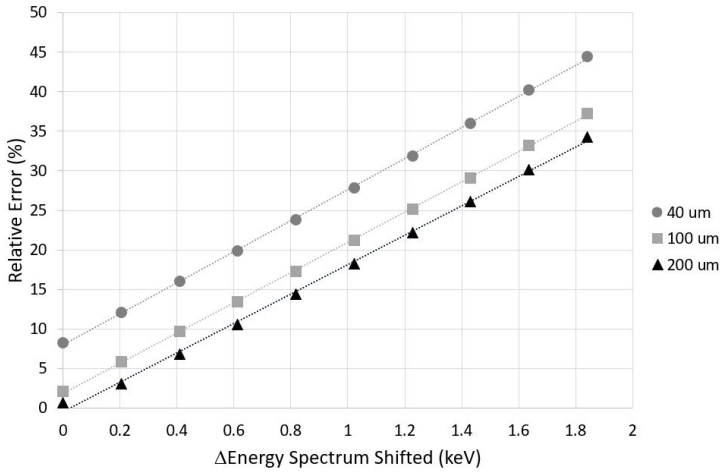

Figure 7.9: Relative error versus the change in energy that the spectrum is shifted over

The next simulations that are investigated are using the L12531 Hamamatsu source at $R_1 = 8$ cm, $R_2 = 16$ cm, PTFE cylinders and three different source potentials: 60 kV, 80 kV and 100 kV. The results are shown in Figure 7.10 and they show that varying the source potential does alter the resulting retrieved thickness. As can be seen in Table 7.10, each source potential has a different quadratic expression and their R-squared value ranges from 0.9944 to 0.9949. Because of this difference, this means that the same quadratic expression cannot be used for different source potentials. Thus, as seen in the previous

figures in section 7.1, the same quadratic expression can be used when the same source potential is used and R_1 or R_2 is varied, but a different quadratic expression is required if the source potential is changed.

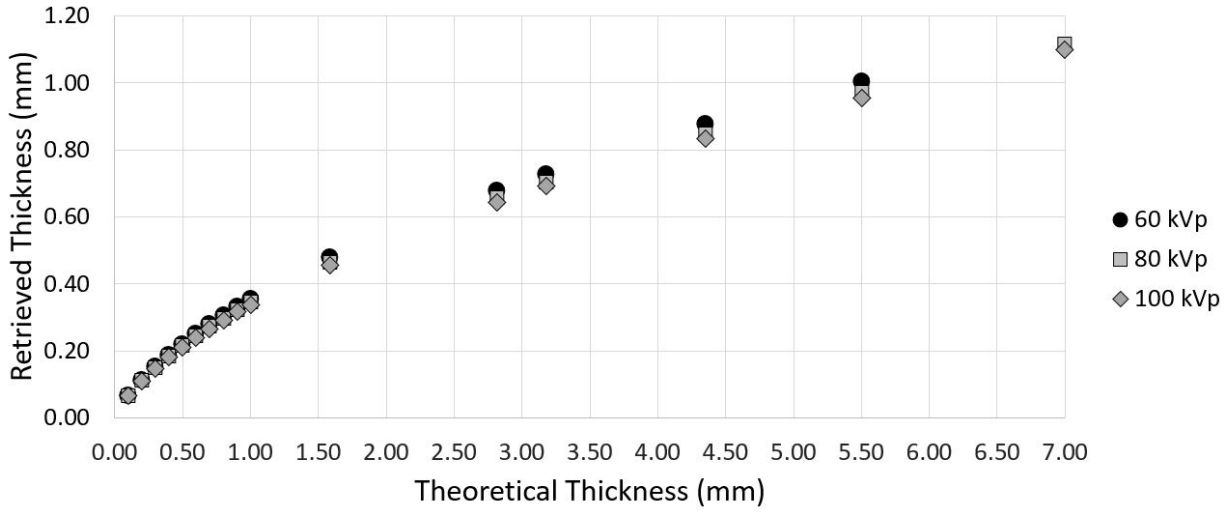

Figure 7.10: Retrieved thickness versus theoretical thickness of a PTFE cylinder varying source potential using a L12531 Hamamatsu source

Table 7.10: Polynomial expressions of PTFE cylinders at different source potentials using a L12531 Hamamatsu source

Source Potential (kV)	Equation	R^2
60	$y = -0.013x^2+0.2418x+0.0973$	0.9944
80	$y = -0.014x^2+0.2404x+0.0933$	0.9946
100	$y = -0.0136x^2+0.2357x+0.0912$	0.9949

Another cause of error that is seen in Figure 7.11 using a Kevlar cylinder as an example is that using different sources at the same source potential can cause a large difference between the retrieved thickness and measured thickness. Each source is used in separate simulations, therefore the same spectrum from a specified source is used to simulate the object and retrieve the image. The difference between the Thermo Scientific source spectrum at 60 kV and the Hamamatsu source spectrum at 60 kV is where the peaks occur

and the number of peaks present. This change in spectrum causes the Thermo Scientific source to have a relative error of around 13% for a measured thickness of 7 mm; whereas the L12531 Hamamatsu source has a relative error of 68%. The only difference between the two is the inputted spectrum used to create the final intensity image before phase retrieval. Overall, the Thermo Scientific source seems to produce better results than the Hamamatsu source according to this simulation. The one issue with the Thermo Scientific spectrum, as mentioned before in section 7.1, is that there is uncertainty in how accurate the spectrum is due to pileup caused by the number of photons hitting the spectrometer, and a collimator is required to eliminate this issue. At this time, a collimator is not available. From these results, it is obvious that the spectrum can affect the accuracy of retrieved thickness for thicker objects.

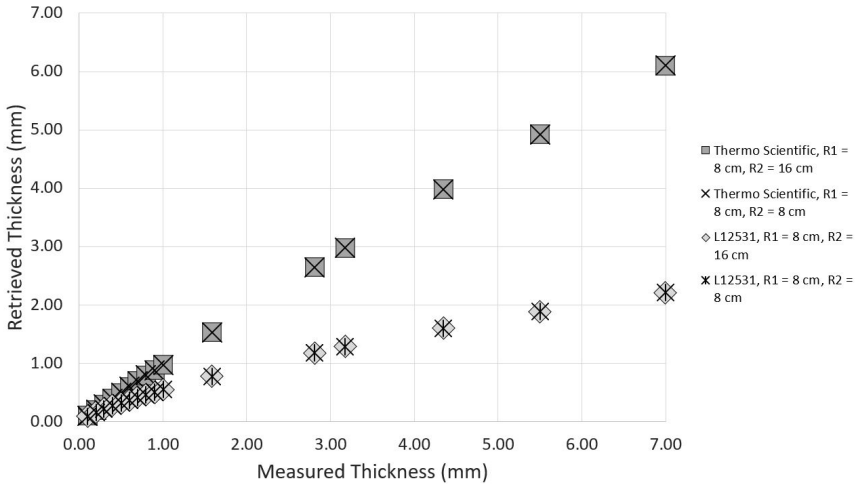

Figure 7.11: Retrieved thickness versus measured thickness of Kevlar while varying the R_1 and R_2 values, and the source

Thus, the spectrum needs to be well calibrated and if the source potential changes, a new spectrum and set of equations need to be used to find the true thickness of the material. Also, different sources can affect the error of the final thickness retrieved image.

7.3 Effect of Noise on Paganin's Method

As mentioned in section 4.4, noise plays a large role in X-ray imaging. For this reason, some simulations using polystyrene cylinders where noise is present were run using the spectrum

from Figure 5.1. The MATLAB code used to introduce noise is described in section 4.6. Other than adding noise, the same parameters that were used in Chapter 5 are used for these simulations. For all the simulations that occurred in Chapter 5, Paganin's method had a relative error that was always less than 10% for thicknesses between 20 µm to 400 µm.

In the presence of noise, Paganin's method performs well for the case of relative error versus thickness for thicknesses ranging between 20 µm to 400 µm, as seen in Figure 7.12. Overall, the relative error is generally below 10%, except for samples that are thinner than 100 µm. In this case it appears as though Paganin's method can handle added noise well. This is expected because the Fourier filter used in Paganin's method tends to increase the SNR.

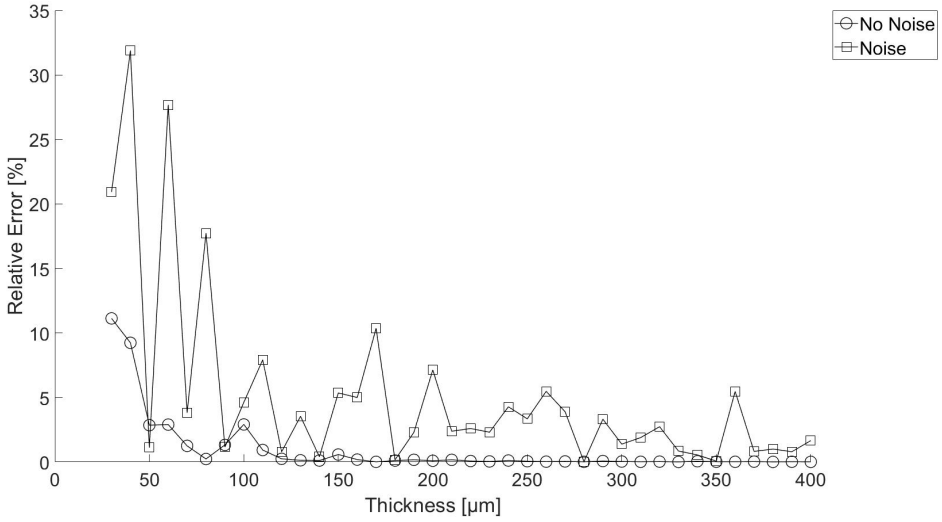

Figure 7.12: Relative error versus thickness of polystyrene in the presence of noise

In the case of changing the source potential and adding noise, the relative error for lower potential is much higher in Figure 7.13 compared to the no noise case seen in the same figure. Without noise, the relative error is less than 15% over all source potentials; whereas for low source potentials (20 kV to 60 kV) with noise present, the relative error generally exceeds 20%.

In the presence of noise, there is a lot more oscillation occurring with the relative error due to the fact that noise is random and changes in each image. This oscillation effect can be seen in all the figures in this section, but is especially obvious in Figures 7.14 and 7.15, where R_1 and R_2 are varied, respectively. This oscillation trend was observed with

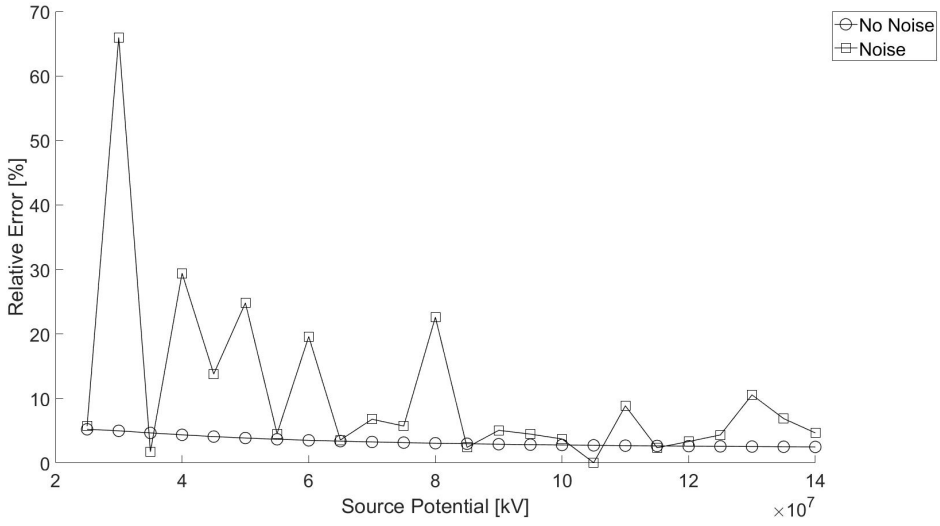

Figure 7.13: Relative error versus source potential of polystyrene in the presence of noise

all materials when varying R_1 and R_2 in Chapter 5, although the oscillations become more prominent with noise. In Figure 7.14, for the case where R_1 is varied, the relative error oscillates from close to zero up to around 23%.

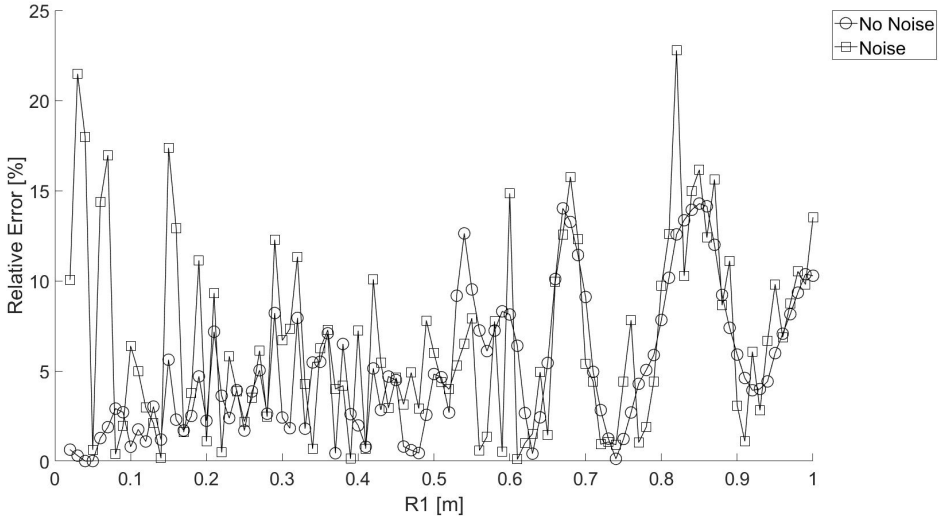

Figure 7.14: Relative error versus R_1 of polystyrene in the presence of noise

In Figure 7.15, for the case where R_2 is varied, the relative error generally oscillates between zero to around 20% and, occasionally, reaches as high as 44%.

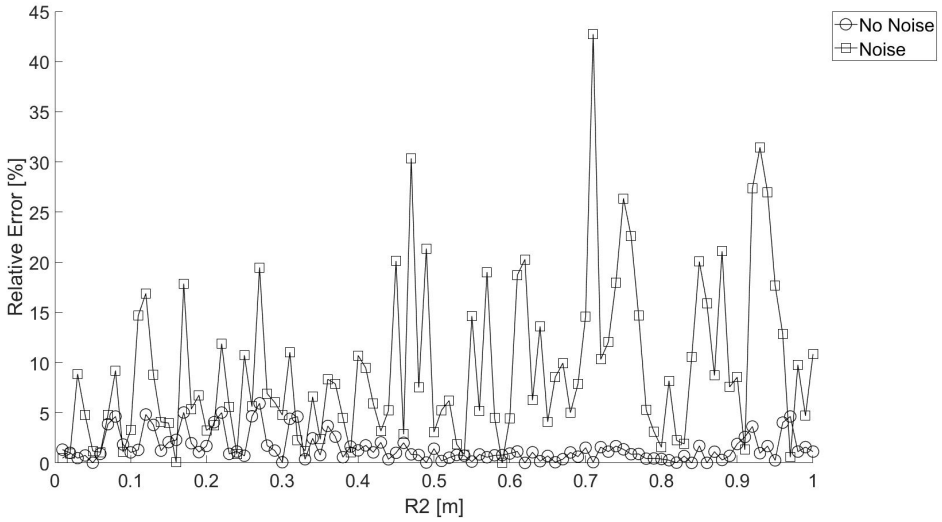

Figure 7.15: Relative error versus R_2 of polystyrene in the presence of noise

From these results, it can be concluded that even though Paganin's method seems to be decently resilient to noise and, in some cases, can increase the SNR, noise may cause the relative error to increase.

Chapter 8

Conclusions, Contributions and Future Work

8.1 Conclusions

Propagation-based PCI is the most promising PCI method to be used in medical and industrial applications due to its simple setup that only requires a detector and an X-ray source. It can be easily integrated into current X-ray systems that use a polychromatic source. Although it is the simplest setup, it has the drawback that its post-image processing is the most mathematically intense. All PCI images require a post-processing algorithm called phase retrieval. Phase retrieval is required because the detector only detects the intensity of X-rays, which contains both the attenuation and phase information. These intensity values are a qualitative representation of the object, and, to properly analyze an image, the phase information must be unwrapped from the data. For many of the methods that use complex optics, phase retrieval is simple and only requires an unwrapping of the 2π phase shifts. In propagation-based PCI, phase retrieval becomes a nonlinear inverse technique that is used to estimate the phase shift, thickness or electron density in an image. When phase retrieval is applied, it removes the edge enhancement from the image so that the boundaries of the object become well-defined and quantitative.

Most inverse problems, including phase retrieval, are ill-posed, which is caused by either solutions not existing or not being unique. Also, the solutions may be unstable with respect to small perturbations of input data. For propagation-based PCI, there exists two methods of phase retrieval that include iterative and non-iterative approaches. Many researchers have tried to linearize the equations by using the transport of intensity

equation and the contrast transfer function. In the end, there are seven well-known methods that have been derived: Paganin's method, Bronnikov method, Modified Bronnikov method, Arhatari TIE method, Arhatari CTF method, phase-attenuation duality method and attenuation-partition based algorithm. Each method is derived under different mathematical assumptions, but they all perform the same task of retrieving the phase in a phase-contrast image. All of these methods except for Arhatari's two methods have been derived under the assumption of a monochromatic source. Monochromatic sources tend to require a large facility and are expense, thus cannot be easily integrated into industrial or medical imaging. Polychromatic sources are already used in many imaging facilities, therefore making it easier to integrate PCI and are cheaper than a monochromatic source. For this reason, a phase retrieval method for polychromatic X-ray imaging is desirable. Many of the methods derived under the assumption of a monochromatic source can be easily altered to include a polychromatic source. These methods have been investigated by many groups under the assumption of a monochromatic source. In this thesis, they are extended to a polychromatic source, tested and analyzed under five cases for different materials, which are varying object thickness, source potential, source-to-object distance, object-to-detector distance and pixel size. Overall, Paganin's method performs with minimal relative error under each test case and is the best method investigated. Modified Bronnikov method and Arhatari TIE method perform almost as well as Paganin's method. The other four methods perform with relatively high relative error, with Bronnikov method performing by-far the worst. Further, it was discovered that APBA does not work for energies less than 60 keV as claimed in [21]. In the end, Paganin's method is chosen to be applied experimentally.

Paganin's method does not perform well experimentally with PTFE samples that have thicknesses greater than 0.7112 mm. The retrieved thicknesses of these objects have high relative errors when imaged using an unfiltered or filtered spectrum. The trends in the results retrieved by Paganin's method are found to be polynomial. There is no correlation found between energy and retrieving the correct thickness with each sample imaged. After reviewing the experimental data, it is clear that problems are arising in the system, which could be caused by the source, the object or the detector. Since it is difficult to distinguish where in the system the source of error is arising through experimentation, simulations where performed.

When the object thickness is greater than 100 µm, the relative error of the thickness retrieved by Paganin's method increases. The trend between retrieved thickness versus theoretical thickness of the objects is observed to be polynomial for many different types of materials using different spectrums. This is the same trend that was observed in the experimental results, but the equations were found to be different betweeen simulation and

experimental results. The equations are similar when imaging the same type of material at different source-to-object distances or object-to-detector distances, but they vary for different spectrums or source potentials. Generally, a filtered spectrum using 2 mm of aluminum gives the best results with the lowest relative error. Paganin's method is able to retrieve the thickness of a polystyrene object in simulation with relatively small error; whereas PTFE has a large relative error. This proves that what is considered sufficiently thin for one material may not apply to another material, and that phase retrieval is extremely material dependent. Paganin's method does not work on metals or dense materials, such as tungsten.

Also, the spectrum needs to be well calibrated, and, if the source potential changes, a new set of equations will need to be derived to calculate the true thickness of the object. Different sources can affect the error produced by Paganin's method. From the detector side, Paganin's method is resilient to noise and can increase the signal-to-noise ratio through Fourier filtering.

Overall, the high relative error in experiment is caused by PTFE not being considered a thin object past 400 µm. Also, another cause is that the spectrum needs to be properly characterized. These appear to be the largest factors that are causing the high relative error in experimentation.

8.2 Contributions

The contributions of this work in the development of the phase-contract X-ray imaging system includes:

- Analyzed the PSF of the 7.8 µm a-Se CMOS detector under optical light.
- Soldered and debugged the printed circuit board used for the detector.
- Improved the X-ray system by including various stages and safety components.
- Adapted some phase retrieval methods to work with a polychromatic X-ray spectrum.
- Compared phase retrieval methods under the polychromatic source condition.
- Applied phase retrieval to experimentally obtained polychromatic images and analyzed the sources of error in simulation.
- Constructed a micro-CT X-ray system and adapted existing reconstruction toolboxes to create the final CT image.

8.3 Future Work

A collimator should be used to measure the spectrum, and this new spectrum should be applied in the phase retrieval algorithm to observe if there is any improvement in the results of previously obtained data. Experimental investigation should be completed on various types of materials. In future work, filtering the spectrum to acquire images is advised and increasing the source-to-object distance to avoid backscattered X-rays from entering the object. Most of the methods investigated in this paper only apply to homogeneous objects, therefore finding a method that can be applied to a multi-material object is desired, such as one that utilizes two spectrums. The long term goal of this work is to apply the phase retrieval algorithm in micro-CT imaging, which will revolutionize industrial and medical applications. Also, applying phase retrieval to mammography to distinguish carcinoma from tissue and calcification is desired.

References

[1] A. Thomas and A. Banerjee, *The history of radiology*. OUP, 2013.

[2] T. J. Davis, D. Gao, T. E. Gureyev, A. W. Stevenson, and S. W. Wilkins, "Phase-contrast imaging of weakly absorbing materials using hard x-rays," *Nature*, vol. 373, p. 595, 1995.

[3] D. Paganin, *Coherent X-ray optics*. Oxford University Press on Demand, 2006.

[4] S. W. Wilkins, T. E. Gureyev, D. Gao, A. Pogany, and A. W. Stevenson, "Phase-contrast imaging using polychromatic hard x-rays," *Letters to Nature*, vol. 384, pp. 335–338, 1996.

[5] U. Bonse and M. Hart, "An x-ray interferometer," *Appl. Phys. Lett.*, vol. 6, no. 155, p. 155, 1965.

[6] ——, "Principles and design of laue-case x-ray interferometers," *Physik*, vol. 188, no. 2, pp. 154–164, 1965.

[7] A. Olivo and R. Speller, "A coded-aperture technique allowing x-ray phase contrast imaging with conventional sources," *Applied Physics Letters*, vol. 91, no. 074106, pp. 1–3, 2007.

[8] ——, "Modelling of a novel x-ray phase contrast imaging technique based on coded apertures," *Physics in Medicine and Biology*, vol. 52, no. 22, p. 6555, 2007.

[9] X. Wu and H. Liu, "Phase-space evolution of x-ray coherence in phase-sensitive imaging," *Applied Optics*, vol. 47, no. 22, pp. 44–52, 2008.

[10] A. Snigirev, I. Snigireva, V. Kohn, S. Kuznetsov, and I. Schelokov, "On the possibilities of x-ray phase contrast microimaging by coherent high-energy synchrotron radiation," *Review of scientific instruments*, vol. 66, no. 12, pp. 5486–5492, 1995.

[11] P. Cloetens, R. Barrett, J. Baruchel, J. Guigay, and M. schlenker, "Phase objects in synchrotron radiation hard x-ray imaging," *Journal of Physics D: Applied Physics*, vol. 29, pp. 133–146, 1996.

[12] B. Arhatari, K. Hannah, E. Balaur, and A. Peele, "Phase imaging using a polychromatic x-ray laboratory source," *Optical Society of America*, vol. 16, no. 24, pp. 19 950–19 956, 2008.

[13] M. B. Luu, B. D. Arhatari, C. Q. Tran, and et al., "Quantitative phase imaging with polychromatic x-ray sources," *Optics Express*, vol. 19, no. 9, pp. 8127–8134, 2011.

[14] T. Tuohimaa, M. Otendal, and H. Hertz, "Phase-contrast x-ray imaging with a liquid-metal-jet anode microfocus source," *Applied Physics Letters*, vol. 91, no. 074104, pp. 1–3, 2007.

[15] A. Burvall, P. Takman, D. Larsson, and H. Hertz, "Phase retrieval in x-ray phase-contrast imaging suitable for tomography," *Optics Express*, vol. 19, no. 11, pp. 10 359–10 376, 2011.

[16] B. Yu, L. Weber, and e. a. A Pacureanu, "Phase retrieval in 3d x-ray magnified phase nano ct: Imaging bone tissue at the nanoscale," *ISBI*, pp. 56–59, 2017.

[17] T. Gureyev, A. Pogany, D. Paganin, and S. Wilkins, "Linear algorithms for phase retrieval in the fresnel region," *Optics Communications*, vol. 231, no. 1-6, pp. 53–70, 2004.

[18] D. Paganin, S. C. Mayo, T. E. Gureyev, P. R. Miller, and S. W. Wilkins, "Simultaneous phase and amplitude extraction from a single defocused image of a homogeneous object," *Journal of Microscopy*, vol. 206, no. 1, pp. 33–40, 2002.

[19] A. V. Bronnikov, "Reconstruction formulas in phase-contrast tomography," *Optics Communications*, vol. 171, no. 4-6, pp. 239–244, 1999.

[20] X. Wu, H. Liu, and A. Yan, "X-ray phase-attenuation duality and phase retrieval," *Optical Society of America*, vol. 30, no. 4, pp. 379–381, 2005.

[21] A. Yan, H. Liu, and X. Wu, "An attenuation-partition based iterative phase retrieval algorithm for in-line phase-contrast imaging," *Optics Express*, vol. 16, no. 17, pp. 13 330–13 341, 2008.

[22] A. Yan, X. Wu, and H. Liu, "A robust general phase retrieval method for medical applications," *MASR*, vol. 8, no. 5, pp. 1–12, 2012.

[23] A. Groso, A. Abela, and M. Stampanoni, "Implementation of a fast method for high resolution phase contrast tomography," *Optics Express*, vol. 14, no. 18, pp. 8103–8110, 2006.

[24] R. Fitzgerald, "Phase-sensitive x-ray imaging," *Phys. Today*, vol. 53, no. 7, pp. 23–26, 2000.

[25] J. Als-Nielsen and D. McMorrow, *Elements of modern X-ray physics*. John Wiley and Sons, 2011.

[26] X. Wu and H. Liu, "A new theory of phase contrast x-ray imaging based on wigner distributions," *Medical physics*, vol. 31, no. 9, pp. 2378–2384, 2004.

[27] P. Suortti, J. Keyrilainen, and W. Thomlinson, "Analyser-based x-ray imaging for biomedical research," *J. Phys. D: Appl. Phys.*, vol. 46, no. 494002, pp. 1–25, 2013.

[28] W. Zhou, K. Majidi, and J. G. Brankov, "Analyzer-based phase-contrast imaging system using a micro focus x-ray source," *Rev. Sci. Instrum.*, vol. 85, no. 8, pp. 1–8, 2014.

[29] P. Russo, Ed., *Handbook of X-ray Imaging: Physics and Technology*. CRC Press, 2018.

[30] D. C. Ghiglia and M. D. Pritt, *Two-dimensional phase unwrapping: theory, algorithms, and software*. Wiley, 1998.

[31] B. L. Sprague, R. E. Gangnon, V. Burt, and et al., "Prevalence of mammographically dense breasts in the united states," *JNCI*, vol. 106, no. 10, pp. 1–6, 2014.

[32] N. A. Dyson, *X-rays in Atomic and Nuclear Physics*. Press Syndicate of the University of Cambridge, 1973.

[33] N. I. of Standards and Technology. X-ray mass attenuation coefficients. [Online]. Available: https://www.nist.gov/pml/x-ray-mass-attenuation-coefficients

[34] ——. X-ray form factor, attenuation, and scattering tables. [Online]. Available: https://physics.nist.gov/PhysRefData/FFast/html/form.html

[35] X. Wu and H. Liu, "A general theoretical formalism for x-ray phase contrast imaging," *Journal of X-ray Science and Technology*, vol. 11, no. 1, pp. 33–42, 2003.

[36] J. Beutel, H. L. Kundel, and R. L. V. Metter, Eds., *Handbook of Medical Imaging: Volume 1. Physics and Psychophysics.* SPIE, 2000.

[37] W. S. Boyle and G. Smith, "Charge-coupled semiconductor devices," *Bell SYstem Techenics of Journal*, vol. 49, no. 4, pp. 587–593, 1970.

[38] M. Bigas, E. Cabruja, J. Forest, and J. Salvi, "Review of cmos image sensors," *Microelectronics Journal*, vol. 37, no. 5, pp. 433–451, 2006.

[39] R. P. Millane, "Phase retrieval in crystallography and optics," *J. Opt. Soc. Am. A*, vol. 7, no. 3, pp. 394–411, 1990.

[40] T. E. Gureyev, Y. I. Nesterets, and D. M. Paganin, "Monomorphous decomposition method and its application for phase retrieval and phase-contrast tomography," *Physical Review A*, vol. 92, no. 053860, pp. 1–10, 2015.

[41] M. R. Teague, "Deterministic phase retrieval: a green's function solution," *J. Opt. Soc. Am.*, vol. 73, no. 11, pp. 1434–1441, 1983.

[42] T. E. Gureyev, Y. I. Nesterets, A. W. Stevenson, and et al., "Some simple rules for contrast, signal-to-noise and resolution in in-line x-ray phase contrast imaging," *Optics Express*, vol. 16, no. 5, pp. 3223–3241, 2008.

[43] C. Zuo, Q. Chen, and A. Asundi, "Transport of intensity equation: a new approach to phase and light field," *Proceedings of SPIE*, vol. 9271, no. 92710H, pp. 1–16, 2014.

[44] L. D. Turner, B. B. Dhal, J. P. Hayes, and et al, "X-ray phase imaging: Demonstrastion of extended conditions with homogeneous objects," *Optics Express*, vol. 12, no. 13, pp. 2960–2965, 2004.

[45] M. Bartels, "Cone-beam x-ray phase contrast tomography of biological samples," *Gottingen series in X-ray physics*, vol. 13, pp. 21–22, 2013.

[46] M. A. Beltran, D. M. Paganin, K. Uesugi, and M. J. Kitchen, "2d and 3d x-ray phase retrieval of multi-material objects using a single defocus distance," *Optics Express*, vol. 18, no. 7, pp. 6423–6436, 2010.

[47] J. Wenz, S. Schleede, K. Khrennikov, and et al., "Quantitative x-ray phase-contrast microtomography from a compact laser-driven betatron source," *Physik*, vol. 6, no. 7568, pp. 1–6, 2015.

[48] X. Wu and H. Liu, "X-ray cone-beam phase tomography formulas based on phase-attenuation duality," *Optics Express*, vol. 13, no. 16, pp. 6000–6014, 2005.

[49] A. Yan, X. Wu, and H. Liu, "Performance analysis of the attenuation-partition based iterative phase retrieval algorithm for in-line phase contrast imaging," *Optics Express*, vol. 18, no. 15, pp. 16 074–16 089, 2010.

[50] J. H. Siewerdsen, A. M. Waese, D. J. Moseley, S. Richard, and D. A. Jaffray, "Spektr: A computational tool for x-ray spectral analysis and imaging system optimization," *Med. Phys.*, vol. 31, no. 11, pp. 3057–3067, 2004.

[51] J. M. Boone and J. A. Seibert, "An accurate method for computer-generating tungsten anode x-ray spectra from 30 to 140 kv," *Med Phys*, vol. 24, no. 11, pp. 1661–1670, 1997.

APPENDICES

Appendix A

Phase Retrieval Comparison Results

A.1 Polystyrene Results

A.1.1 With Bronnikov's Method

Cylinder

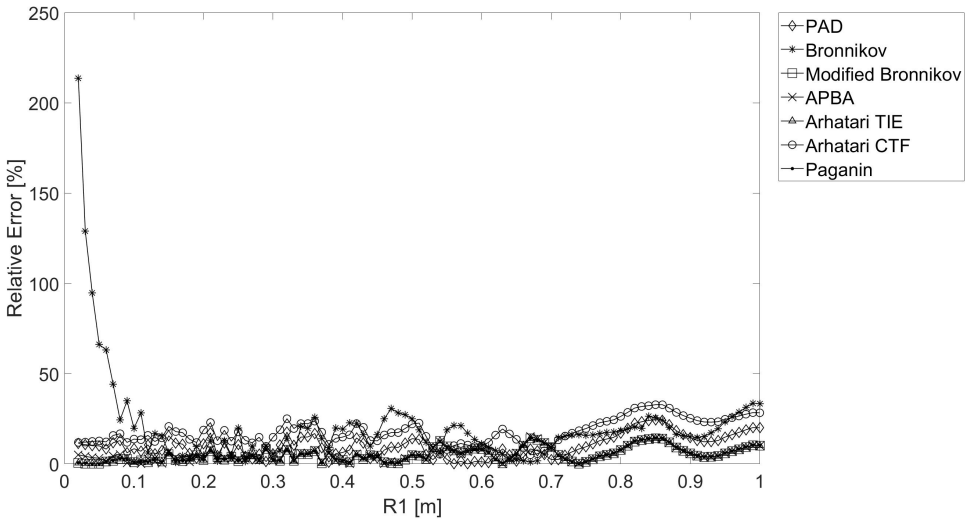

Figure A.1: Relative error versus R_1 for a polystyrene cylinder retrieved by different phase retrieval methods

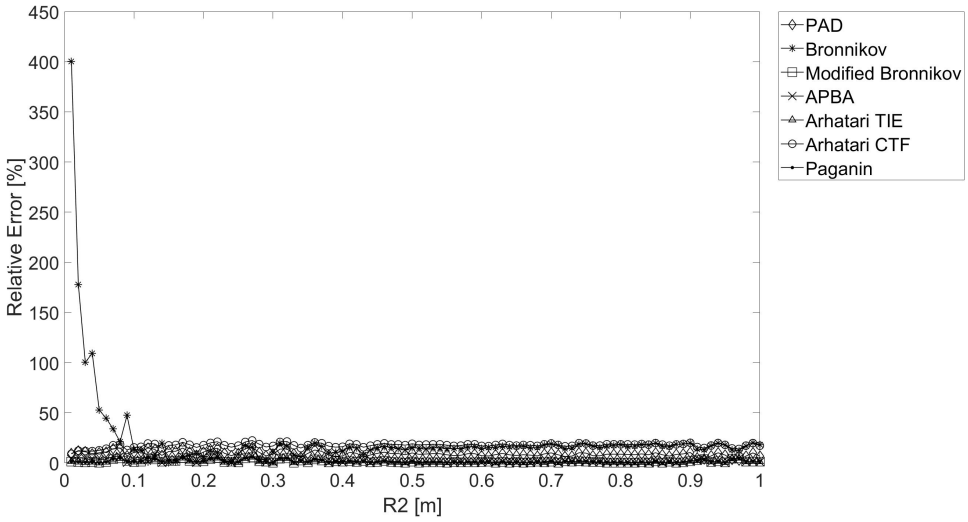

Figure A.2: Relative error versus R_2 with $R_1 = 16$ cm for a polystyrene cylinder retrieved by different phase retrieval methods

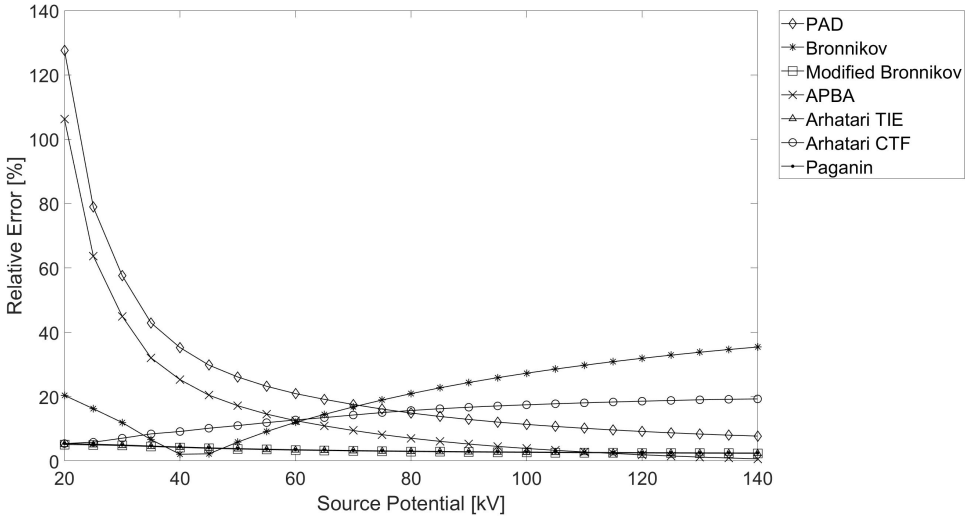

Figure A.3: Relative error versus source potential for a polystyrene cylinder retrieved by different phase retrieval methods

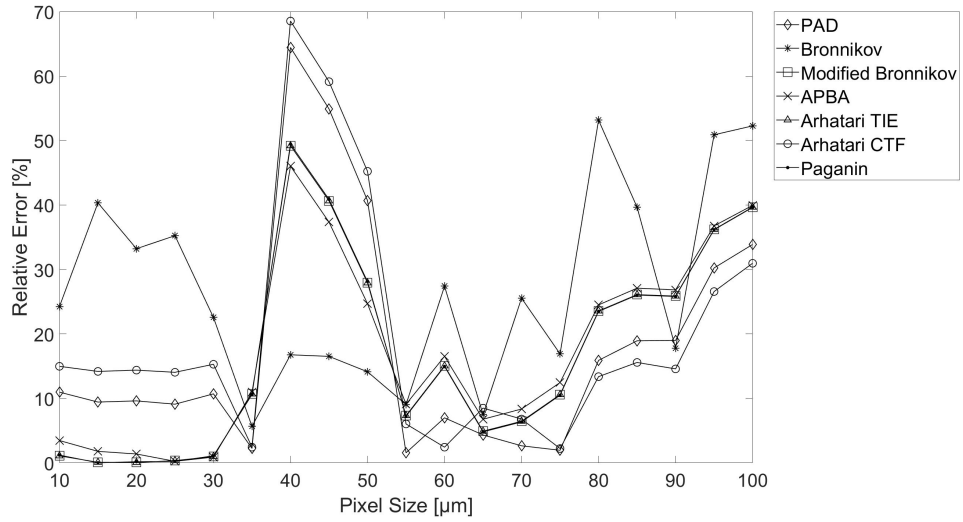

Figure A.4: Relative error versus pixel size for a polystyrene cylinder retrieved by different phase retrieval methods

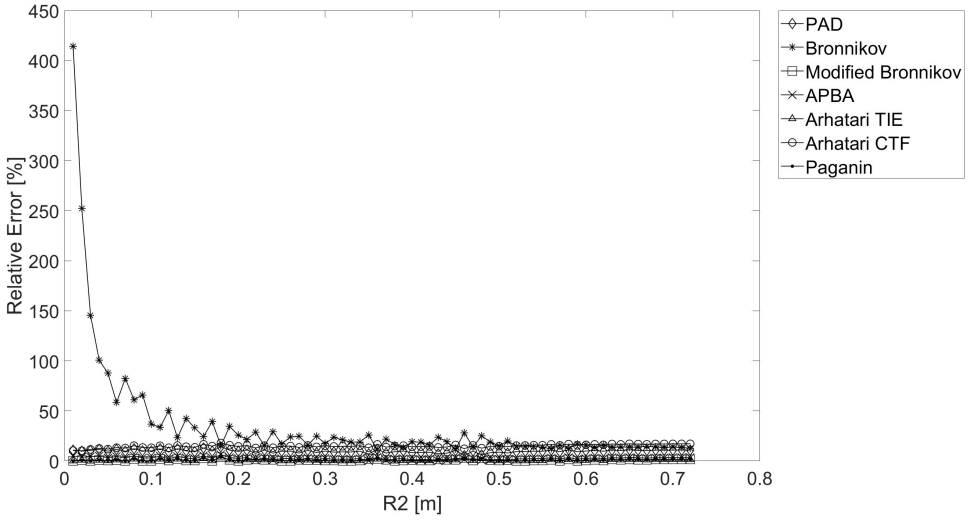

Figure A.5: Relative error versus R_2 with $R_1 = 8$ cm for a polystyrene cylinder retrieved by different phase retrieval methods

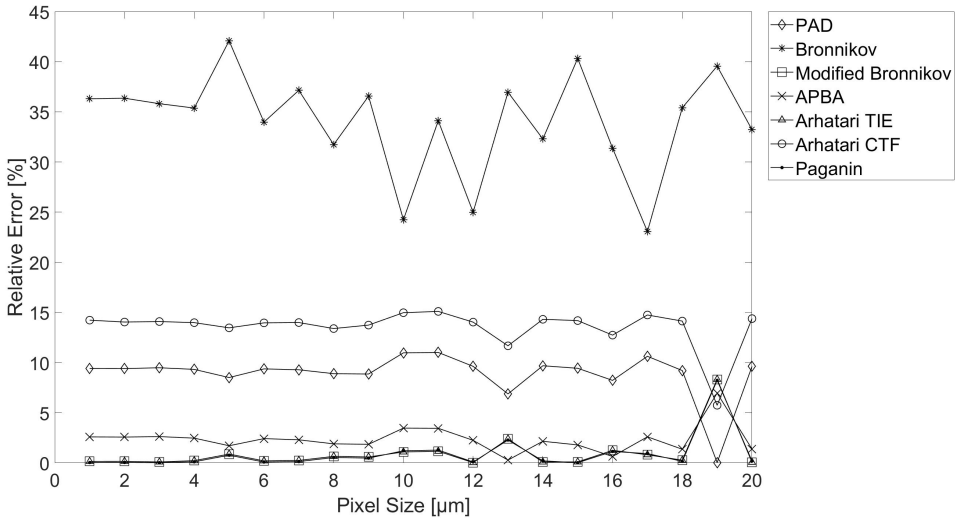

Figure A.6: Relative error versus pixel size for a polystyrene cylinder retrieved by different phase retrieval methods

Sphere

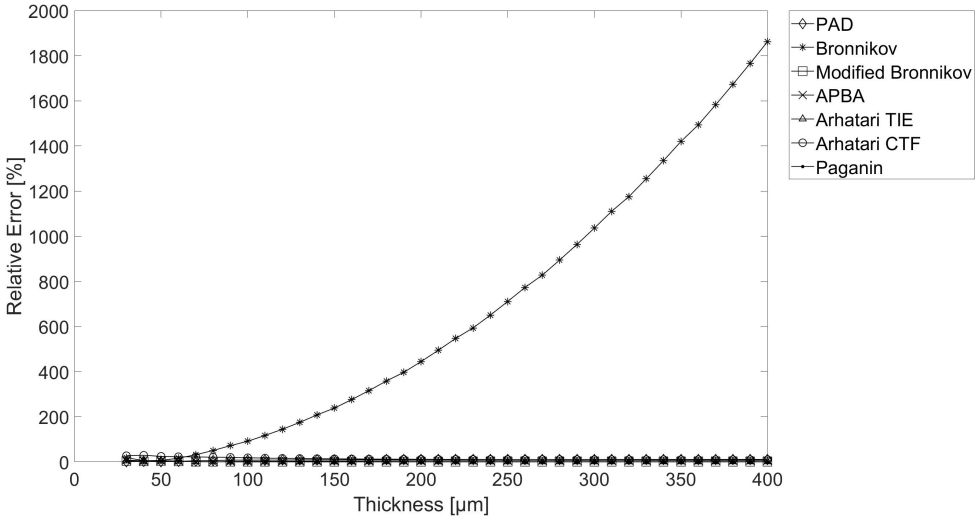

Figure A.7: Relative error versus thickness for a polystyrene sphere retrieved by different phase retrieval methods

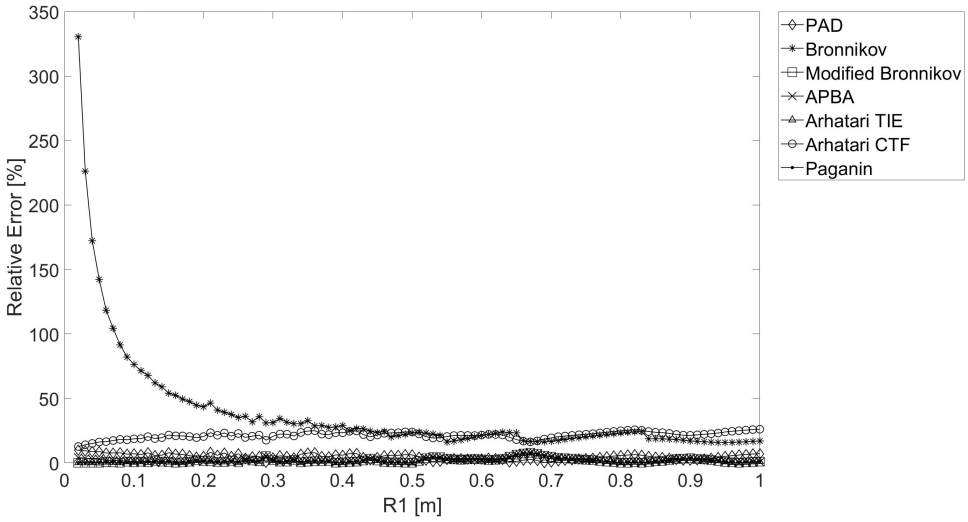

Figure A.8: Relative error versus R_1 for a polystyrene sphere retrieved by different phase retrieval methods

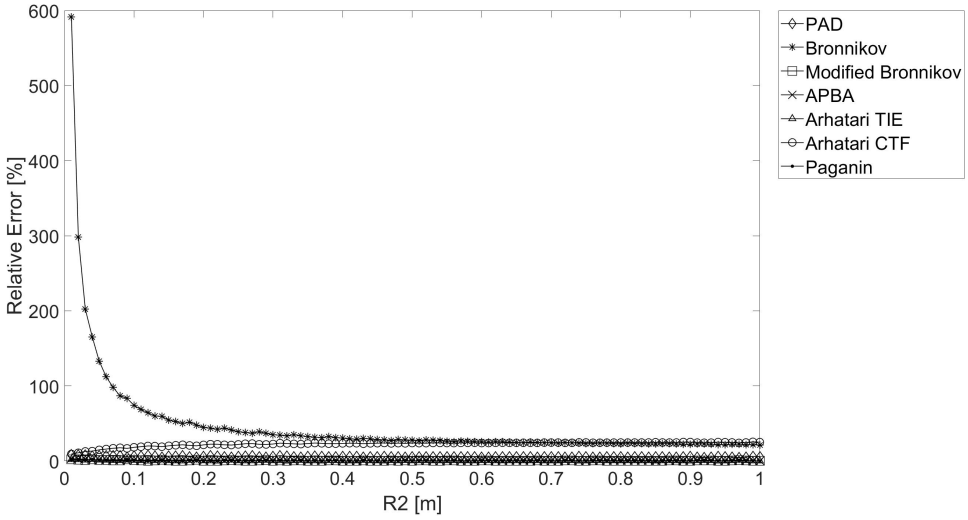

Figure A.9: Relative error versus R_2 with $R_1 = 16$ cm for a polystyrene sphere retrieved by different phase retrieval methods

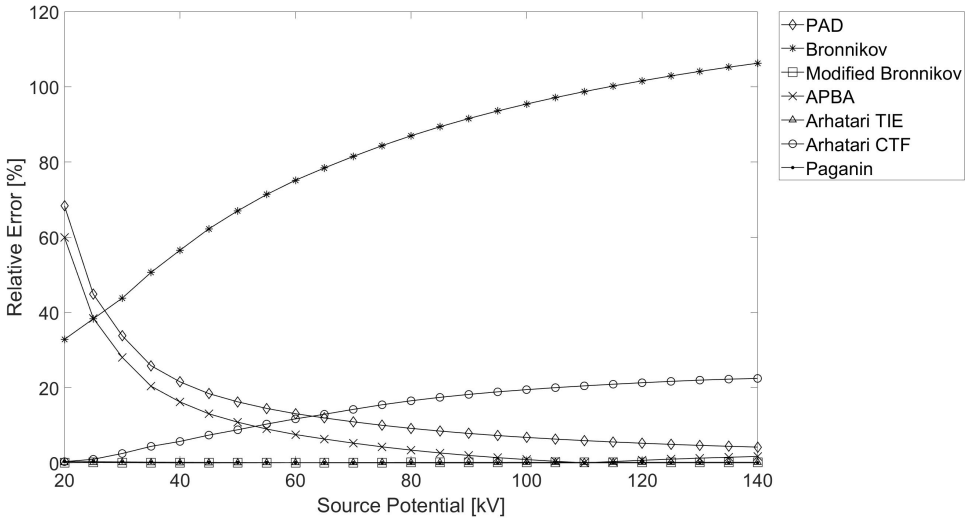

Figure A.10: Relative error versus source potential for a polystyrene sphere retrieved by different phase retrieval methods

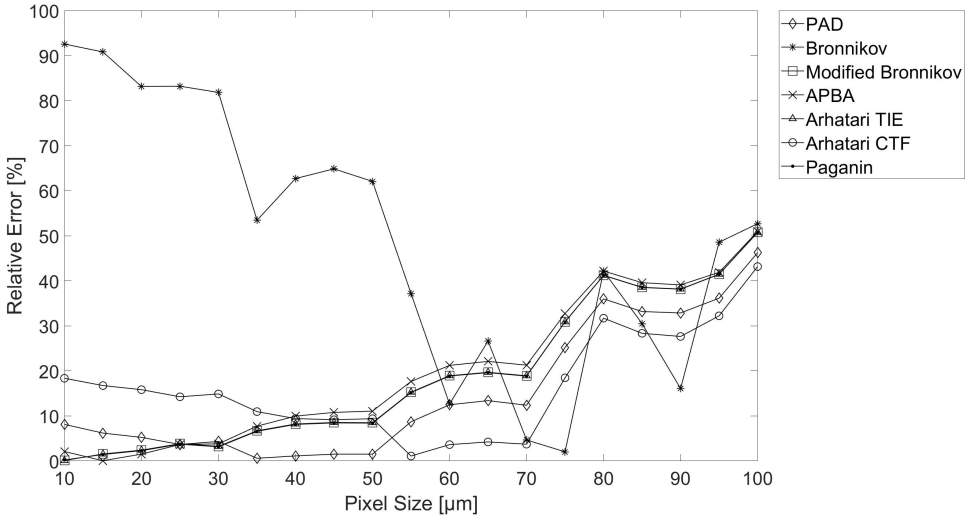

Figure A.11: Relative error versus pixel size for a polystyrene sphere retrieved by different phase retrieval methods

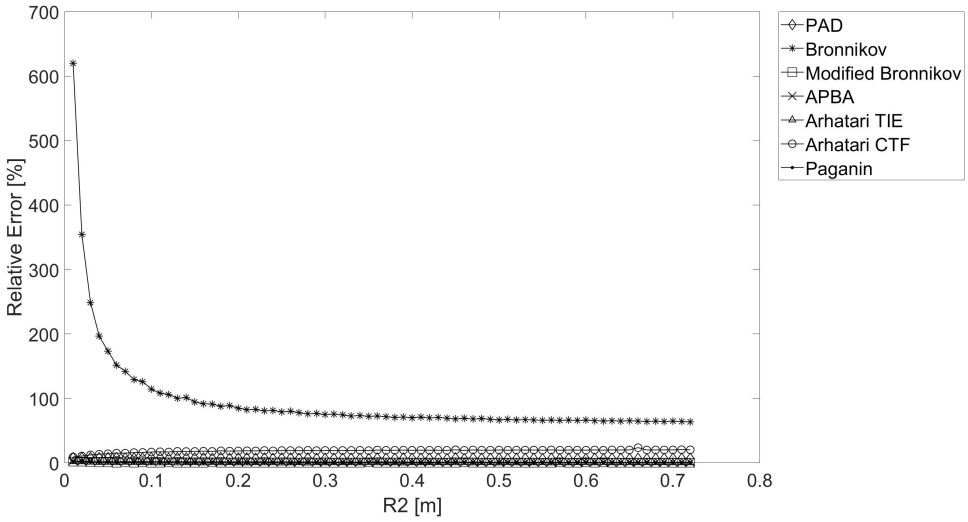

Figure A.12: Relative error versus R_2 with $R_1 = 8$ cm for a polystyrene sphere retrieved by different phase retrieval methods

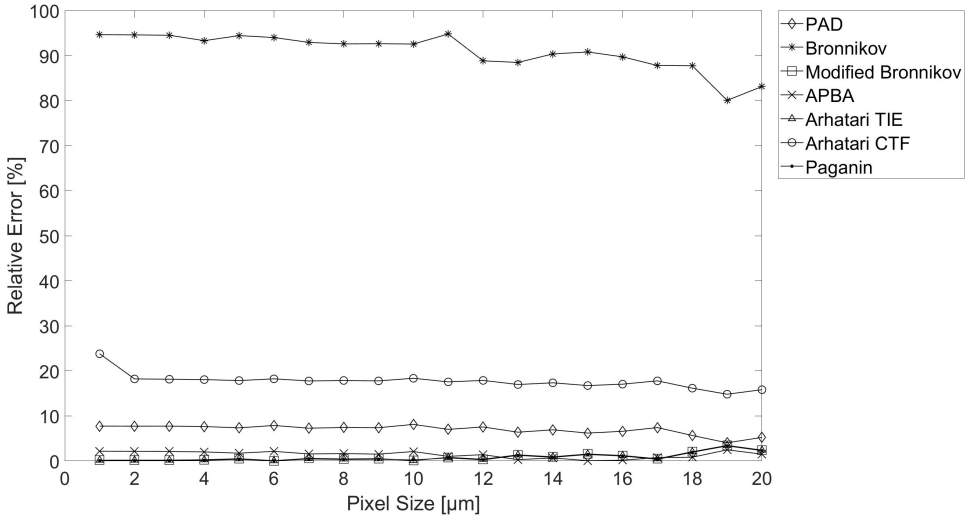

Figure A.13: Relative error versus pixel size for a polystyrene sphere retrieved by different phase retrieval methods

A.1.2 Without Bronnikov's Method

Cylinder

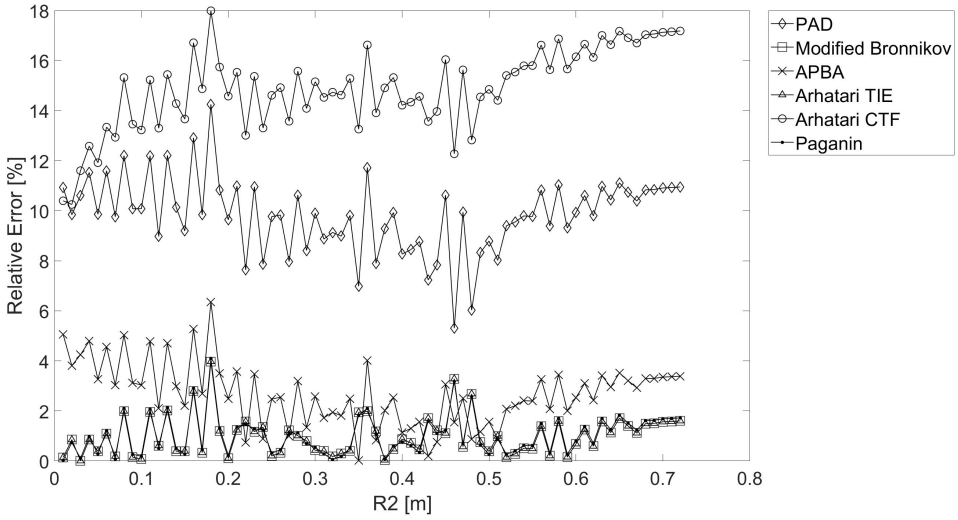

Figure A.14: Relative error versus R_2 with $R_1 = 8$ cm for a polystyrene cylinder retrieved by different phase retrieval methods

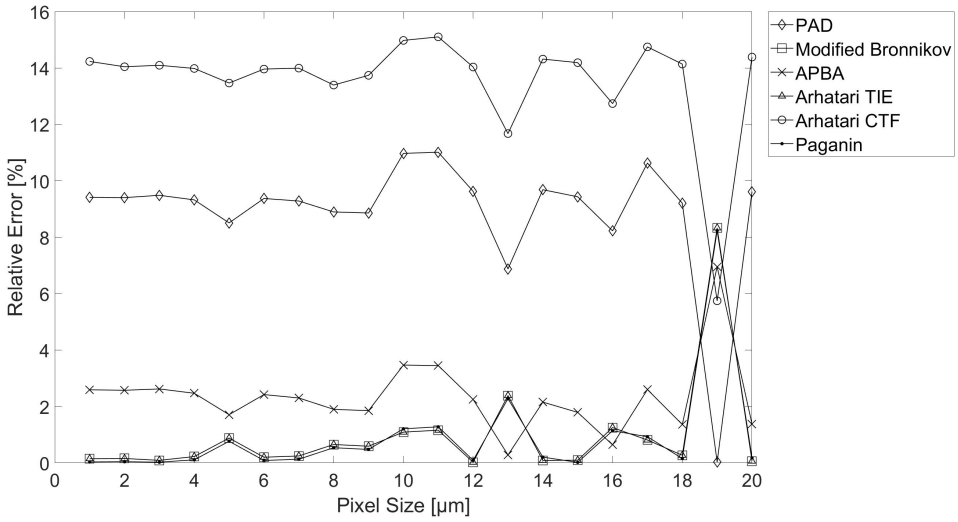

Figure A.15: Relative error versus pixel size for a polystyrene cylinder retrieved by different phase retrieval methods

Sphere

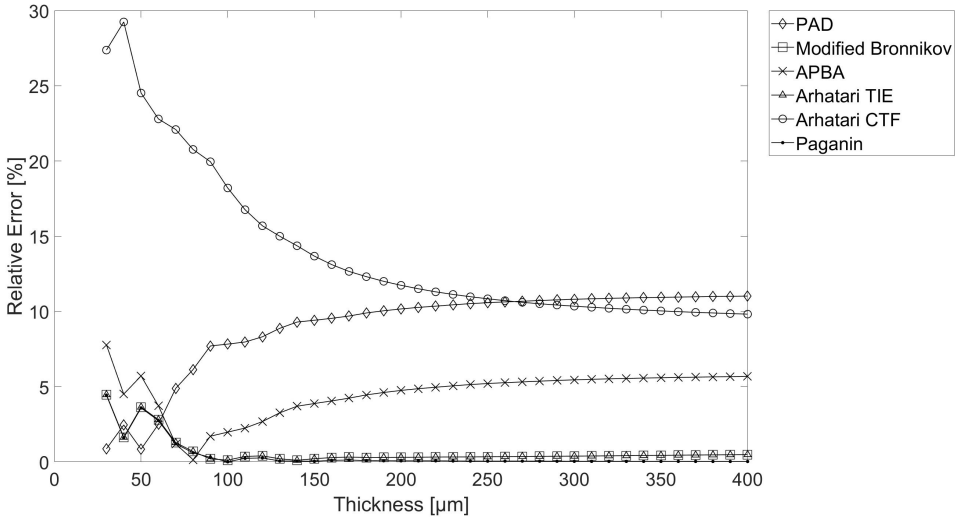

Figure A.16: Relative error versus thickness for a polystyrene sphere retrieved by different phase retrieval methods

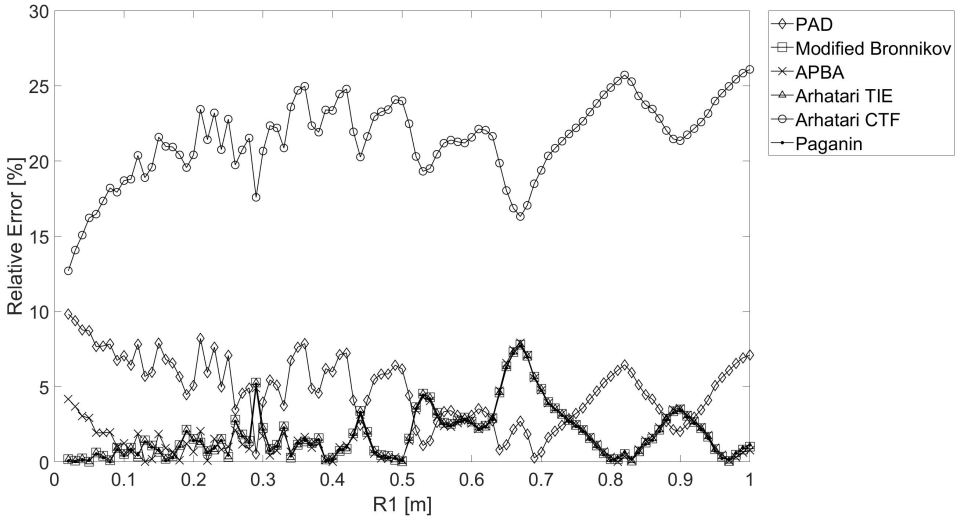

Figure A.17: Relative error versus R_1 for a polystyrene sphere retrieved by different phase retrieval methods

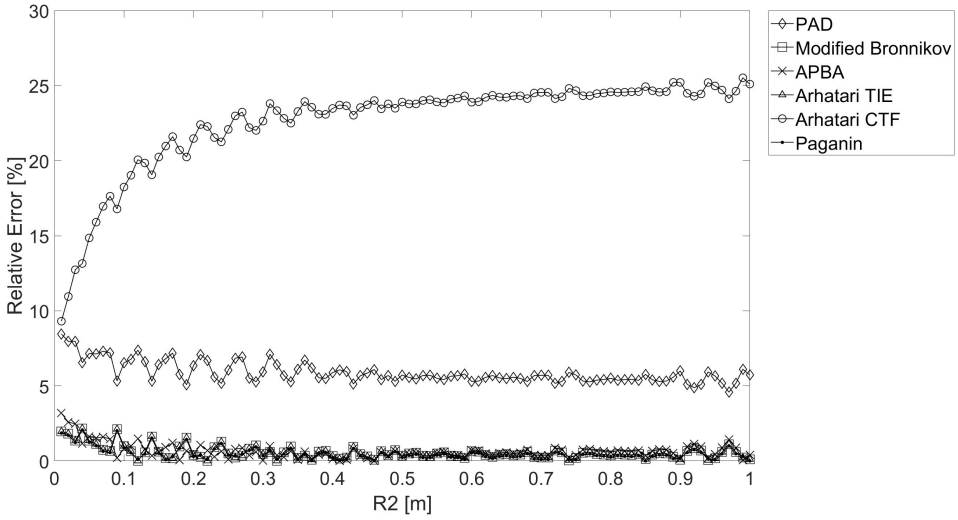

Figure A.18: Relative error versus R_2 with $R_1 = 16$ cm for a polystyrene sphere retrieved by different phase retrieval methods

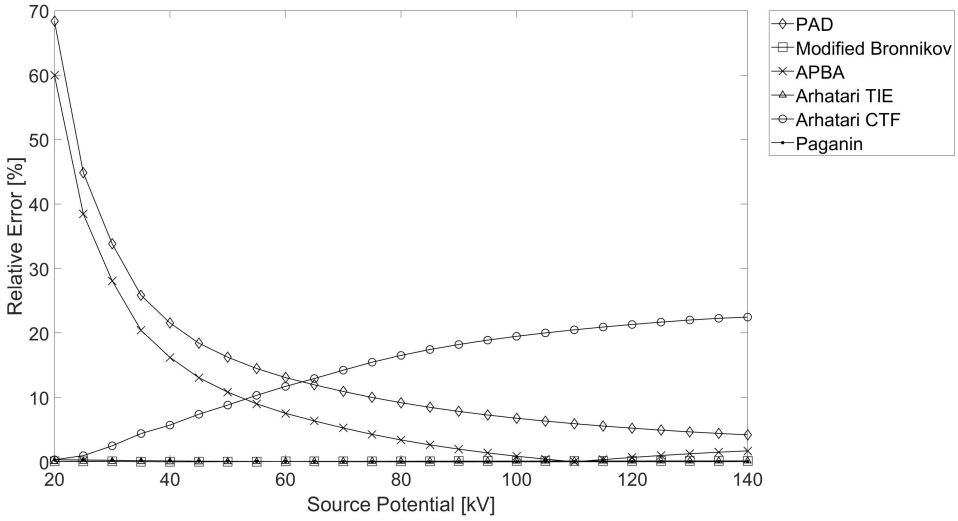

Figure A.19: Relative error versus source potential for a polystyrene sphere retrieved by different phase retrieval methods

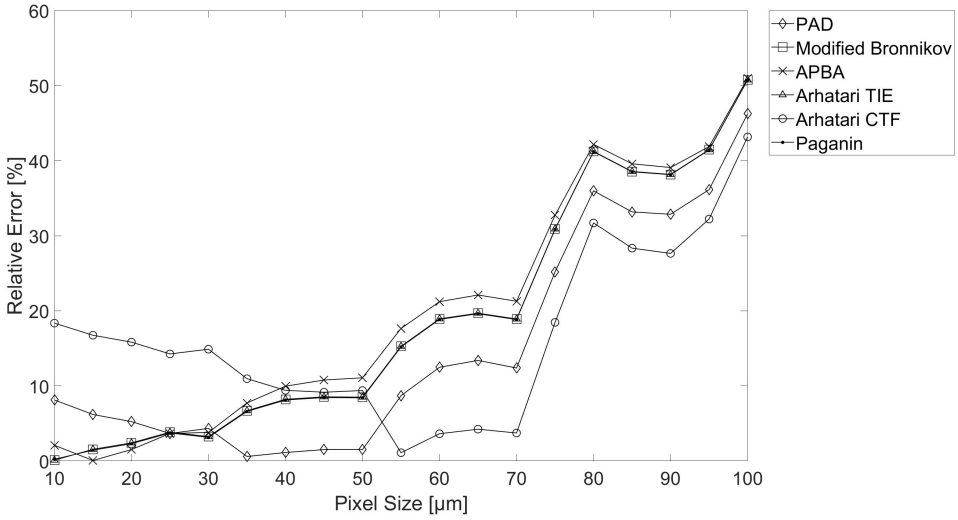

Figure A.20: Relative error versus pixel size for a polystyrene sphere retrieved by different phase retrieval methods

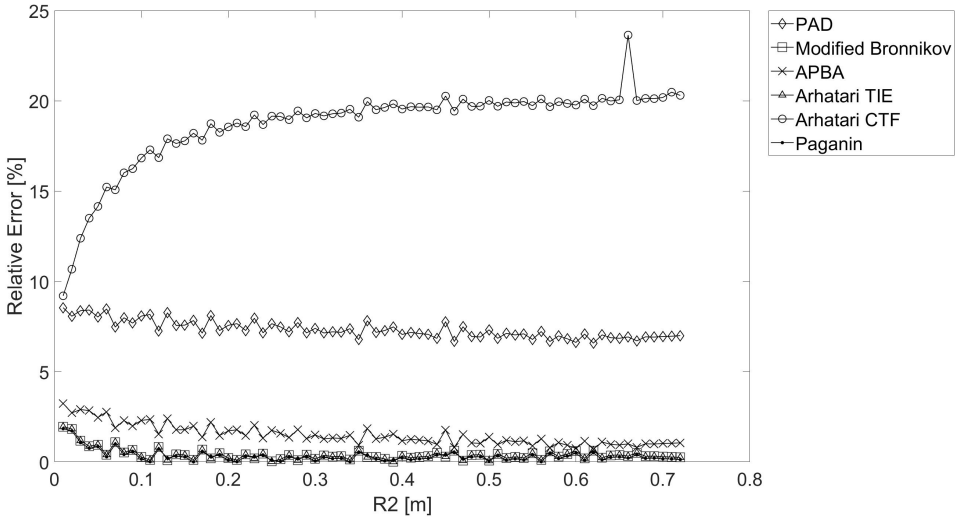

Figure A.21: Relative error versus R_2 with $R_1 = 8$ cm for a polystyrene sphere retrieved by different phase retrieval methods

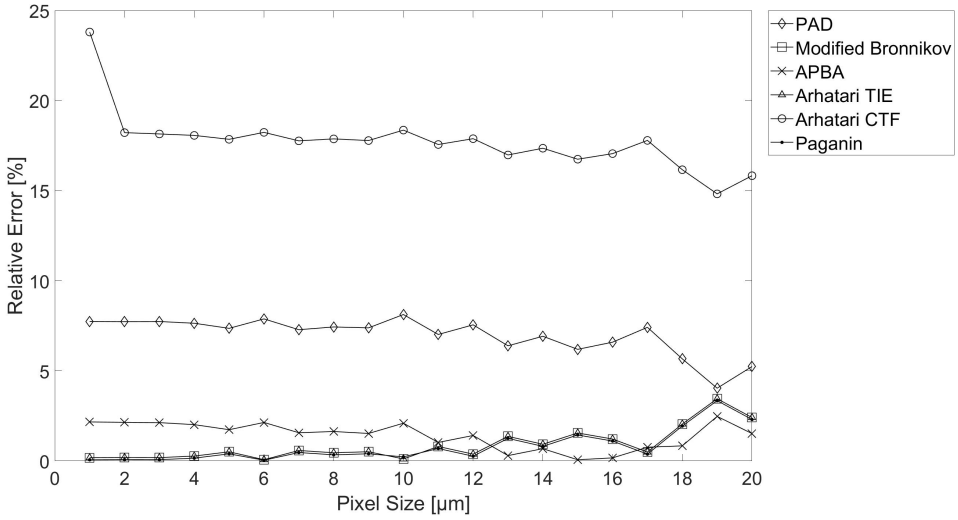

Figure A.22: Relative error versus pixel size for a polystyrene sphere retrieved by different phase retrieval methods

A.2 Kapton Results

A.2.1 With Bronnikov's Method

Cylinder

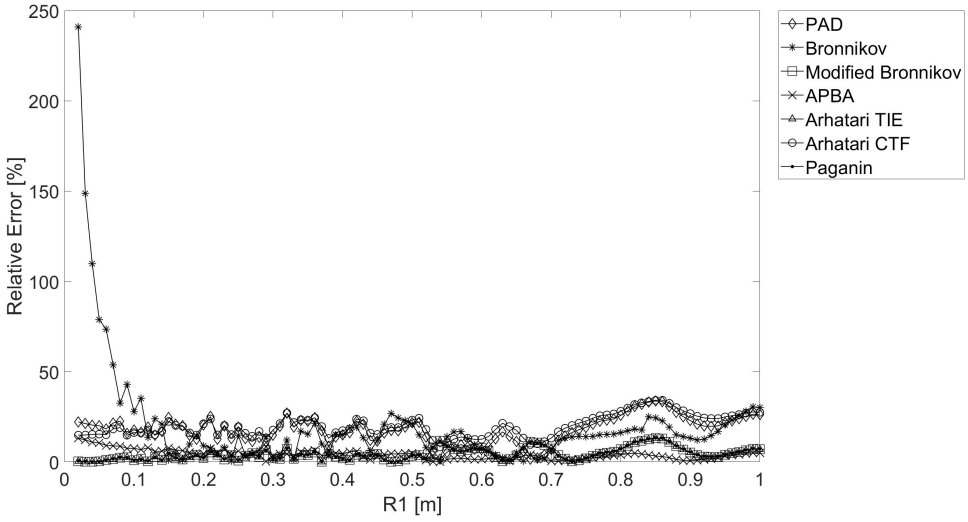

Figure A.23: Relative error versus R_1 for a kapton cylinder retrieved by different phase retrieval methods

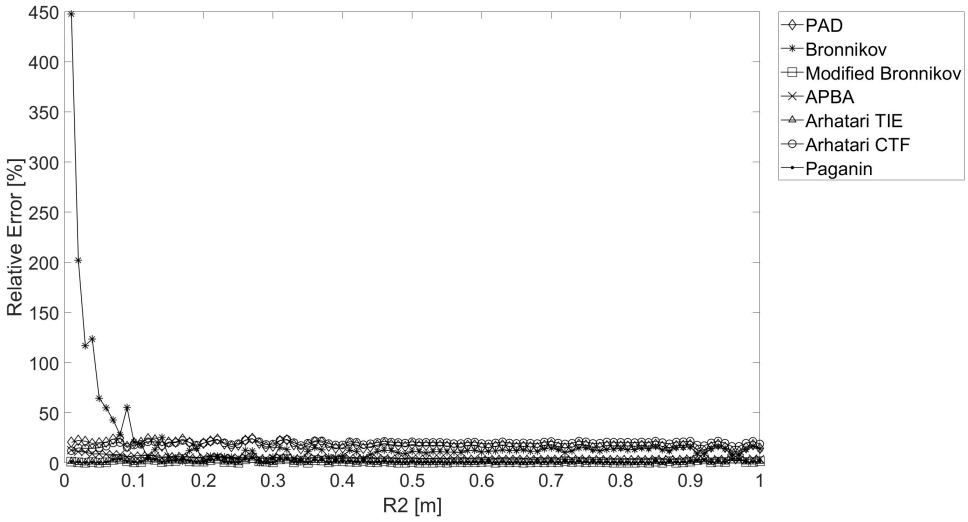

Figure A.24: Relative error versus R_2 with $R_1 = 16$ cm for a kapton cylinder retrieved by different phase retrieval methods

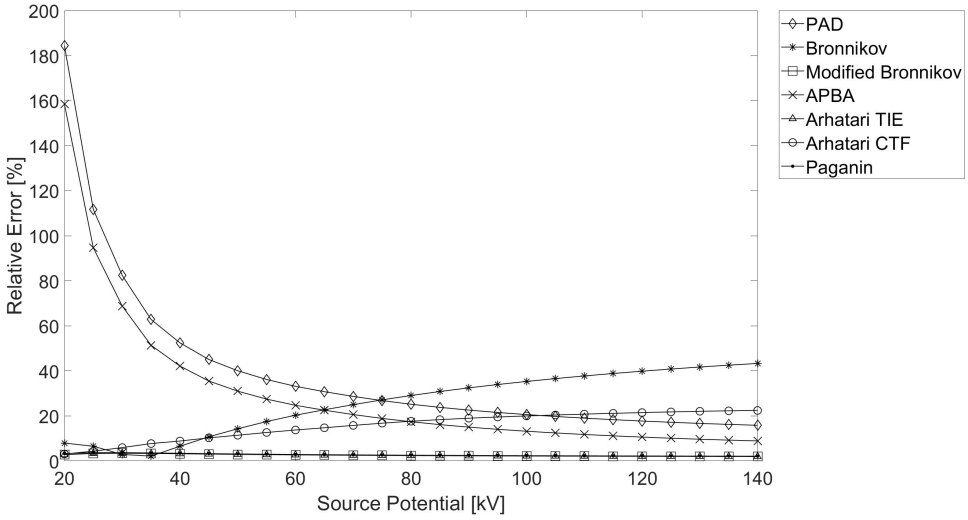

Figure A.25: Relative error versus source potential for a kapton cylinder retrieved by different phase retrieval methods

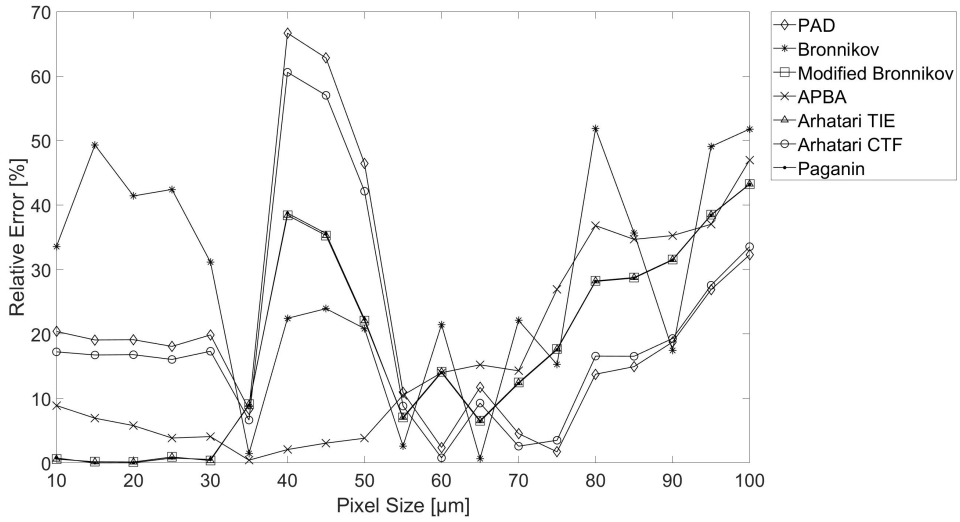

Figure A.26: Relative error versus pixel size for a kapton cylinder retrieved by different phase retrieval methods

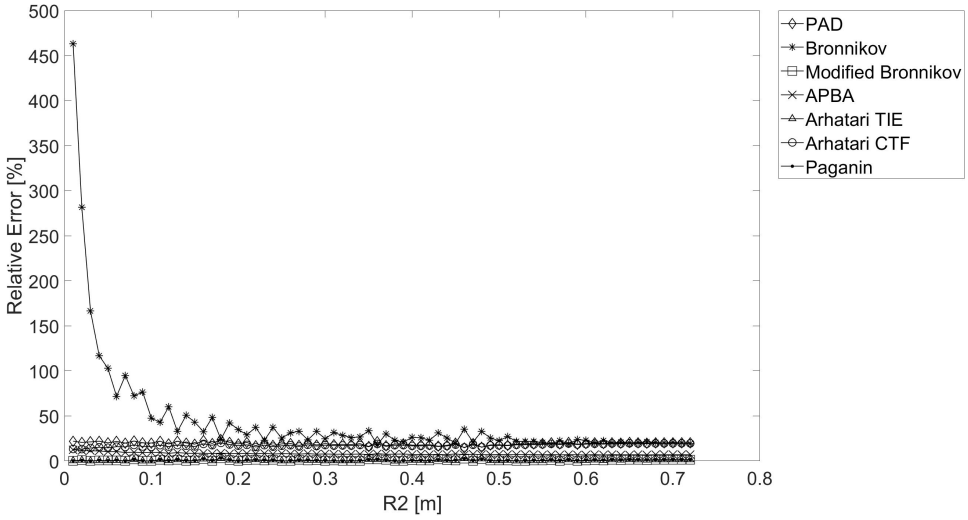

Figure A.27: Relative error versus R_2 with $R_1 = 8$ cm for a kapton cylinder retrieved by different phase retrieval methods

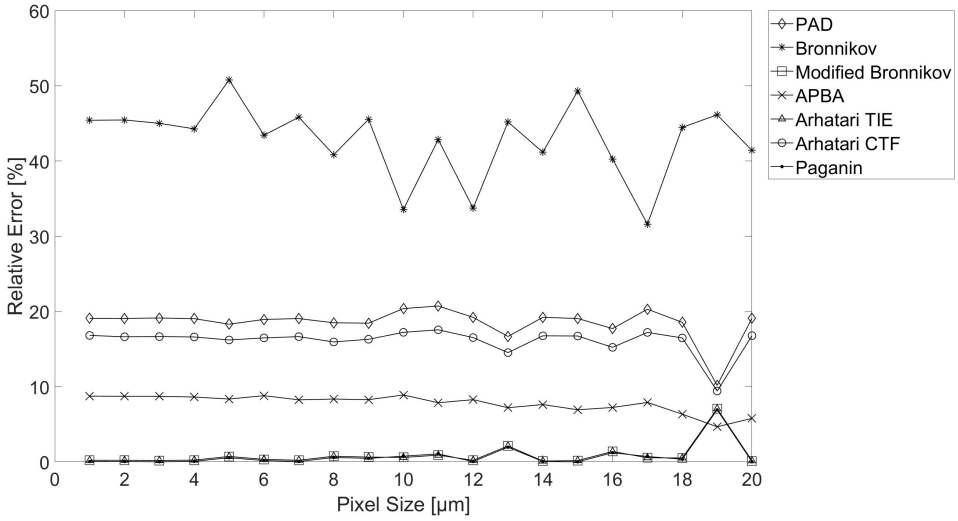

Figure A.28: Relative error versus pixel size for a kapton cylinder retrieved by different phase retrieval methods

Sphere

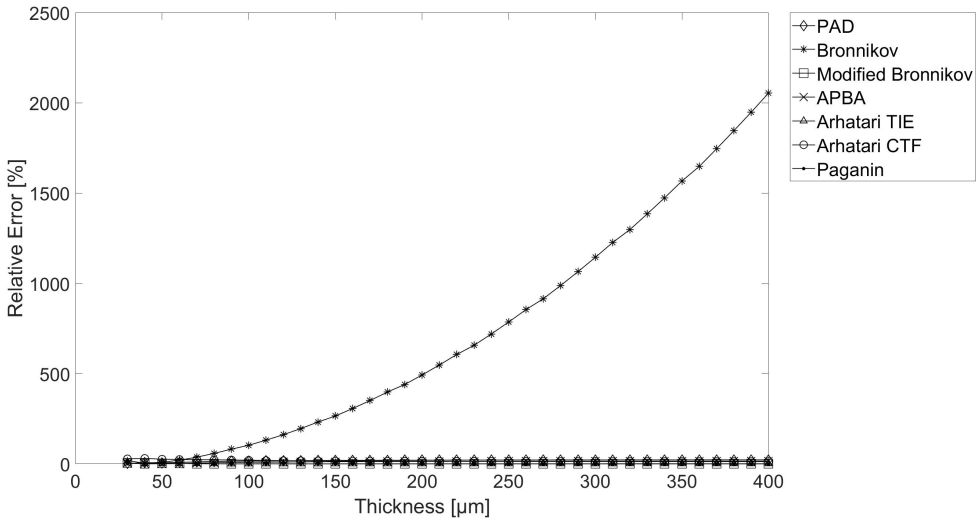

Figure A.29: Relative error versus thickness for a kapton sphere retrieved by different phase retrieval methods

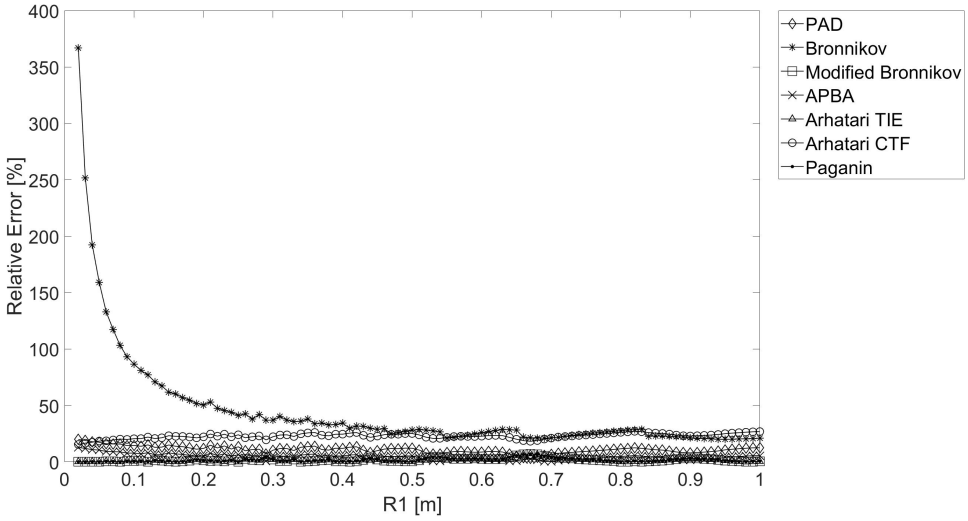

Figure A.30: Relative error versus R_1 for a kapton sphere retrieved by different phase retrieval methods

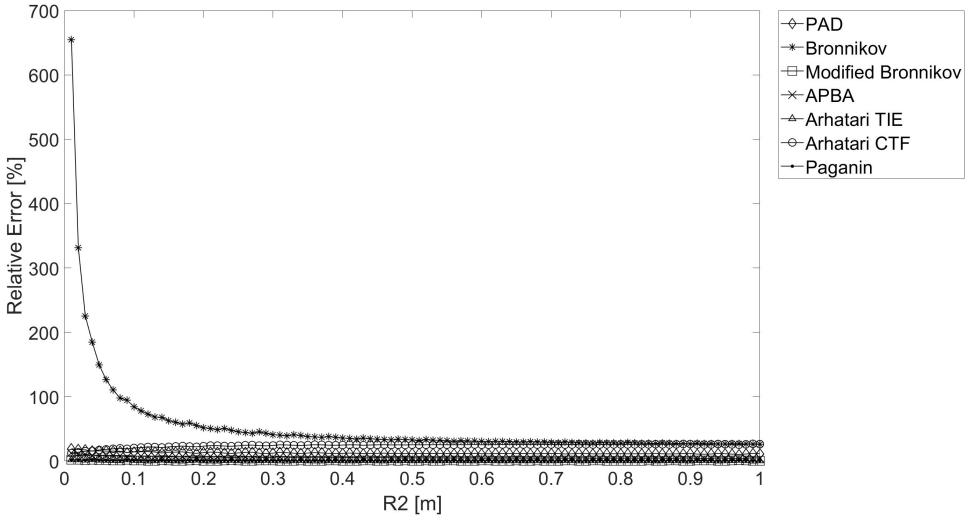

Figure A.31: Relative error versus R_2 with $R_1 = 16$ cm for a kapton sphere retrieved by different phase retrieval methods

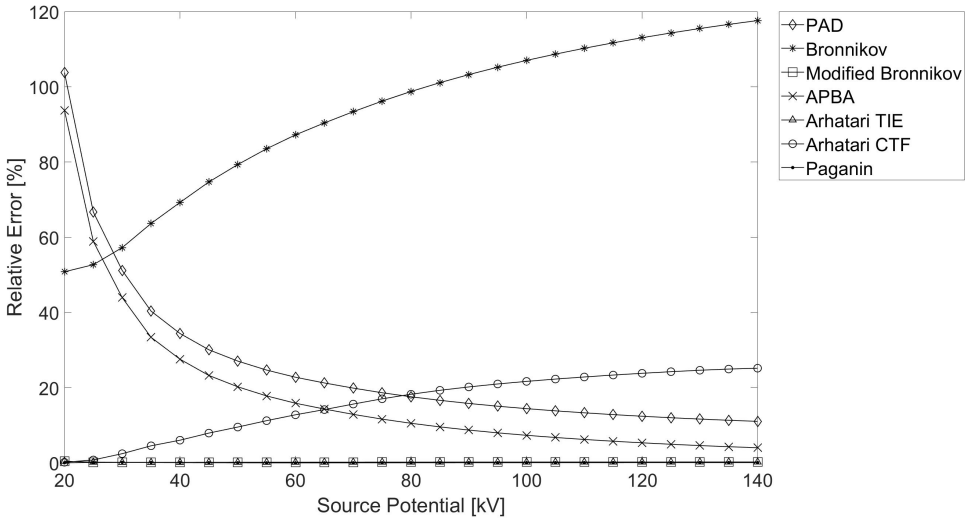

Figure A.32: Relative error versus source potential for a kapton sphere retrieved by different phase retrieval methods

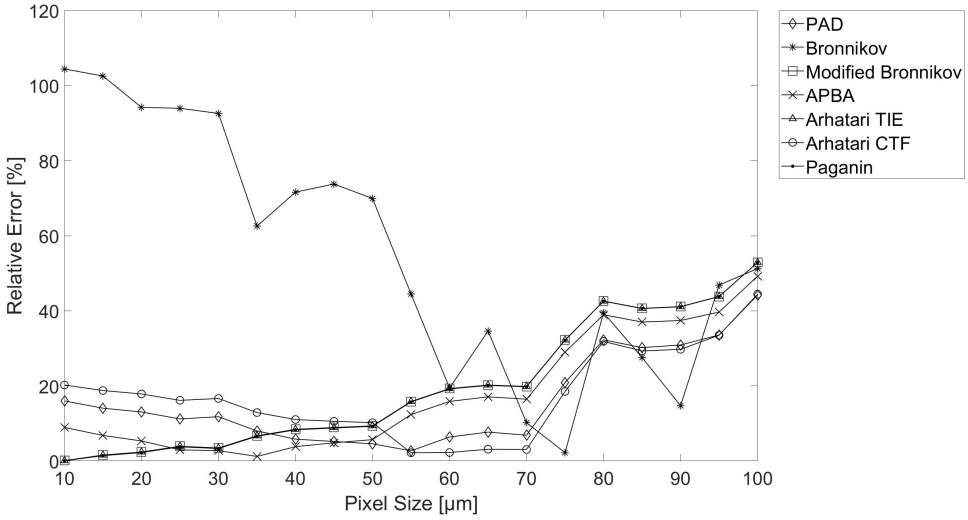

Figure A.33: Relative error versus pixel size for a kapton sphere retrieved by different phase retrieval methods

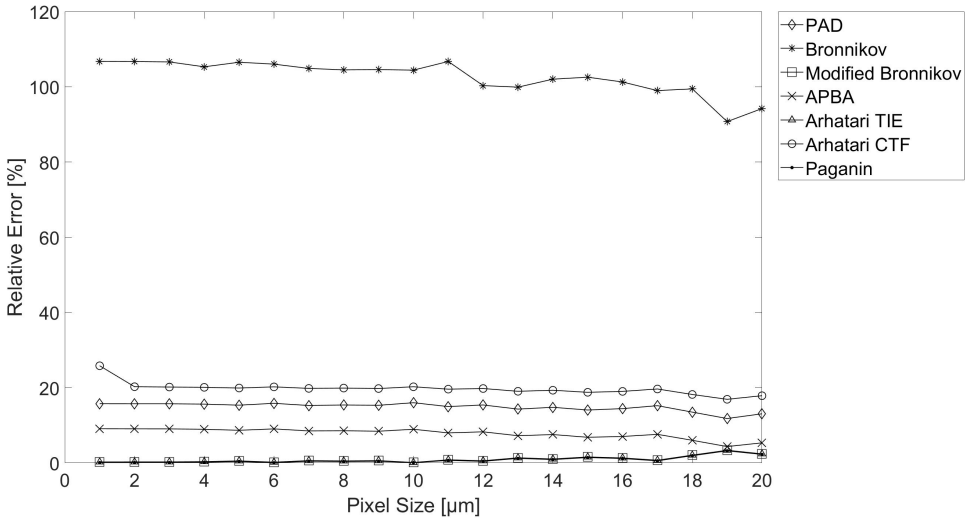

Figure A.35: Relative error versus pixel size for a kapton sphere retrieved by different phase retrieval methods

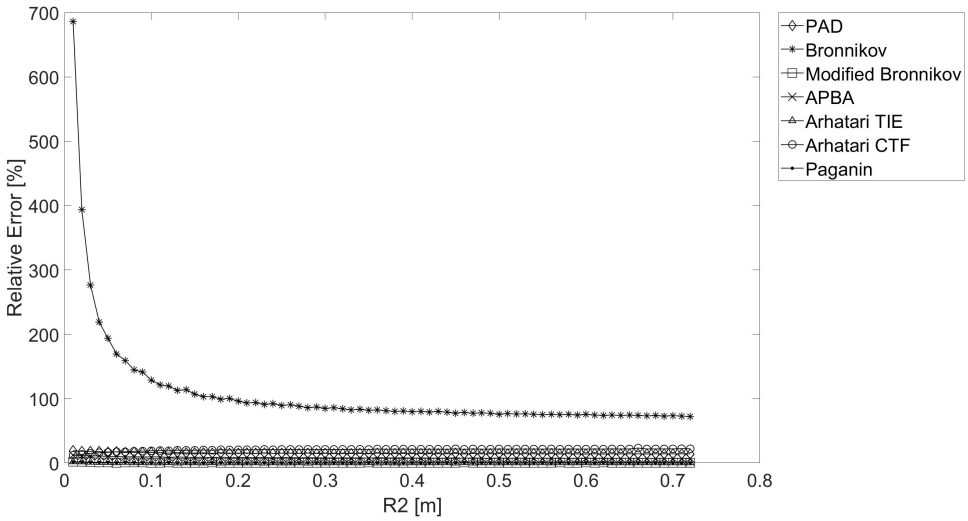

Figure A.34: Relative error versus R_2 with $R_1 = 8$ cm for a kapton sphere retrieved by different phase retrieval methods

A.2.2 Without Bronnikov's Method

Cylinder

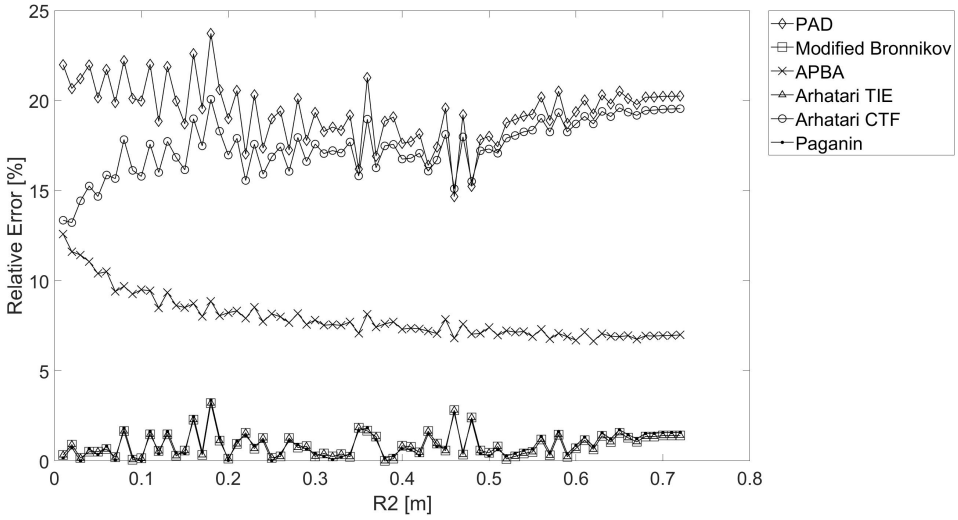

Figure A.36: Relative error versus R_2 with $R_1 = 8$ cm for a kapton cylinder retrieved by different phase retrieval methods

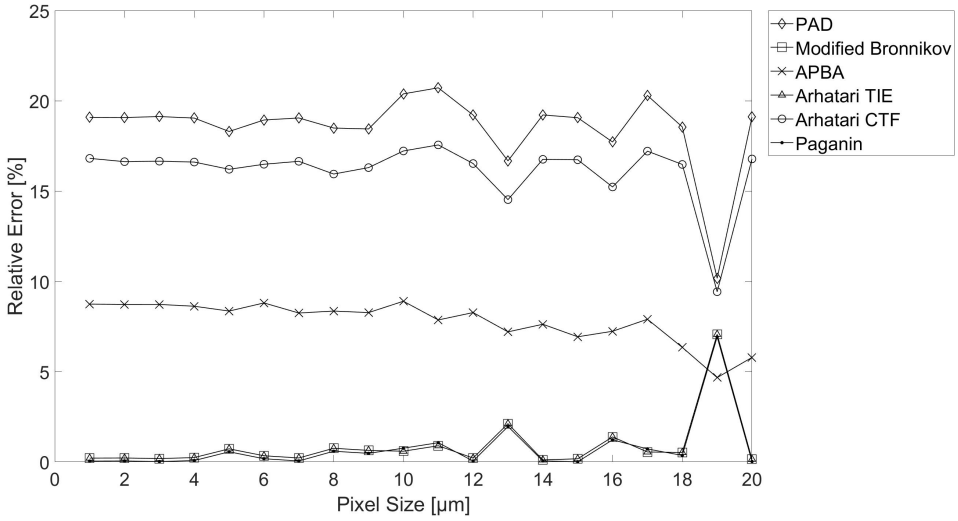

Figure A.37: Relative error versus pixel size for a kapton cylinder retrieved by different phase retrieval methods

Sphere

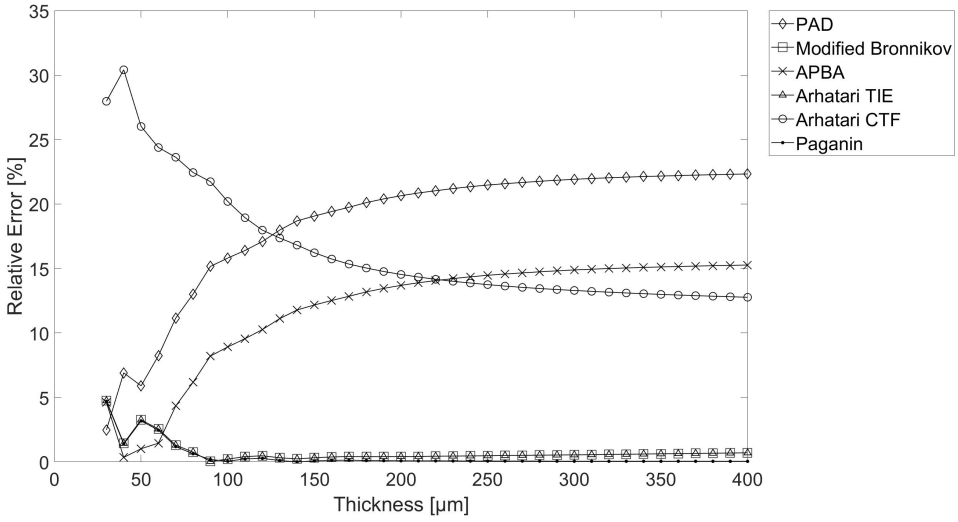

Figure A.38: Relative error versus thickness for a kapton sphere retrieved by different phase retrieval methods

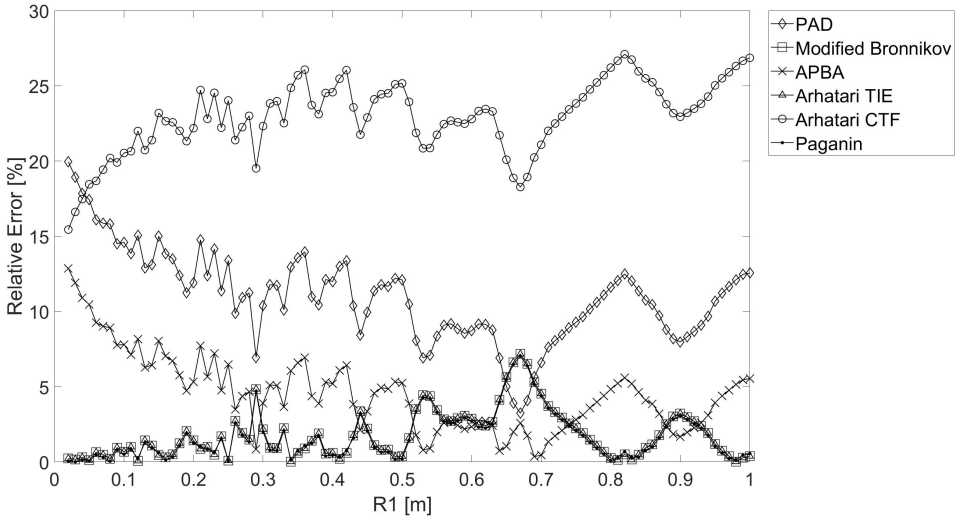

Figure A.39: Relative error versus R_1 for a kapton sphere retrieved by different phase retrieval methods

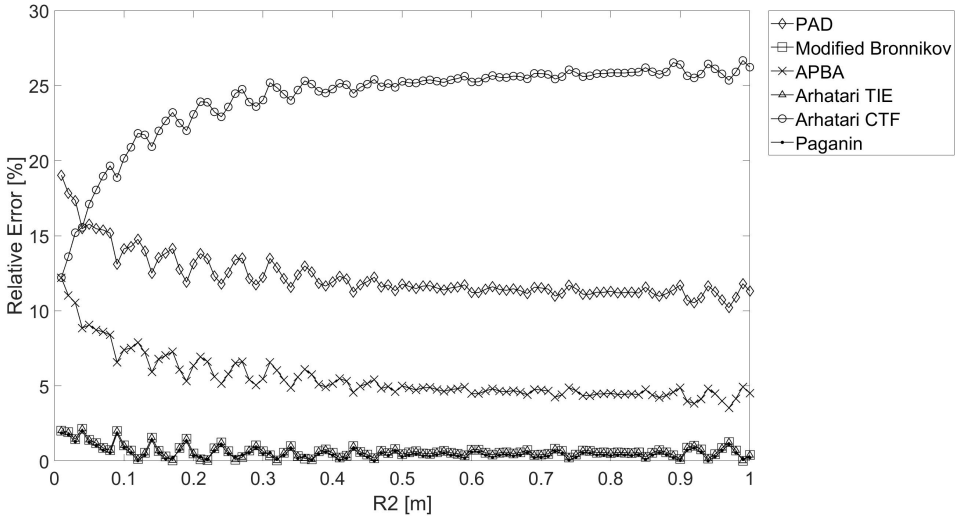

Figure A.40: Relative error versus R_2 with $R_1 = 16$ cm for a kapton sphere retrieved by different phase retrieval methods

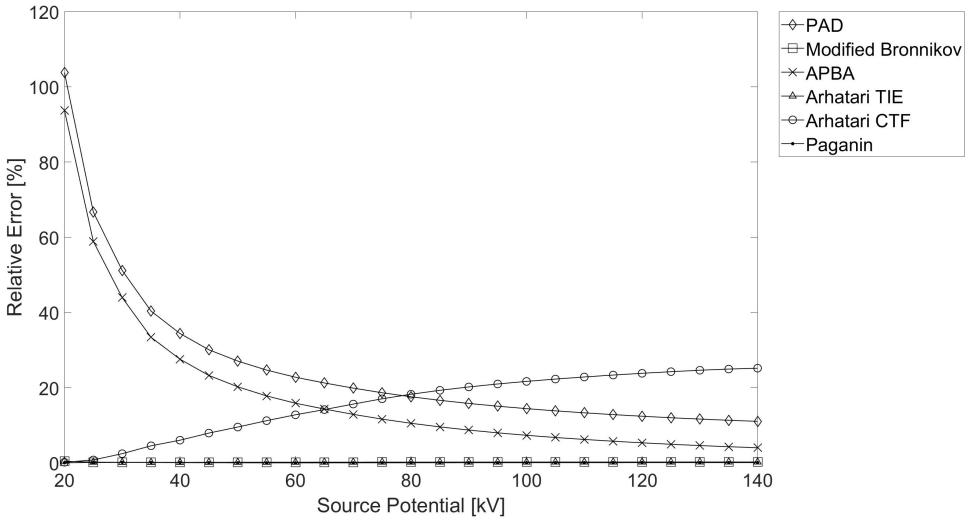

Figure A.41: Relative error versus source potential for a kapton sphere retrieved by different phase retrieval methods

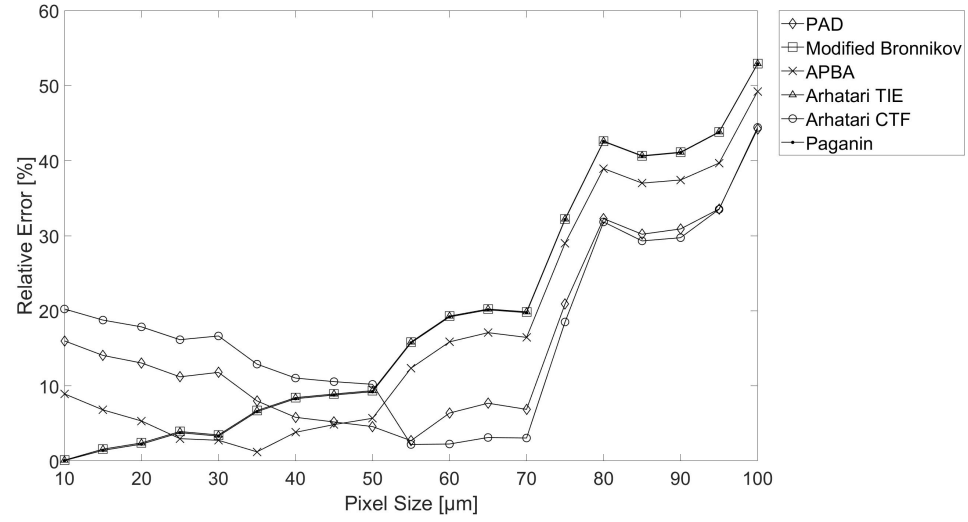

Figure A.42: Relative error versus pixel size for a kapton sphere retrieved by different phase retrieval methods

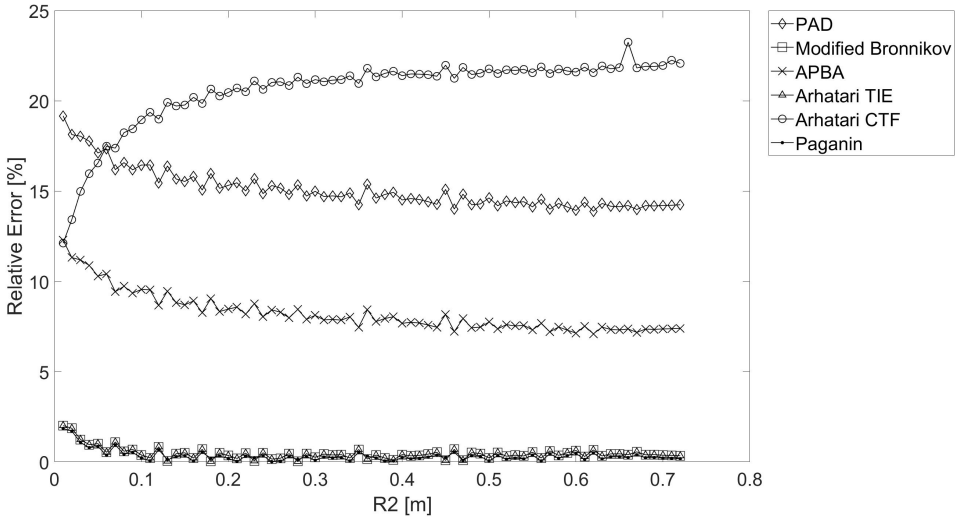

Figure A.43: Relative error versus R_2 with $R_1 = 8$ cm for a kapton sphere retrieved by different phase retrieval methods

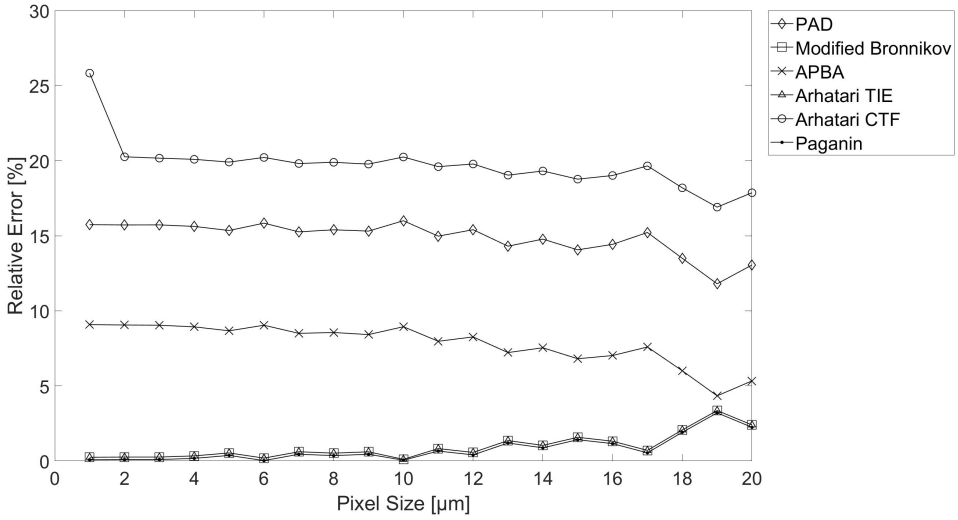

Figure A.44: Relative error versus pixel size for a kapton sphere retrieved by different phase retrieval methods

A.3 PTFE Results

A.3.1 With Bronnikov's Method

Cylinder

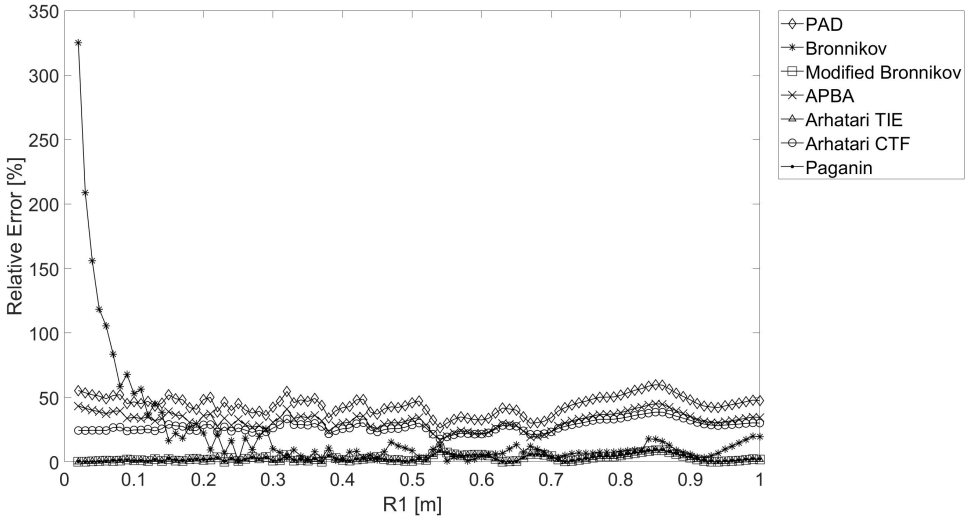

Figure A.45: Relative error versus R_1 for a PTFE cylinder retrieved by different phase retrieval methods

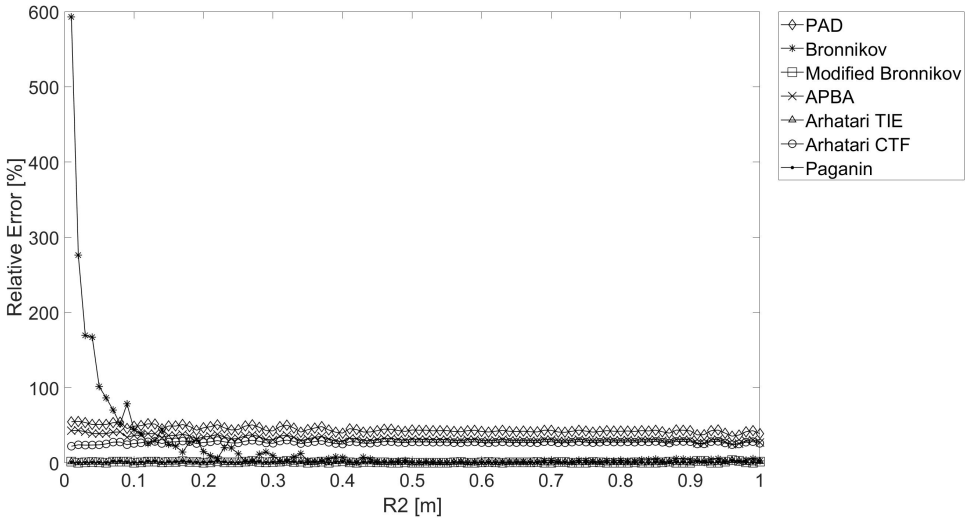

Figure A.46: Relative error versus R_2 with $R_1 = 16$ cm for a PTFE cylinder retrieved by different phase retrieval methods

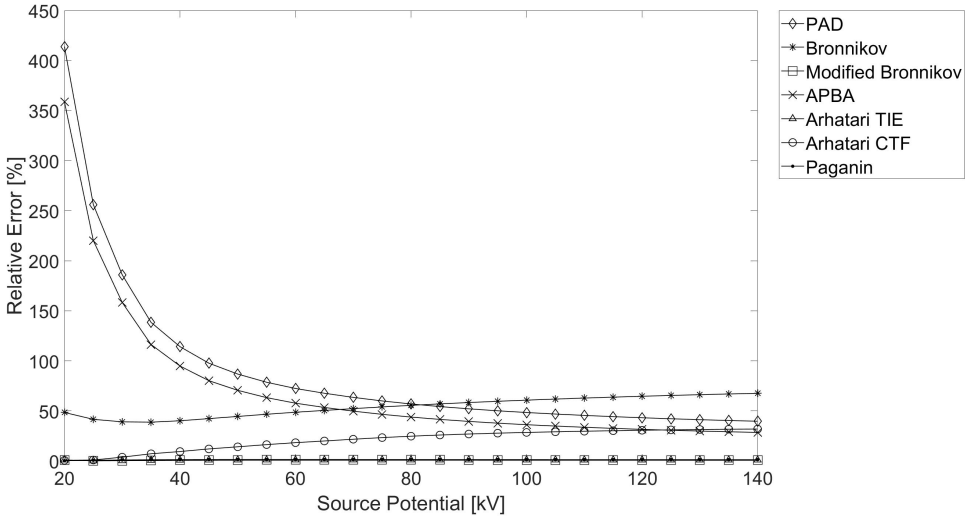

Figure A.47: Relative error versus source potential for a PTFE cylinder retrieved by different phase retrieval methods

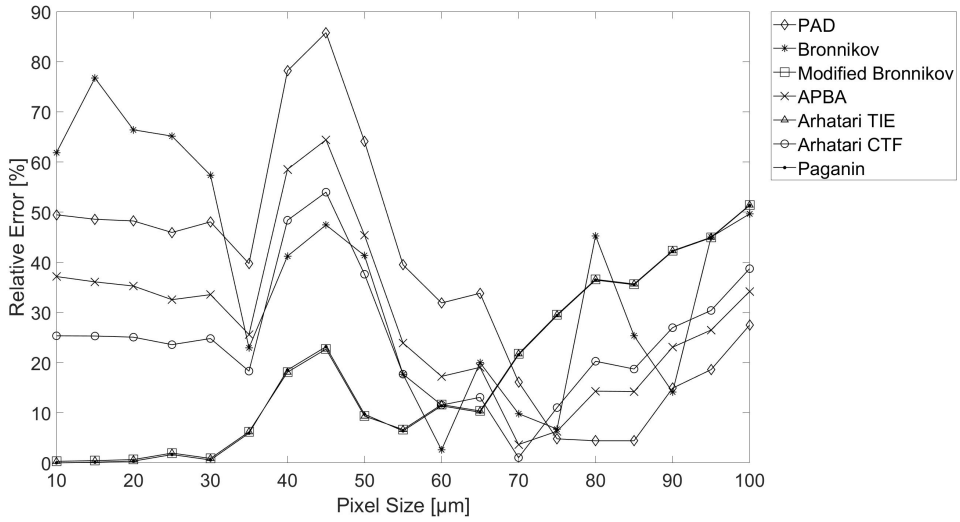

Figure A.48: Relative error versus pixel size for a PTFE cylinder retrieved by different phase retrieval methods

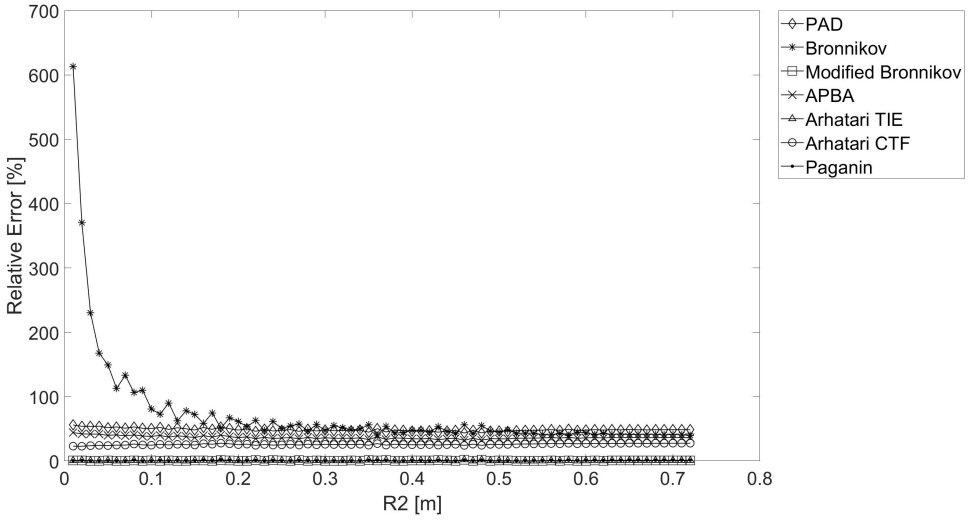

Figure A.49: Relative error versus R_2 with $R_1 = 8$ cm for a PTFE cylinder retrieved by different phase retrieval methods

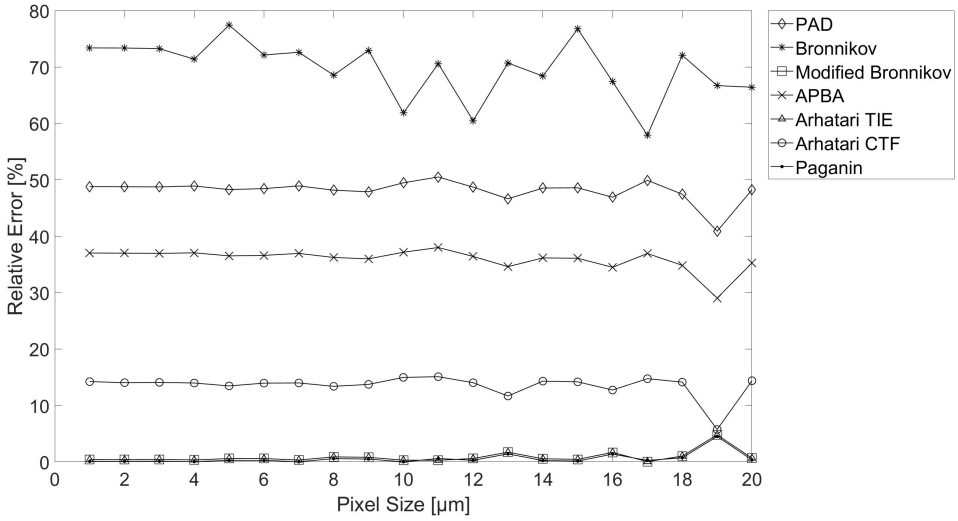

Figure A.50: Relative error versus pixel size for a PTFE cylinder retrieved by different phase retrieval methods

Sphere

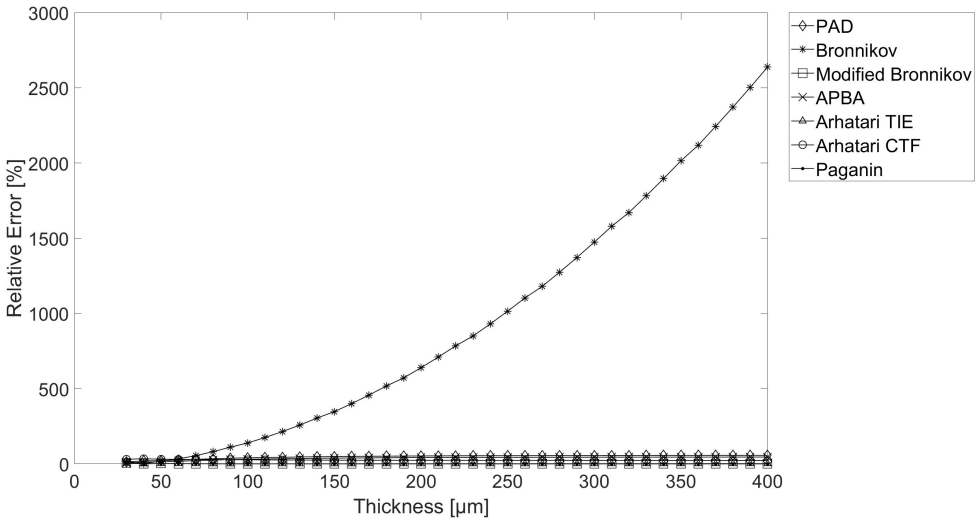

Figure A.51: Relative error versus thickness for a PTFE sphere retrieved by different phase retrieval methods

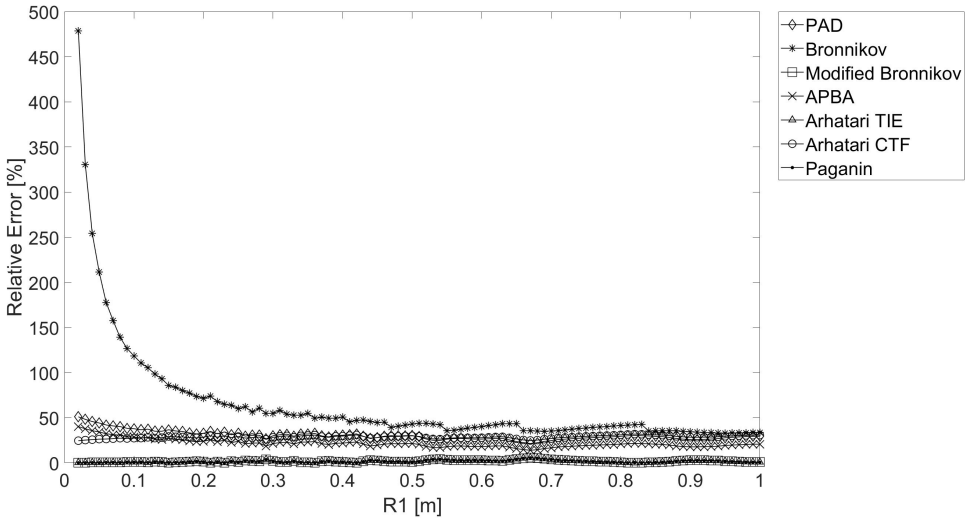

Figure A.52: Relative error versus R_1 for a polystyrene sphere retrieved by different phase retrieval methods

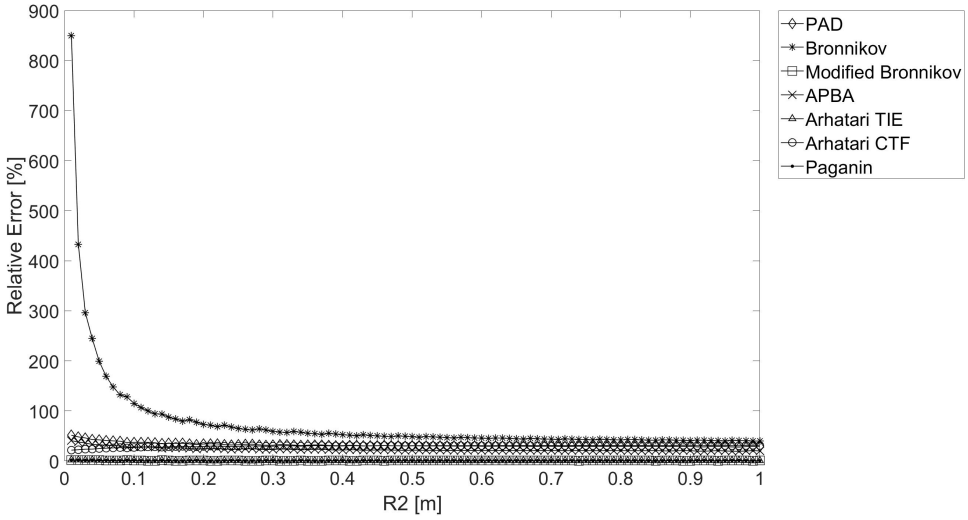

Figure A.53: Relative error versus R_2 with $R_1 = 16$ cm for a PTFE sphere retrieved by different phase retrieval methods

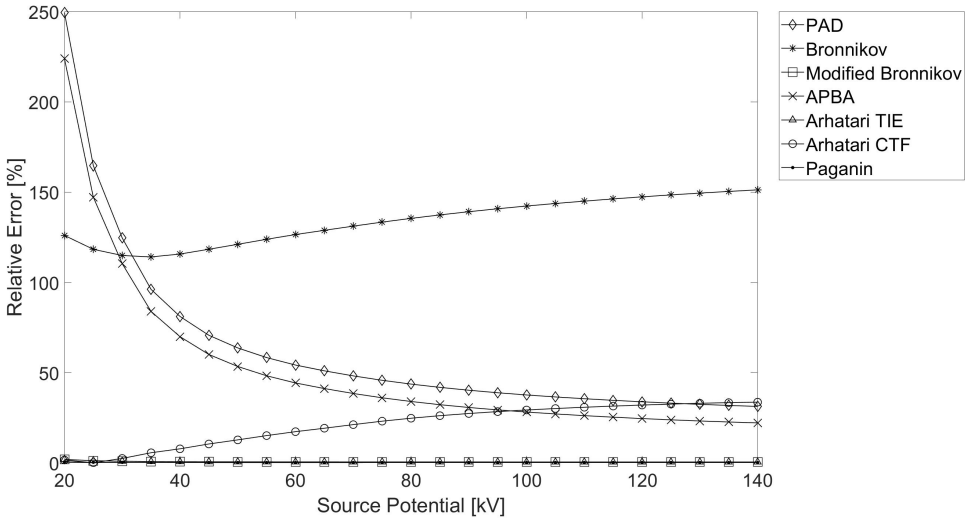

Figure A.54: Relative error versus source potential for a PTFE sphere retrieved by different phase retrieval methods

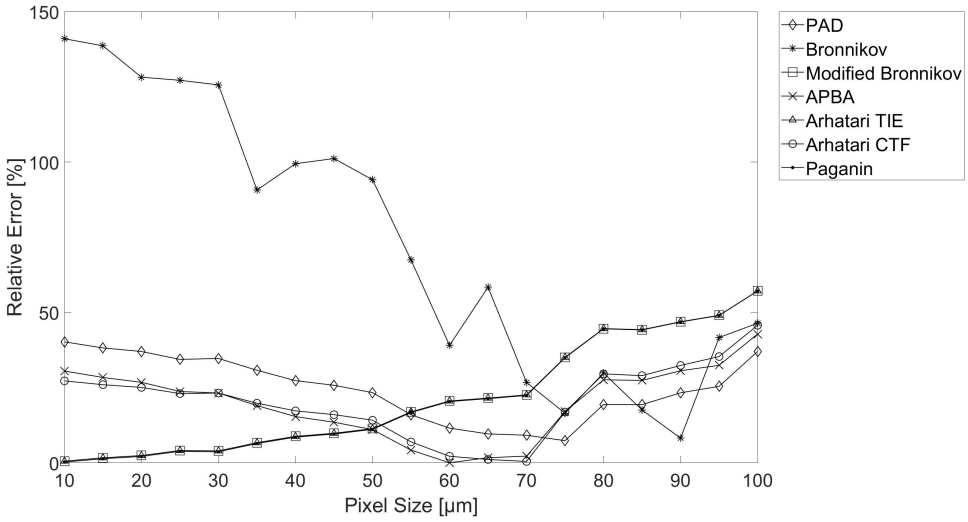

Figure A.55: Relative error versus pixel size for a PTFE sphere retrieved by different phase retrieval methods

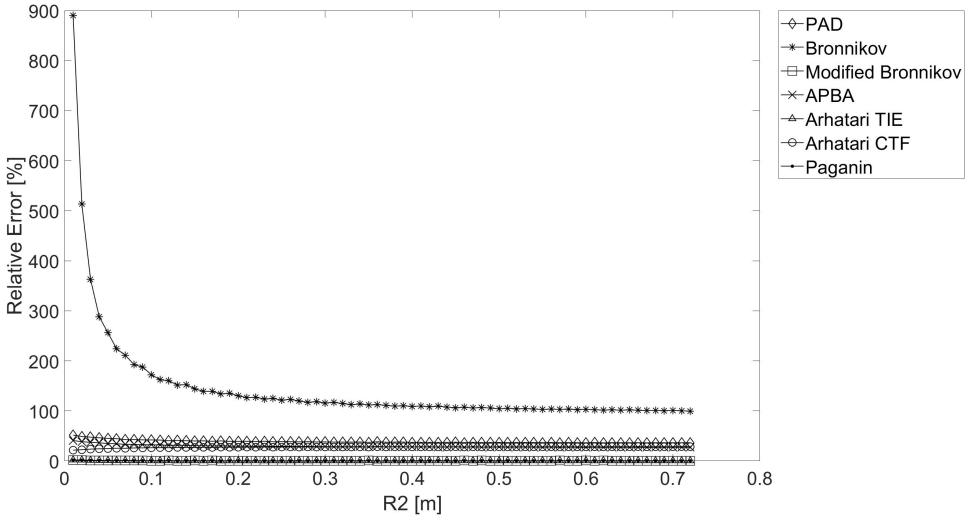

Figure A.56: Relative error versus R_2 with $R_1 = 8$ cm for a PTFE sphere retrieved by different phase retrieval methods

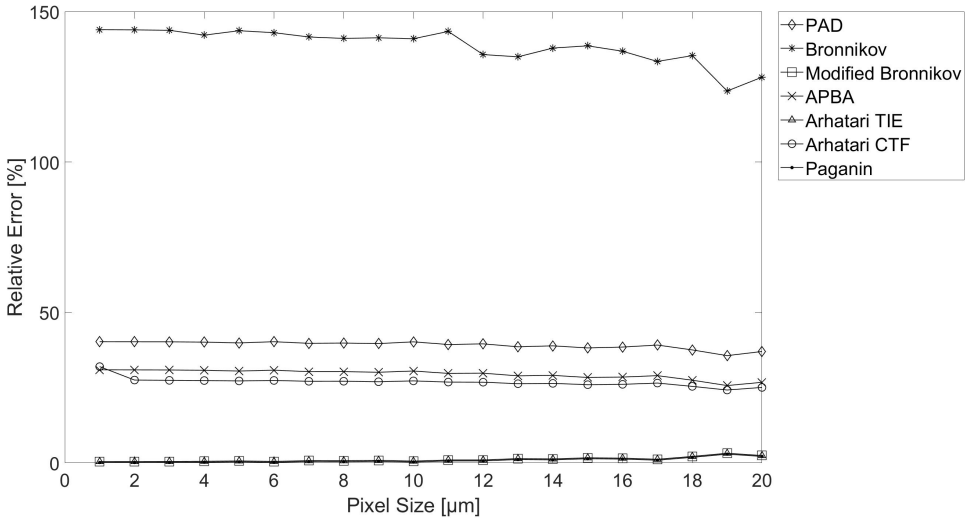

Figure A.57: Relative error versus pixel size for a PTFE sphere retrieved by different phase retrieval methods

A.3.2 Without Bronnikov's Method

Cylinder

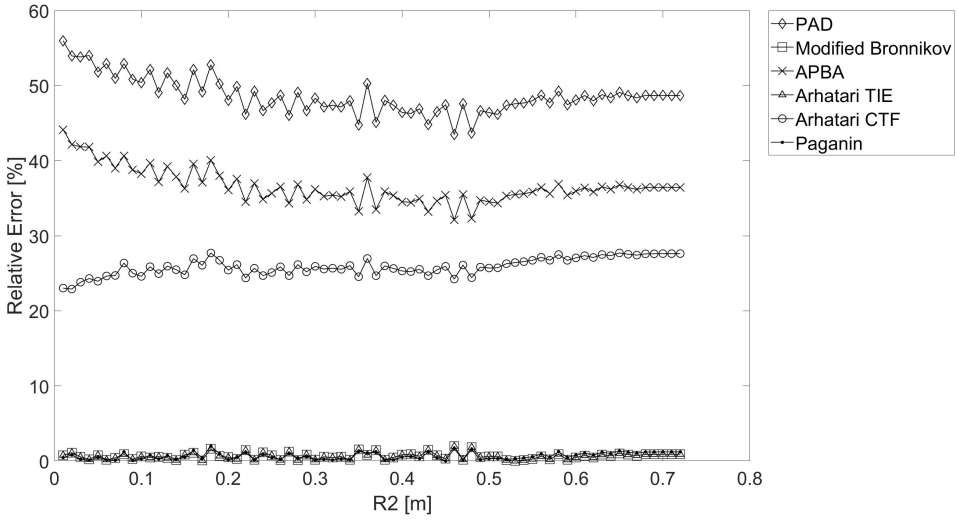

Figure A.58: Relative error versus R_2 with $R_1 = 8$ cm for a PTFE cylinder retrieved by different phase retrieval methods

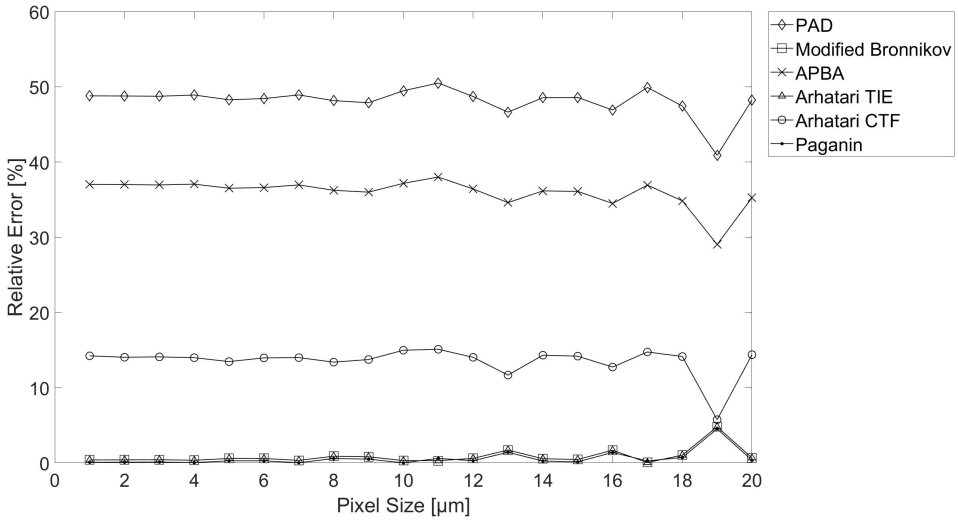

Figure A.59: Relative error versus pixel size for a PTFE cylinder retrieved by different phase retrieval methods

Sphere

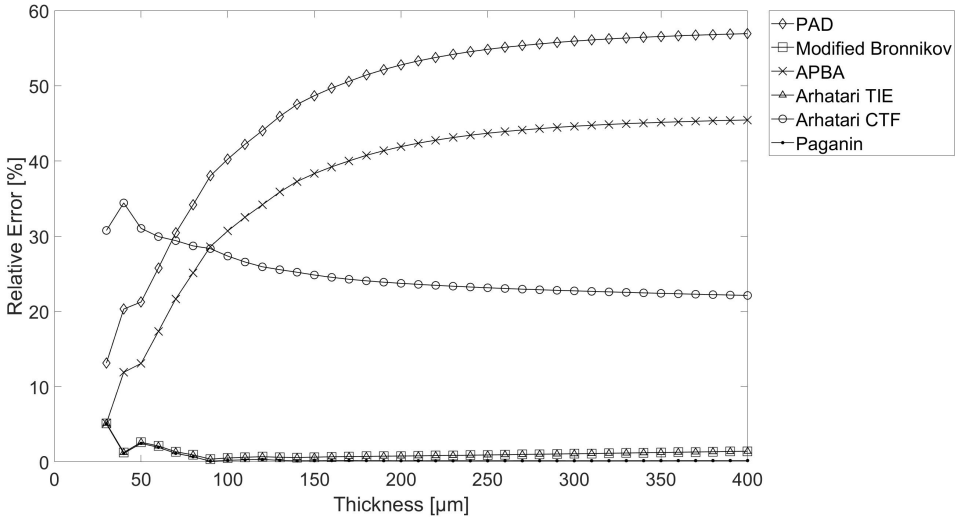

Figure A.60: Relative error versus thickness for a PTFE sphere retrieved by different phase retrieval methods

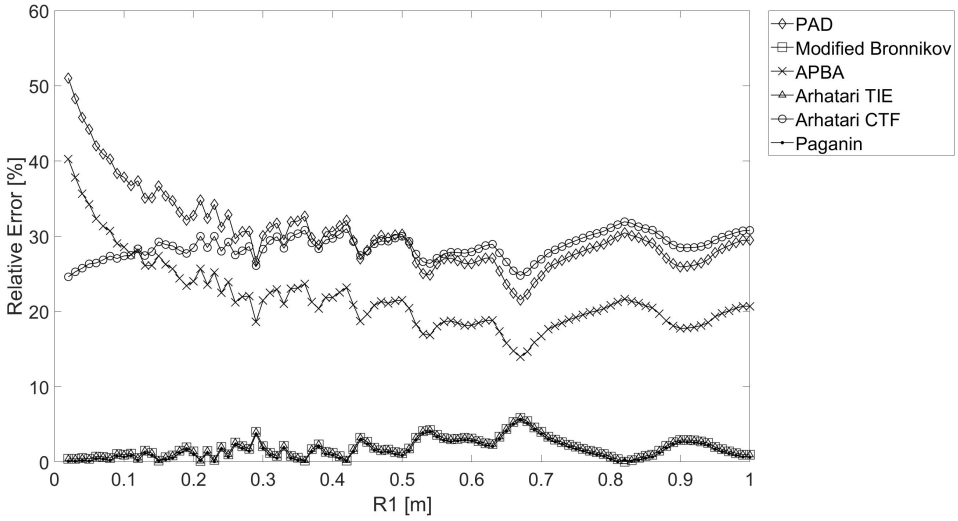

Figure A.61: Relative error versus R_1 for a PTFE sphere retrieved by different phase retrieval methods

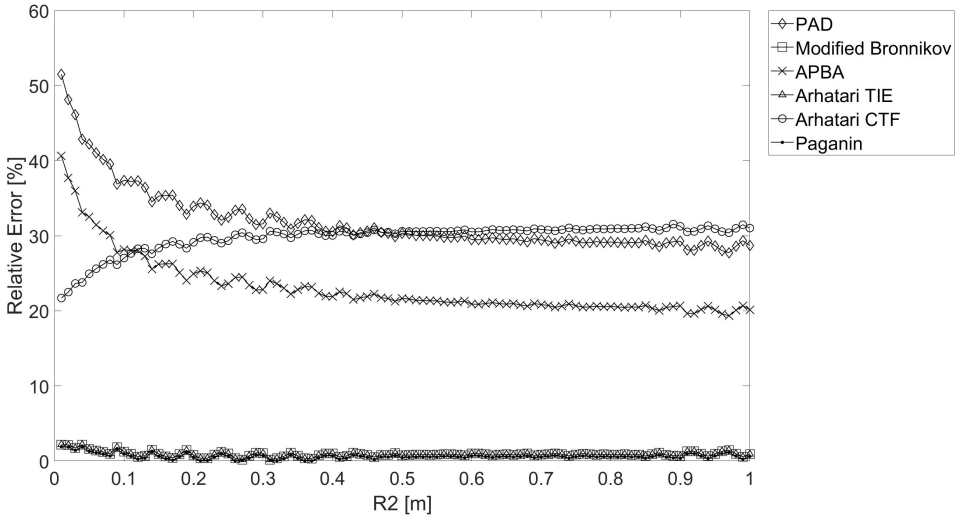

Figure A.62: Relative error versus R_2 with $R_1 = 16$ cm for a PTFE sphere retrieved by different phase retrieval methods

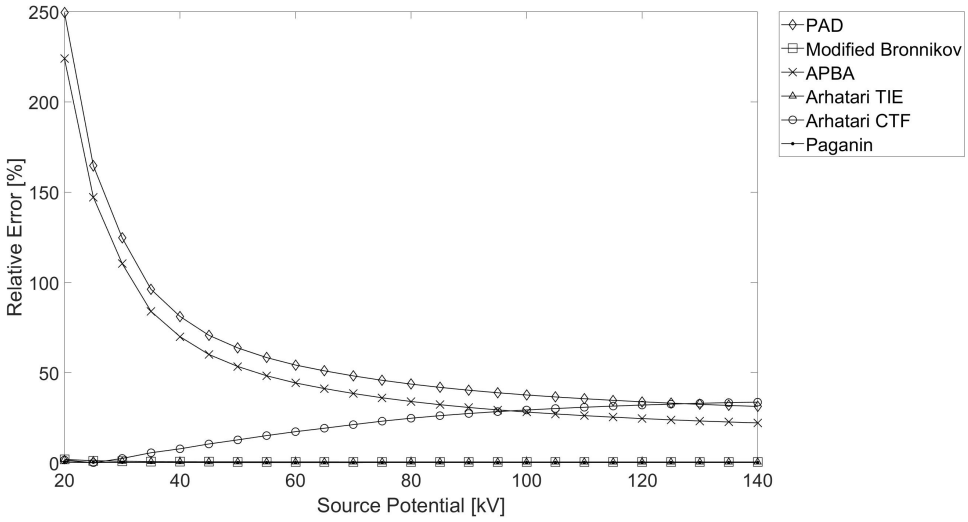

Figure A.63: Relative error versus source potential for a PTFE sphere retrieved by different phase retrieval methods

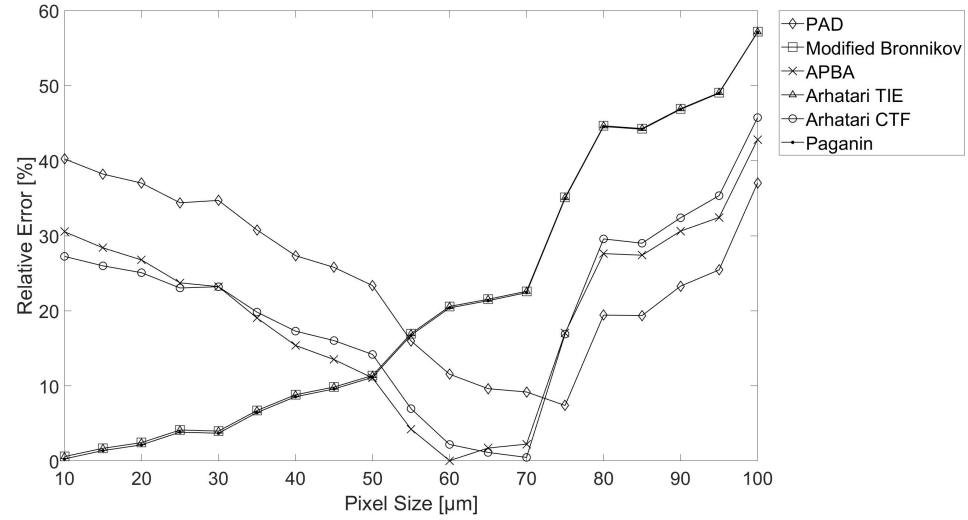

Figure A.64: Relative error versus pixel size for a PTFE sphere retrieved by different phase retrieval methods

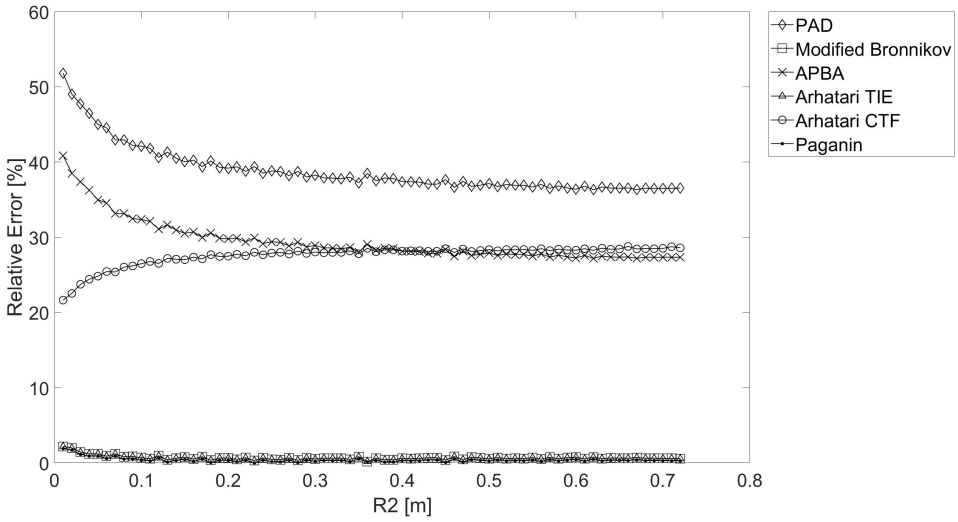

Figure A.65: Relative error versus R_2 with $R_1 = 8$ cm for a PTFE sphere retrieved by different phase retrieval methods

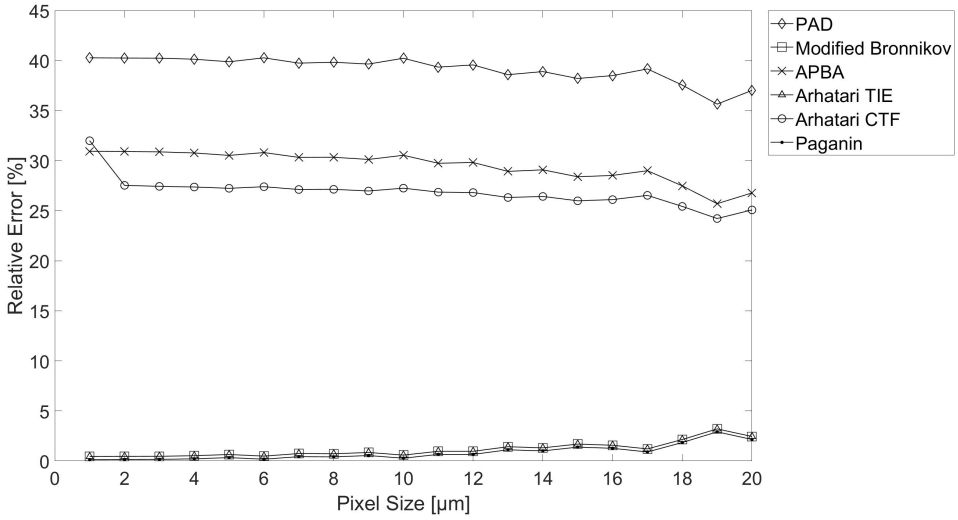

Figure A.66: Relative error versus pixel size for a PTFE sphere retrieved by different phase retrieval methods

Appendix B

Effect of Materials Results

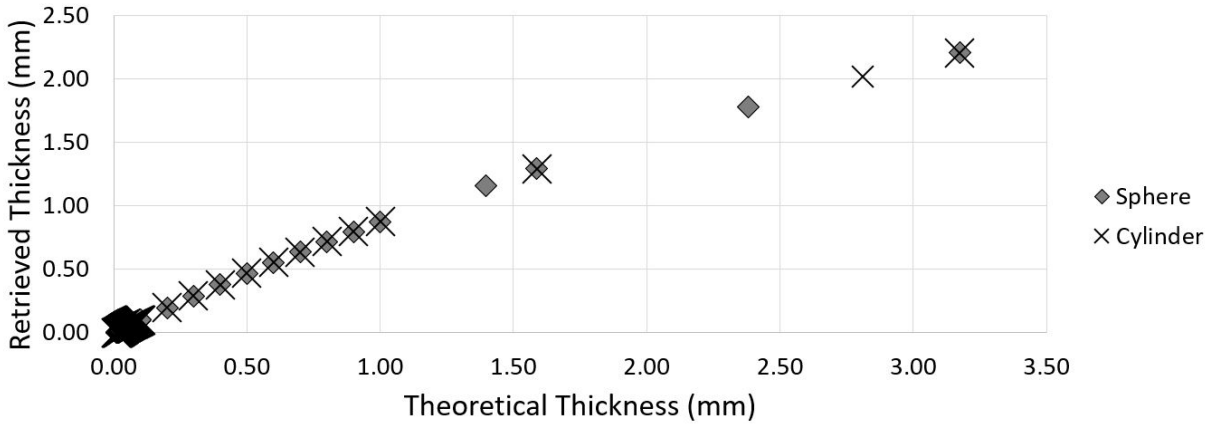

Figure B.1: Retrieved thickness versus theoretical thickness comparing the results of a simulated PTFE sphere and cylinder using the 40 kV Thermo Scientific spectrum

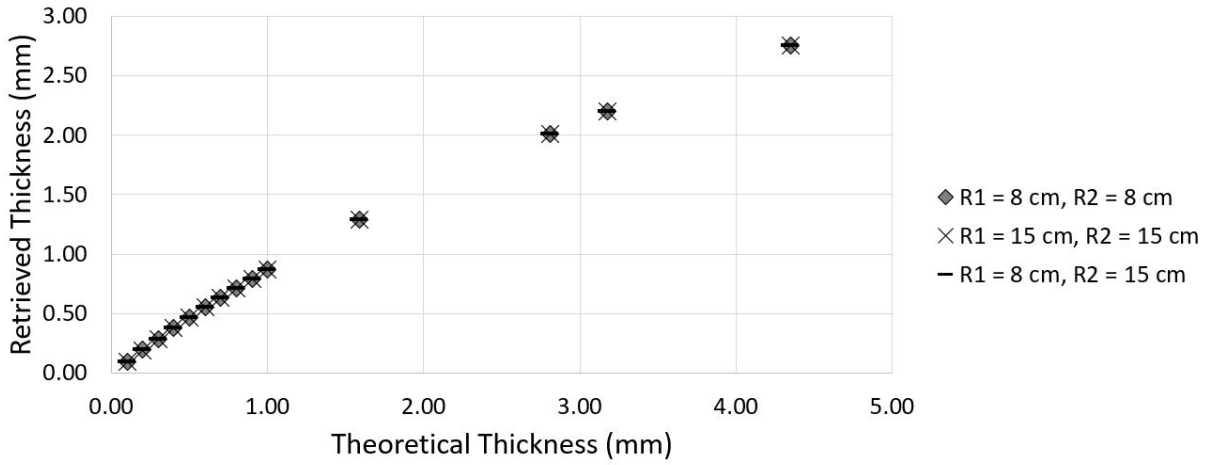

Figure B.2: Retrieved thickness versus theoretical thickness of a PTFE cylinder varying R_1 and R_2 using the 40 kV Thermo Scientific spectrum

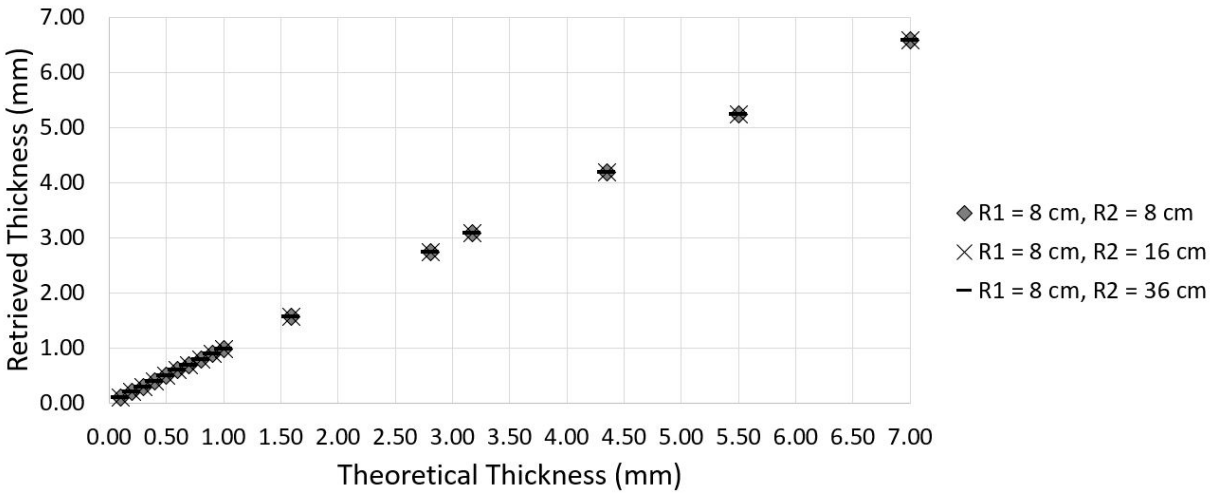

Figure B.3: Retrieved thickness versus theoretical thickness of a polystyrene cylinder varying R_1 and R_2 using the 40 kV Thermo Scientific spectrum

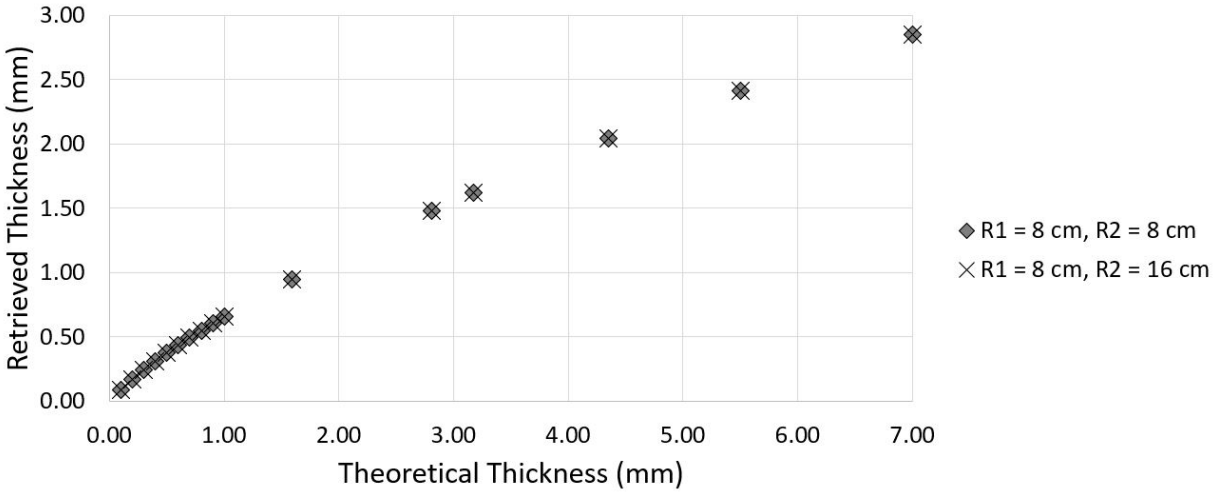

Figure B.4: Retrieved thickness versus theoretical thickness of a polystyrene cylinder varying R_1 and R_2 using the 100 kV L12531 Hamamatsu spectrum

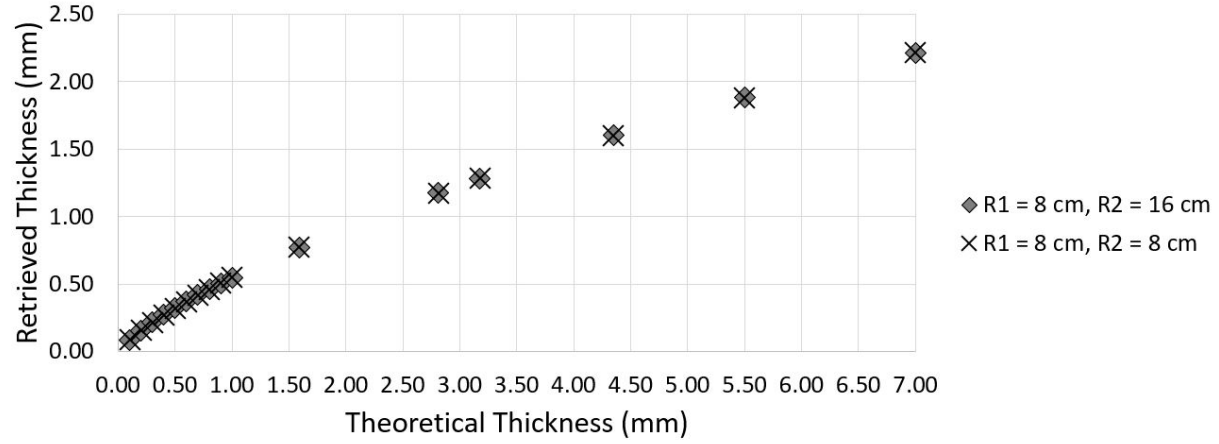

Figure B.5: Retrieved thickness versus theoretical thickness of a kevlar cylinder varying R_1 and R_2 using the 60 kV L12531 Hamamatsu spectrum

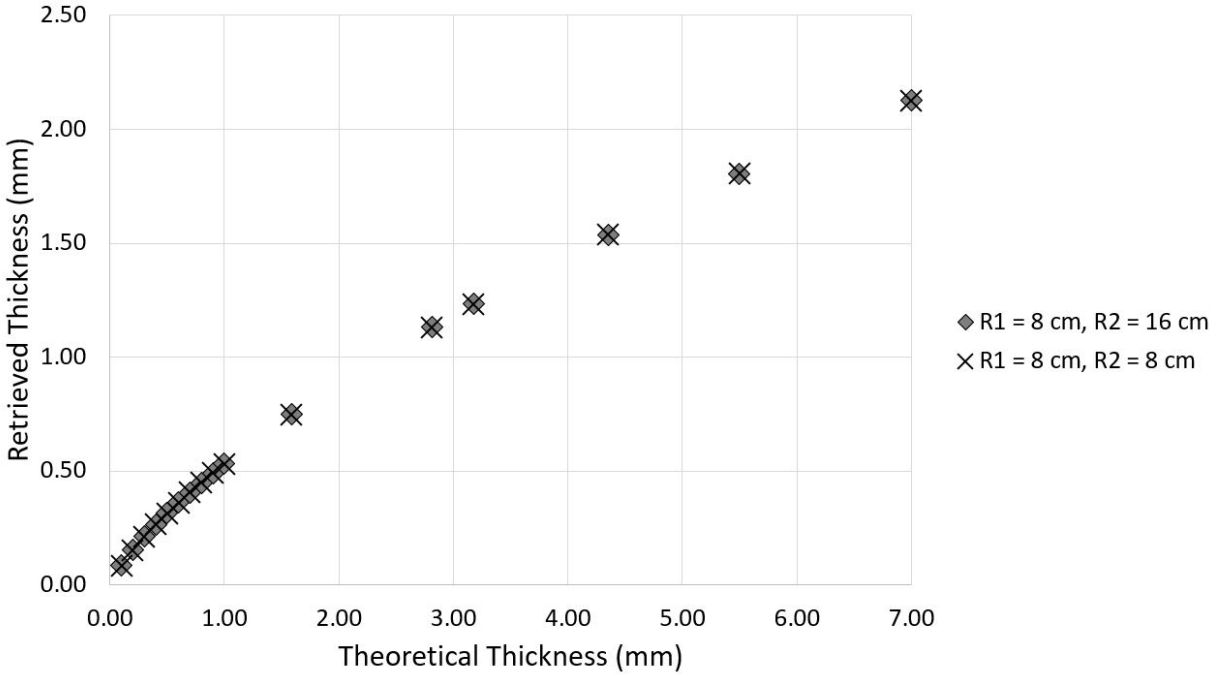

Figure B.6: Retrieved thickness versus theoretical thickness of a kevlar cylinder varying R_1 and R_2 using the 100 kV L12531 Hamamatsu spectrum

Appendix C

Attenuation Partition Based Algorithm Matlab Code

```
%%%%%%%%%%%%%%%%%%%%%%%%%%%%%%%%%%%%%%%%%%%%%%%%%%%%%%%%%%%%%%%%%%%%%%%%%%%%%%%%
%
%Starts the phase mapping program
%
%%%%%%%%%%%%%%%%%%%%%%%%%%%%%%%%%%%%%%%%%%%%%%%%%%%%%%%%%%%%%%%%%%%%%%%%%%%%%%%%
L = 0;
for j = 20:5:140
L = L+1;
r = 50*1e-6; %[m] radius of sphere
R1 = 0.08; % [m] SOD
R2 = 0.16; % [m] ODD
Rtot = R1 + R2; % [m] SDD
M = Rtot/R1; %[unitless] magnification
z = R2/M; %[m] effective propagation distance

%Detector
% p = 7.8e-6; %[m] pixel pitch
%Detector
p = 7.8*1e-6; %[m] pixel pitch
% p=5e-6;
%Simulation resolution of field of view
model_res = p/10; %[m]
```

```
dx = model_res; %[m]
dy = model_res; %[m]
xfov = 3*r; %[m] field of view
yfov = 3*r; %[m]
xmin = -xfov/2; xmax = xfov/2; %[m] x range of field of view in object plane
ymin = -yfov/2; ymax = yfov/2; %[m] y range of field of view in object plane
x = xmin:dx:xmax; y = ymin:dy:ymax; %[m] coordinate vectors
[X,Y] = meshgrid(x,y); %[m] coordinate matrices

%Spatial frequencies
nx = length(x); ny = length(y); %[unitless] number of pixels in x and y direction
%[1/m] frequency in the x and y direction respectively
u = ifftshift((-floor(nx/2):floor((nx-1)/2))/(nx*dx));
v = ifftshift((-floor(ny/2):floor((ny-1)/2))/(ny*dy));
[U,V] = meshgrid(u,v); %[1/m] frequency grid
w2 = U.^2+V.^2; %[1/m^2]

%physical constants
c = 299792458; %[m/s] speed of light
h = 6.6260689633e-34; %[Js] Planck's constant
eV = 1.6022e-19; %[J/eV] unit conversion constant
re = 2.82e-15; %[m] classical electron radius
Na = 6.022e23; %[atoms/mol] Avogradro's number
me = 9.10938356e-31; %[kg] mass of an electron

%X-ray energy
E = [1:150]*1e3'; % [eV]
inherent_filtration = [spektrElement2Z('Be'), 0.1]; % [mm Be]
added_filtration = [[spektrElement2Z('Al'), 2.0]]; % [mm Al]
kVp = j; % [kVp]

Phi_tube = spektrSpectrum(kVp, inherent_filtration); % spectrum with inherent filtratio
spectrum = spektrBeers(Phi_tube, added_filtration); % spectrum with filtration
Quanta = sum(spectrum); % Number of quanta

lambda = c*h./(E*eV); %[m] wavelength
k = 2*pi./lambda; %[rad/m] angular wave number
```

```
%Teflon information for delta (phase coefficient):
%C2F4 is PTFE
% rho = 2.2; %density of PTFE [g/cm^3]
% Num_of_C = 2;
% Num_of_F = 4;
%
% %Molar Mass
% MMC = 12.011*Num_of_C; %[g/mol]
% MMF = 18.998*Num_of_F; %[g/mol]
% MM_total = MMC + MMF; %[g/mol]
%
% ZC = 6;
% ZF = 9;
%
% Z = ZC*Num_of_C + ZF*Num_of_F; %total atomic number
% nz_total = rho*1e6*1/MM_total*Na; %atoms/m^3
% delta = re*h^2*c^2./(2*pi*(E*eV).^2).*nz_total*Z;

% rho = 1.04; % density of polystyrene [g/cm^3]
%
% Num_of_C = 8;
% Num_of_H = 8;
% Num_of_F = 0;
% %
% % %Atomic numbers
% ZH = 1;
% ZC = 6;
% ZF = 9;

%Teflon information for delta (phase coefficient):
%C2F4 is PTFE
% rho = 2.21439238; % density of PTFE [g/cm^3]
% Num_of_C = 2;
% Num_of_F = 4;
% Num_of_H = 0;

%Molar Mass
```

```
% MMC = 12.011*Num_of_C; % [g/mol]
% MMH = 1.008*Num_of_H; % [g/mol]
% MMF = 18.998*Num_of_F; % [g/mol]
% MM_total = MMC + MMH + MMF; % [g/mol] total molar mass

% Z = ZC*Num_of_C + ZH*Num_of_H+ ZF*Num_of_F; %total atomic number

% %Kapton
rho = 1.42; %[g/m^3] Density of Kapton Polyimide film
%
% % Composition C22H10N2O5
Num_of_C = 22;
Num_of_H = 10;
Num_of_N = 2;
Num_of_O = 5;

% Molar Mass
MMC = 12.011*Num_of_C; %[g/mol]
MMH = 1.008*Num_of_H; %[g/mol]
MMN = 14.00670*Num_of_N; %[g/mol]
MMO = 15.9994*Num_of_O; %[g/mol]
MM_total = MMC + MMH + MMN + MMO; %[g/mol] total molar mass

% Atomic numbers
ZH = 1;
ZC = 6;
ZN = 7;
ZO = 8;

Z = ZC*Num_of_C +ZH*Num_of_H + ZN*Num_of_N + ZO*Num_of_O;

nz_total = rho*1e6*1/MM_total*Na; %atoms/m^3;

delta = re*h^2*c^2./(2*pi*(E*eV).^2).*(nz_total*Z);

%Detector
rho_Se = 4.819; %[g/cm^3] density of selenium
mu_Se = spektrMuRhoElement(34)*rho_Se*100; %[1/m] attenuation
```

```
E_mu = [1:150]*1e3; %Spektr energies [eV]
mu_Se = interp1(E_mu, mu_Se, E);
thickness_Selenium = 100e-6; % [m] thickness of selenium deposited on the detector
eta = 1-exp(-mu_Se.*thickness_Selenium);
spectrum = spectrum'.*eta;

%[1/m] sample attenuation coefficient for the energies E
% mu = spektrMuRhoCompound([6 2; 9 4])*rho*100; %[1/m] attenuation coefficient of teflo
% mu = spektrMuRhoCompound([6 8;1 8])*rho*100;%attenuation coefficient of
% polystyrene
mu = mu_rho_function(E/1000, 'Kapton')*100;
%Sample data
thickness = 2*real(sqrt(r.^2-X.^2-Y.^2)); %[m] sphere
% thickness = 2*real(sqrt(r.^2-X.^2)); %[m] cylinder

%Phase image
img = zeros(ny, nx);
noiseVariance = zeros(ny,nx);
for n = 1:length(E)
    %Transmission function of the object at energy E(n)
    transmission = exp(-thickness*(mu(n)/2 + 1i*k(n)*delta(n)));
    %Fourier filter corresponding to free space propagation
    propagator = exp(-1i*pi*z*lambda(n)*w2);
    %propagator field for current photon energy
    img0 = abs(ifft2(fft2(transmission).*propagator)).^2;
    %add contribution of this energy to the image
    img = img + img0.*spectrum(n);
end

%Interpolate from simulation pixels to detector pixels
%Define pixel coordinates
Dx = p/M; Dy = p/M; %[m] pixel size in sample plane
xp = (min(x)-dx/2+Dx/2:Dx:max(x)+dx/2-Dx/2); %[m]
yp = (min(y)-dy/2+Dy/2:Dy:max(y)+dy/2-Dy/2); %[m]
%[m] create pixel coordinates matrices
[Xp,Yp] = meshgrid(xp,yp);
rp2 = Xp.^2+Yp.^2; %[m^2]
```

```
%Spatial freqencies
nxp = length(xp); nyp = length(yp); %number of pixels in x and y direction
%[1/m] frequency in the x and y direction respectively
up = ifftshift((-floor(nxp/2):floor((nxp-1)/2))/(nxp*Dx));
vp =ifftshift((-floor(nyp/2):floor((nyp-1)/2))/(nyp*Dy));
[Up, Vp] = meshgrid(up, vp); %[1/m]
w2p = Up.^2 + Vp.^2; %[1/m^2]

%Specify pixel reslution
pixelMTF = sinc(pi*p/M*U).*sinc(pi*p/M*V); %MTF corresponding to integration over the a
%Blur image (filter with MTF)
img = ifft2(fft2(img).*pixelMTF);

%Interpolate and scale signal with pixel size
img = interp2(X,Y, img, Xp, Yp)*p/M*p/M/(dx*dy);

Iin = img(1,1); %incident intensity at the object plane

%Models the absoprtion image
model_res_A = p/10;
dxA = model_res_A; %[m] simulation pixel size in x direction in object plane
dyA = model_res_A; %[m] simulation pixel size in y direciton in object plane
xfovA = 3*r;
yfovA = 3*r;
xminA = -xfovA/2; xmaxA = xfovA/2; %[m] x range of field of view in object plane
yminA = -yfovA/2; ymaxA = yfovA/2; %[m] y range of field of view in object plane
xA = xminA:dxA:xmaxA; yA = yminA:dyA:ymaxA; %[m] coordinate vectors
[XA,YA] =meshgrid(xA, yA); %[m] coordinate matrices

%Spatial frequencies
nxA = length(xA); nyA = length(yA); %number of pixels in x and y direction
%[1/m] frequency in the x and y direction respectively
uA =ifftshift((-floor(nxA/2):floor((nxA-1)/2))/(nxA*dxA));
vA =ifftshift((-floor(nyA/2):floor((nyA-1)/2))/(nyA*dyA));
[UA,VA] = meshgrid(uA,vA); %[1/m] frequency grid
w2A = UA.^2+VA.^2;

%Sample data for absorption image
```

```
% thickness = 2*real(sqrt(r.^2-XA.^2-YA.^2)); %[m] sphere
thickness = 2*real(sqrt(r.^2-XA.^2)); %[m] cylinder

%Sum up contributions to the image for all energies of the spectrum
img_abs = zeros(nyA, nxA); %[detector counts] the image to be calculated
noiseVariance = zeros(nyA,nxA);
for n = 1:length(E)
    %transmission function of the object at energy E
    transmissionA = exp(-thickness*(mu(n)/2 + 1i*k(n)*delta(n)));
    %Absorption Image
    img_abs = abs(transmissionA).^2;

    img_abs = img_abs + img_abs.*spectrum(n);


end

%Specify pixel resolution
pixelMTF = sinc(pi*p*UA).*sinc(pi*p*VA); %MTF corresponding to integration over the are
%Blur image (filter with the MTF)
img_abs = ifft2(fft2(img_abs).*pixelMTF);

%%%%%%%%%%%%%%%%%%%%%%%%%%%%%%%%%%%%%%%%%%%%%%%%%%%%%%%%%%%%%%%%%%%%%%%%%%%%
%
%Initialization values for APBA
%Note: Any physical distances  should be divided by 0.0050 cm/pix to
%convert to pixels
%
%%%%%%%%%%%%%%%%%%%%%%%%%%%%%%%%%%%%%%%%%%%%%%%%%%%%%%%%%%%%%%%%%%%%%%%%%%%%

delta_A_old = double(0);
I_delta = double(0);
error = double(0);
% re = re*100/p; %Radius of electron [pixels]
eta = (E*eV)./(me*(c^2));
%Equation 11 (Klein-Nishina equation)
sigma = 2.*pi.*re.^2.*((1+eta)./(eta.^2).*((2.*(1+eta))./(1+2.*eta)-(1./eta)...
    .*log(1+2.*eta))+1./(2.*eta).*log(1+2.*eta)-(1+3.*eta)./((1+2.*eta).^2)); %[m^2]
```

```
I0 = Iin;
n = 1;

I = img./I0; %normalized intensity
A0 = sqrt(img_abs);

sigma = sum(sigma.*spectrum)./sum(spectrum);
lambda_2_sigma = sum(lambda.^2./sigma.*spectrum)/sum(spectrum);
lambda = sum(lambda.*spectrum)/sum(spectrum);
delta = sum(delta.*spectrum)/sum(spectrum);

omega = lambda*R2/(2*pi*M); %[m^2]
k = lambda_2_sigma*R2*re/(2*pi*M); %[m^2]
while (n<=10)
    I_KN = (sqrt(I) + sqrt(I_delta)).^2;
    A_KN_2 = ifft2(fft2(I_KN)./(1+4*pi^2*k*w2p));

%     A_KN_2 = abs(A_KN_2);
    phi = lambda*re/sigma*log(A_KN_2); %phase

    A_KN = sqrt(A_KN_2);

    P = A0./A_KN;
    A_delta = A_KN.*(1-P);
    delta_error = abs(delta_A_old - A_delta);
    error = max(max(delta_error));

    T = A_delta.*exp(1i.*phi);
    G = exp(1i.*(rp2)./(2*omega));

    t0 = (fft2(T));

%Analytical transform of G by Rhiannon
    g = exp(-1i/2*omega*w2p)/(-1i/omega);
    e1 = (1/(2*pi*omega)).*g.*t0;
    E_1 = ifft2((e1));
    E_2 = conj(E_1);
```

```
    I_delta = abs(E_1).^2;
    delta_A_old = A_delta;
    n = n + 1;
end

thickness_retrieved = -lambda*phi/(2*pi*delta);

theoretical_thickness(L) = max(thickness(:)); %Diameter of the sphere or cylinder
kVp_all(L) = kVp;
absolute_error(L) = abs(theoretical_thickness(L) - max(max(thickness_retrieved)))*100;
relative_error(L) = absolute_error(L)/theoretical_thickness(L);
simulated_thickness(L) = max(max(thickness_retrieved));
R1_all(L) = R1;
R2_all(L)=  R2;
pixel_size(L) = p;
end
```

Appendix D

Phase Retrieval Simulation Matlab Code

```
clear all
clc
close all

addpath('C:\Users\rlloh\OneDrive - University of Waterloo\Master''s\Simulations\Researc
addpath('C:\Users\rlloh\OneDrive - University of Waterloo\Master''s\Simulations\xrTK\s
addpath('C:\Users\rlloh\OneDrive - University of Waterloo\Master''s\Simulations\xrTK\ta

%initialize matrices
simulated_thickness = [];
absolute_error = [];
relative_error = [];
kVp_all = [];
theoretical_thickness = [];
% method: Paganin = 0
%Arhatari TIE = 1
%Modified Bronnikov = 2
%PAD = 3
%Arhatari CTF = 4
%Bronnikov = 5
method = 0;
L = 0; % initialize a counter
```

```
%material: PTFE = PT
%Kapton = KA
%Tungsten = WW
%Polystyrene = PS
%Aluminum = Al
%Kevlar = KV
material = 'PT';
geo = 'C';
noise = 0; %include noise = 1
filter = -0.8; %creates a half-value layer of 1.2
ti = [1.5875, 2.8125, 3.175, 4.35, 5.5, 7]; % thickness to be simulated
spec = 0; %use spectrum from source = 0, use Spektr spectrum = 1

for j = 1:length(ti)
r = ti(j)/2*1e-3; % radius of a sphere
L = L+1;
kVp = 60;

%Imaging geometry
R1 = 8/100; % [m] source to object distance
R2 = 8/100; % [m] object to detector distance
Rtot = R1 + R2; % [m] source to detector distance

M = Rtot/R1; % magnification
z = R2/M; % [m] effective propagation distance

%Detector
p =7.8*1e-6; % [m] pixel pitch

%Simulation resolution and field of view
model_res = p/10;
dx = model_res; % [m] simulation pixel size in x direction in object plane
dy = model_res; % [m] simulation pixel size in y direction in object plane
xfov = 3*r;
yfov = 20e-6;
xmin = -xfov/2; xmax = xfov/2; % [m] x range of field of view in object plane
ymin = -yfov/2; ymax = yfov/2; % [m] y range of field of view in object plane
x = xmin:dx:xmax; y = ymin:dy:ymax; % [m] coordinate vectors
```

```
[X,Y] = meshgrid(x,y); % [m] coordinate matrices

%Spatial frequencies
nx = length(x); ny = length(y); % number of pixels in x and y direction
% [1/m] frequency in the x and y direction, respectively
u = ifftshift((-floor(nx/2):floor((nx-1)/2))/(nx*dx));
v = ifftshift((-floor(ny/2):floor((ny-1)/2))/(ny*dy));
[U,V] = meshgrid(u,v); % [1/m] frequency grid
w2 = U.^2 + V.^2; % frequency magnitude squared

%Physical constants
c = 299792458; % [m/s]
h = 6.6260689633e-34; % [Js] Planck's constant
eV = 1.6022e-19; % [J/eV] unit conversion constant
re = 2.82e-15; % [m] classical electron radius
Na = 6.022e23; % [atoms/mol] Avogadro's number
me = 9.10938356e-31; %[kg] mass of an electron

if spec == 1
    E = [1:150]*1e3;
    spectrum = spektrSpectrum(kVp,filter);
end

 % X-ray Spectrum
inherent_filtration = [spektrElement2Z('Be'), 0.1]; % [mm Be]
added_filtration = [[spektrElement2Z('Al'), 0.0]]; % [mm Al]
kVp = 90; % [kVp]

Phi_tube = spektrSpectrum(kVp, inherent_filtration); % spectrum with inherent filtratio
spectrum = spektrBeers(Phi_tube, added_filtration); % spectrum with filtration

if spec == 0
    Counts_Energy = load('C:\Users\rlloh\OneDrive - University of Waterloo\Master''s\Si
    spectrum = Counts_Energy.Phi;
    spectrum = spectrum./sum(spectrum);
    E = Counts_Energy.E;
    E = E*1000;
end
```

```
lambda = c*h./(E*eV); % [m] wavelength

k = 2*pi./lambda; %[1/m] angular wave number

%Sample data
if geo == 'C'
    thickness = 2*real(sqrt(r.^2-X.^2)); % [m] cylinder
elseif geo == 'S'
    thickness = 2*real(sqrt(r.^2-X.^2-Y.^2)); % [m] sphere
end


if material == 'PS'
%Polystyrene information for delta (phase coefficient):
%C8H8 is polystyrene
rho = 1.04; % density of polystyrene [g/cm^3]
Num_of_C = 8;
Num_of_H = 8;
Num_of_F = 0;

% %Atomic numbers
ZH = 1;
ZC = 6;
ZF = 9;

Z = ZC*Num_of_C + ZH*Num_of_H+ ZF*Num_of_F; %total atomic number

% Molar Mass
MMC = 12.011*Num_of_C; % [g/mol]
MMH = 1.008*Num_of_H; % [g/mol]
MMF = 18.998*Num_of_F; % [g/mol]
MM_total = MMC + MMH + MMF; % [g/mol] total molar mass
mu =spektrMuRhoCompound([6 8; 1 8])*rho*100; %[1/m] attenuation of polystyrene
mu = interp1([1:150], mu, E/1000);
```

```
elseif material == 'Al'
%Aluminum
rho = 2.7; %Density of Al [g/cm^3]
ZAl = 13; %Atomic number of Al
Num_of_Al = 1;

MMAl = 26.98; %[g/mol]
Z = ZAl*Num_of_Al;
MM_total = MMAl;
mu = spektrMuRhoElement(ZAl)*rho*100; %[1/m] attenuation of Aluminum
mu = interp1([1:150], mu, E/1000);

elseif material == 'PT'
% %Teflon information for phase coefficient:
% %C2F4 is PTFE
rho = 2.21439238; % density of PTFE [g/cm^3]
Num_of_C = 2;
Num_of_F = 4;
Num_of_H = 0;

% %Atomic numbers
ZH = 1;
ZC = 6;
ZF = 9;

Z = ZC*Num_of_C + ZH*Num_of_H+ ZF*Num_of_F; %total atomic number

% Molar Mass
MMC = 12.011*Num_of_C; % [g/mol]
MMH = 1.008*Num_of_H; % [g/mol]
MMF = 18.998*Num_of_F; % [g/mol]
MM_total = MMC + MMH + MMF; % [g/mol] total molar mass

mu = spektrMuRhoCompound([6 2; 9 4])*rho*100; % [1/m] attenuation of teflon
mu = interp1([1:150], mu, E/1000);

elseif material == 'KA'
%Kapton
```

```
rho = 1.42; %[g/m^3] Density of Kapton Polyimide film

%Composition C22H10N2O5
Num_of_C = 22;
Num_of_H = 10;
Num_of_N = 2;
Num_of_O = 5;

% Molar Mass
MMC = 12.011*Num_of_C; %[g/mol]
MMH = 1.008*Num_of_H; %[g/mol]
MMN = 14.00670*Num_of_N; %[g/mol]
MMO = 15.9994*Num_of_O; %[g/mol]
MM_total = MMC + MMH + MMN + MMO; %[g/mol] total molar mass

% Atomic numbers
ZH = 1;
ZC = 6;
ZN = 7;
ZO = 8;

Z = ZC*Num_of_C +ZH*Num_of_H + ZN*Num_of_N + ZO*Num_of_O; % total atomic number
mu = mu_rho_function(E/1000, 'Kapton')*100;

elseif material == 'WW'
 %Tungsten
rho = 19.3; %density of tungsten W
MM_total = 183.84;
Z = 74;

mu = spektrMuRhoElement(Z)*rho*100;
mu = interp1([1:150], mu, E/1000);

elseif material == 'KV'
% Kevlar
% COC6H4CONHC6H4NH
% C 14 O 2 H 10 N 2
rho = 1.44; % density of Kevlar in [g/cm^3]
```

```
MM_total =  10*1.008 + 14.00670*2 + 15.9994*2 + 12.011*14;
Z = 1*10 + 6*14 + 2*8 + 6*14;
mu = mu_rho_function(E/1000, 'Kevlar')*100;
end

nz_total = rho*1e6*1/MM_total*Na; %atoms/m^3;

delta = re*h^2*c^2./(2*pi*(E*eV).^2).*(nz_total*Z);

rho_Se = 4.819; %[g/cm^3] density of selenium
mu_Se = spektrMuRhoElement(34)*rho_Se*100; %[1/m] attenuation
mu_Se = interp1([1:150], mu_Se, E/1000);


thickness_Selenium = 100e-6; % [m] thickness of selenium deposited on the detector
eta = 1-exp(-mu_Se.*thickness_Selenium);

if spec == 1
    delta = delta';
    mu = mu';
    lambda = lambda';
    eta = eta';
end

spectrum_Se = spectrum.*eta;

%Sum up contributions to the image for all energies of the spectrum
%Ignoring noise in this situation
img = zeros(ny,nx); %[detector counts] the image to be calculated
img_abs = zeros(ny,nx); %[detector counts] the image to be calculated - absorption
noiseVariance = zeros(ny,nx);
for n = 1:length(E)
    %the transmission function of the object at energy E(n)
    transmission = exp(-thickness*(mu(n)/2+1i*k(n)*delta(n)));

    %Absorption Image
    img0 = abs(transmission).^2;
```

```
    %Superimpose absorption image data
    img_abs = img_abs + spectrum_Se(n).*img0;

    %Fourier filter corresponding to free space propagation
    propagator = exp(-1i*pi*z*lambda(n)*w2);

    %propagator field for current photon energy
    img0 = abs(ifft2(fft2(transmission).*propagator)).^2;

    %add contribution of this energy to the image
    img = img+img0.*spectrum_Se(n);

    %add contribution to the variance of the noise
    noiseVariance = noiseVariance + img0*spectrum_Se(n);
end

%Specify the detector resolution
dPSFWidth = 25e-6;%[m] FWHM of Gaussian detector point spread function
%[m] detector PSF standard deviation in sample plane
dPSFSigma = dPSFWidth/(2*sqrt(2*log(2)))/M;
%detector contribution to system MTF
detectorMTF = exp(-w2*pi^2*2*dPSFSigma^2);

%Specify pixel resolution
pixelMTF = sinc(pi*p/M*U).*sinc(pi*p/M*V); % MTF corresponding to integration over the

%Specify the source spatial distribution
sourceWidth = 7e-6; % [m] FWHM of Gaussian source
%[m] source standard deviation scaled to sample plane
sourceSigma = sourceWidth/(2*sqrt(2*log(2)))*(M-1)/M;
%source contribution to the system MTF
sourceMTF = exp(-w2*pi^2*2*sourceSigma^2);

%Add photon noise
NPS = exp(-w2*pi^2*4*dPSFSigma^2) + .05; %normalized noise power spectrum
% create an instance of white noise with the right noise variance
noiseInstance = randn(ny,nx).*sqrt(noiseVariance);
% filter the noise to get the correct noise power spectrum
```

```
noiseInstance = ifft2(fft2(noiseInstance).*sqrt(NPS));
if noise == 1
img = img + noiseInstance; %add the noise to the image
end


%Blur the image (filter with the MTF)
% img_blur = ifft2(fft2(img).*pixelMTF.*detectorMTF);
img_blur = ifft2(fft2(img).*pixelMTF);

%Interpolate from simulation pixels to detector pixels
%Define pixel coordinates
Dx = p/M; Dy = p/M; % [m] pixel size in sample plane
xp = min(x)-dx/2+Dx/2:Dx:max(x)+dx/2-Dx/2; % [m]
yp = min(y)-dy/2+Dy/2:Dy:max(y)+dy/2-Dy/2; % [m]
% [m] create pixel coordinates matrices
[Xp,Yp] = meshgrid(xp,yp);

%Interpolate and scale signal with pixel size
img = interp2(X,Y,img_blur,Xp,Yp)*p/M*p/M/(dx*dy);


%% Phase Retrieval
%Spatial Frequencies
nx = length(xp); ny = length(yp); %number of pixels in x and y direction
dx = Dx; dy = Dy;
%[1/m] frequency in the x and y direction, respectively
u = ifftshift((-floor(nx/2):floor((nx-1)/2))/(nx*dx));
v = ifftshift((-floor(ny/2):floor((ny-1)/2))/(ny*dy));
[U,V] = meshgrid(u,v); %[1/m] frequency grid
w2 = U.^2 + V.^2; %frequency magnitude squared

mu_poly = sum(spectrum_Se.*mu)/sum(spectrum_Se);
delta_poly = sum(spectrum_Se.*delta)/sum(spectrum_Se);
lambda_poly = sum(spectrum_Se.*lambda)/sum(spectrum_Se);

eta = (E*eV)./(me*(c^2));
%Equation 11 (Klein-Nishina equation)
```

```
sigma = 2.*pi.*re.^2.*((1+eta)./(eta.^2).*((2.*(1+eta))./(1+2.*eta)-(1./eta)...
    .*log(1+2.*eta))+1./(2.*eta).*log(1+2.*eta)-(1+3.*eta)./((1+2.*eta).^2)); %[m^2]

sigma = sum(sigma'.*spectrum_Se)/sum(spectrum_Se);
alpha = lambda_poly/(2*pi)*mu_poly/delta_poly;

if method == 0
    %Paganin's method
    g = img./img(1,1);
    %filter function
    Hp = mu_poly./(mu_poly+4*pi^2*delta_poly.*z*w2);
    %Fourier transform image
    FFTgI = fft2(g);
    %Multiply by the filter
    gf = FFTgI.*Hp;
    %Inverse Fourier transform the image
    IFFTgf = ifft2(gf);
    %Retrieve thickness of homogeneous object
    thickness_retrieved = -1/mu_poly*log(IFFTgf);

elseif method == 1
    %Arhatari TIE
    g = img./img(1,1)-1;
    %filter function
    Hp = 1./(mu_poly+z*delta_poly*4*pi^2.*w2);
    %Fourier transform image
    FFTgI = fft2(g);
    %Multiply by the filter
    gf = FFTgI.*Hp;
    %Inverse Fourier transform the image
    IFFTgf = ifft2(gf);
    %Retrieve thickness of homogeneous object
    thickness_retrieved = -IFFTgf; %[m]

elseif method == 2
    %Modified Bronnikov method
    g = img./img(1,1) -1;
    Hp = 1./(2*pi*lambda_poly*z*w2+alpha);
```

```
    gf = Hp.*fft2(g);
    phase = ifft2(gf);
    max(max(phase));
    min(min(phase));
    thickness_retrieved = -lambda_poly*phase./(delta_poly*2*pi);
elseif method == 3
    %PAD
    g = img./img(1,1);
    Hp = 1./(1+2*pi*re*lambda_poly^2*z/sigma*w2);
    gf = Hp.*fft2(g);
    phase = lambda_poly*re/sigma.*log(ifft2(gf));
    thickness_retrieved = -lambda_poly*phase./(delta_poly*2*pi);

elseif method == 4
      %Arhatari CTF
        beta = lambda./(4*pi).*mu;
        CTF_lambda = zeros(ny,nx,length(lambda));
    for k = 1:length(lambda)
        CTF_lambda(:,:,k) = (4*pi*sqrt(delta(k).^2+beta(k).^2)./lambda(k).*sin(pi*lambd
    end

CTF_poly = zeros(ny,nx);

for k = 1:ny
    for j = 1:nx
        CTF_poly(k,j) = trapz(E, CTF_lambda(k,j,:))./trapz(E, spectrum);
    end
end
    Hp = (1./CTF_poly);
    g = img./img(1,1)-1;
    FFTgI = (fft2(g));
    gf = FFTgI.*Hp;
    IFFTgf = ifft2((gf));
    thickness_retrieved = -(IFFTgf);

elseif method == 5
    %Bronnikov method
    g = img./img(1,1) -1;
```

```
    Hp = 1./(2*pi*lambda_poly*z*w2);
    [index1, index2] =find(isinf(Hp));
    Hp(index1, index2) = 1e-28;
    gf = Hp.*fft2(g);
    phase = ifft2(gf);
    max(max(phase));
    min(min(phase));
    thickness_retrieved = -lambda_poly*phase./(delta_poly*2*pi);
end



theoretical_thickness(L) = max(thickness(:)); %Diameter of the sphere or cylinder
kVp_all(L) = kVp;
absolute_error(L) = abs(theoretical_thickness(L) - max(max(thickness_retrieved)))*100;
relative_error(L) = absolute_error(L)/theoretical_thickness(L);
simulated_thickness(L) = max(max(thickness_retrieved));
R1_all(L) = R1;
R2_all(L)=  R2;
pixel_size(L) = p;
end
simulated_thickness = simulated_thickness';
theoretical_thickness = theoretical_thickness';

figure;
% for Intensity, with Se for Retrieval
plot(theoretical_thickness*1e6, simulated_thickness*1e6)
xlabel('Theoretical Thickness [um]')
ylabel('Simulated Thickness [um]')
title('Using Spectrum with Se Absorption')
xlim([20, 200])
figure;
plot(theoretical_thickness*1e6, relative_error, 'o')
xlabel('Theoretical Thickness [um]')
ylabel('Relative Error (%)')
title('Using Spectrum with Se Absorption')

]
```

Appendix E

Phase Retrieval Experimental Matlab Code

E.1 Gain Matlab Code

```
close all
clear variables
filename1 = 'All_Images_Averaged';
filename2 = 'Iin_Averaged';


darkpath = 'Z:\Chris\Data\2018\Oct31\Oct31_1_16in_PTFESphere_60kV_2mmAl_2995ms_R1_36cm_
openpath = 'Z:\Chris\Data\2018\Oct31\Oct31_1_16in_PTFESphere_60kV_2mmAl_2995ms_R1_36cm_
rawpath = 'Z:\Chris\Data\2018\Oct31\Oct31_1_16in_PTFESphere_60kV_2mmAl_2995ms_R1_36cm_P

num_rows = 1000;
num_cols = 1000;

%Extract the image from *.dat file that forms a matrix
%Index for number of images want to use in average
Index_Dark = 25:30;
Index_Open = 2:30;
Index_Raw = 2:30;
```

```
Dark_Image = Load_Images_Dat(darkpath, Index_Dark, num_rows, num_cols);
Open_Image = Load_Images_Dat(openpath, Index_Open, num_rows, num_cols);
Raw_Image = Load_Images_Dat(rawpath, Index_Raw, num_rows, num_cols);

n_img_dark = size(Dark_Image, 3);
n_img_open = size(Open_Image, 3);
n_img = size(Raw_Image, 3);

Instructions = menu('Select the region of interest to be evaluated', 'OK');
fig_img = figure;
imshow(squeeze(Raw_Image(:,:,1)));
title('Select Region of Interest');
imcontrast;
rect = getrect(fig_img);
close(fig_img);

if (rect(3) == 0) || (rect(4) == 0)
       %if the user clicks instead of drawing a rectangle, the entire image
       %is selected as the ROI
       Raw_Image_roi = Raw_Image;
       Dark_Image_roi = Dark_Image;
       Open_Image_roi = Open_Image;
else
    Raw_Image_roi = Raw_Image(rect(2):rect(2)+rect(4),...
        rect(1):rect(1)+rect(3), :);
    Dark_Image_roi = Dark_Image(rect(2):rect(2)+rect(4),...
        rect(1):rect(1)+rect(3), :);
    Open_Image_roi = Open_Image(rect(2):rect(2)+rect(4),...
        rect(1):rect(1)+rect(3), :);
end

size_roi = size(Raw_Image_roi);

offset = squeeze(mean(Dark_Image_roi, 3));
open = squeeze(mean(Open_Image_roi, 3));
Open_Offset = open - offset;
gain = mean(Open_Offset(:))./Open_Offset;
```

```
Intensity = (Raw_Image_roi - repmat(offset,1,1,n_img))...
    .*repmat(gain,1,1,n_img);

I_in = (Open_Image_roi - repmat(offset, 1, 1, n_img_open))...
    .*repmat(gain,1,1,n_img_open);

Intensity = squeeze(mean(Intensity, 3));
I_in = squeeze(mean(I_in, 3));

dicomwrite(uint16(Intensity), filename1);
dicomwrite(uint16(I_in), filename2);

save('Image.mat', 'Intensity', 'I_in');
```

E.2 Phase Retrieval Experimental Matlab Code

```
clear all
clc
close all

addpath('C:\Users\rlloh\OneDrive - University of Waterloo\Master''s\Simulations\Phase r
fpath = 'C:\Users\rlloh\OneDrive - University of Waterloo\Master''s\Simulations\Phase R

fname = 'All_Images_Averaged';
fpath2 = fpath;
fname2 = 'Iin_Averaged';

I = double(dicomread([fpath '\' fname]));
I_in = double(dicomread([fpath2 '\' fname2]));

true_t = 1.5875e-3; % measured thickness [m]

c = 2.9979e8; % Speed of light in a vacuum [m/s]
h = 4.1357e-15; % Planck's constant [eV.s]
r_e = 2.8179e-15; % Classical electron radius [m]
Na = 6.022e23; % Avagadro's number [1/mol]
```

```
p = 7.8e-6; % [m] Pixel pitch
R1 = 0.36; % [m] Source-to-object distance [m]
R2 = 0.08; %[m] Object-to-detector distance [m]
M = (R2+R1)/R1;
z = R2/M;
dimension = size(I);
nx = dimension(2);
ny = dimension (1);
dx = p/M;
dy = dx;
x = dx*(0:nx-1);
y = dy*(0:ny-1);
[Xp,Yp] = meshgrid(x,y);

u = ifftshift((-floor(nx/2):floor((nx-1)/2))/(nx*dx));
v = ifftshift((-floor(ny/2):floor((ny-1)/2))/(ny*dy));
[U,V] = meshgrid(u,v);
w2 = U.^2 +V.^2;

%X-ray spectrum
Counts_Energy = load('C:\Users\rlloh\OneDrive - University of Waterloo\Master''s\Simula
spectrum = Counts_Energy.Phi;

E = Counts_Energy.E;
E = E*1000; %[eV]

E_mu = [1:150]*1e3;
mu_Se = spektrMuRhoElement(34)*4.819*100;
mu_Se = interp1(E_mu, mu_Se, E);
thickness_Selenium = 100e-6; % [m] thickness of selenium deposited on the detector
eta = 1-exp(-mu_Se.*thickness_Selenium);
spectrum = spectrum.*eta;

lambda = c*h./E; %[m] wavelength

%Al properties
% rho_obj = 2.7; %density of Al [g/cm^3]
```

```
% MM = 26.98; %[g/mol]
% Z = 13; %Atomic number of Al
% mu_obj = spektrMuRhoElement(Z)*rho_obj*100;

%PTFE properties
rho_obj = 2.21439238; % Material density [g.cm^-3]
% rho_obj = 2.13135266;
MM = 100.016; % Molecular mass [g.mol^-1]
Z = 2*6 + 4*9; % Total atomic number
% E_mu_obj = [5 6 8 10 15 20 30 40 50 60]*1e3; % [eV]
% mu_rho_obj = [540.9 314.2 132.7 68.05 20.88 9.667 4.025 2.647 2.132 1.880]*1e-1; % Ma
mu_obj = spektrMuRhoCompound([6 2; 9 4])*rho_obj*100;

%Acrylic properties
% rho_obj = 1.1902357; %[g/cm^3]
% MM = 12.011*5 + 1.008*8 + 15.9994*2; %Molecular mass [g/mol]
% Z = 5*6 + 8*1 + 2*8; %Total atomic number
% mu_obj = spektrMuRhoCompound([6 5; 1 8; 8 2])*rho_obj*100;

mu_obj = interp1(E_mu, mu_obj, E, 'pchip');

% Attenuation and refraction properites
N = rho_obj*Na/MM; % Atomic number density [#atoms.cm^-3]
% mu_obj = interp1(E_mu_obj,mu_rho_obj,E,'pchip')*rho_obj*1e2; % Attenuation coefficien
delta = (r_e*(h*c)^2)./(2*pi*E.^2).*(N*1e6).*Z;  % Refractive index decrement

mu_poly = sum(mu_obj.*spectrum)/sum(spectrum);
delta_poly = sum(delta.*spectrum)/sum(spectrum);
lambda = sum(lambda.*spectrum)/sum(spectrum);

Image = I./I_in;

Image(isinf(Image)) = 0;
Image(isnan(Image)) = 0;

Hp = mu_poly./(delta_poly*z*(2*pi)^2*w2 + mu_poly);
g = fft2(Image);
g_filtered = g.*Hp;
```

```
thickness = -1/mu_poly*log(ifft2(g_filtered));


%% Determining the thickness of the object
n = 1; %index - n stays 1 as long as the user wants to plot more thickness
       %profiles of the object
Figure_number = 0; %Figure number for the thickness profile

while n == 1
Figure_number = Figure_number + 1;
Instructions = menu('Select line of interest to create thickness profile with cursor ar
fig = figure;
title('Select Line of Interest');
imshow(thickness*1e6)
imcontrast
[x, y] = getline(fig);
close (fig);

fig_thickness = figure;
thickness_profile = improfile(thickness,x,y);
plot(thickness_profile)
title(['Thickness Profile ' int2str(Figure_number)]);

%Get the user to draw lines in the region where the object is present and
%where there is no object present
menu('Draw a line where the max thickness appears for an average and press Enter', 'OK
index_max = floor(getline(fig_thickness));
menu('Draw a line where there appears to be no object for an average and press Enter',
index_min = floor(getline(fig_thickness));

%if the indices exceed the length of the vector 'thickness_profile',
%redefine them as seen below
if index_max(1,1) > index_max(2,1)
    if index_max(2,1) < 1
        index_max(2,1) = 1;
    end
    if index_max(1,1) > length(thickness_profile)
        index_min(1,1) = length(thickness_profile);
```

```
    end
    %Calculate the mean over the regions selected by the user
    max_thickness = mean(thickness_profile(index_max(2,1):index_max(1,1)))

else
    if index_max(1,1) < 1
       index_max(1,1) = 1;
    end
    if index_max(2,1) > length(thickness_profile)
        index_min(2,1) = length(thickness_profile);
    end
    %Calculate the mean over the regions selected by the user
    max_thickness = mean(thickness_profile(index_max(1,1):index_max(2,1)));
end

if index_min(1,1) > index_min(2,1)
    if index_min(2,1) < 1
       index_min(2,1) = 1;
    end

    if index_min(1,1) > length(thickness_profile)
        index_min(1,1) = length(thickness_profile);
    end
    %Calculate the mean over the regions selected by the user
    min_thickness = mean(thickness_profile(index_min(2,1):index_min(1,1)));

else
    if index_min(1,1) < 1
       index_min(1,1) = 1;
    end

    if index_min(2,1) > length(thickness_profile)
        index_min(2,1) = length(thickness_profile);
    end
    %Calculate the mean over the regions selected by the user
    min_thickness = mean(thickness_profile(index_min(1,1):index_min(2,1)));
end
```

```
%Calculate the total thickness of the object
total_thickness = max_thickness-min_thickness;
%Display the total thickness of the object
display(['The total thickness of the object is ' num2str(total_thickness*1000) ' mm']);

%prompt the user to see if they want to plot another thickness profile
n = menu('Plot another thickness profile?', 'Yes', 'No');
end

%Multiplication factor used to save the image of a '.dcm' file and to show
%the image in a figure at the end
% Multiplication_Factor = 10^3/10^(floor(log10(mean(mean(thickness)))));
dicomwrite(int16((thickness-1e-4).*1000000),'thickness');
```